Stockholm University

Bachelor Thesis

Degree Project in
Geology 15 hp

Determination of metamorphic P-T conditions of the Tarfala Amphibolite in the Tarfala valley, Kebnekaise mountains, with petrographic and SEM/EDS analysis.

Elin Hellgren

Stockholm 2022

Department of Geological Sciences
Stockholm University
SE-106 91 Stockholm

Abstract

This study focuses on the geology of the Tarfala Valley which is situated in the Kebnekaise mountains of the Scandinavian Caledonides. The bedrock in this area is comprised of north-west to south-west dipping thrust sheets (nappes) belonging to the Middle Allochthon and the Seve Nappe Complex which derives from the Caledonian Orogeny. A geological map, based on field observations and previous studies of the Tarfala Valley is presented in this thesis. Further-more, petrographic studies, Scanning Electron Microscopy (SEM) with Energy Dispersive Spectroscopy (EDS) studies and Thermodynamic modelling using THERMOCALC were used to estimate pressure and temperature conditions during metamorphism of a sample from the Tarfala Amphibolite (Seve Nappe Complex). This yielded peak metamorphic conditions of 606±27°C and 1.13±0.1 GPa which places the Tarfala Amphibolite in the high-pressure end of the Amphibolite facies, bordering the Eclogite facies. In addition, some evidence for metamorphic fluid flow is also presented.

Aim

The aim of this study is to map the Tarfala Valley, Kebnekaise mountains, and define and quantify the metamorphic conditions by acquiring pressure and temperature (P-T) estimates from the Tarfala Amphibolite located in the valley. The goal is to achieve data based on petrographic examination, fieldwork, Scanning Electron Microscope (SEM) with fitted Energy-dispersive detector (EDS) analyses and the use of internally consistent databases (THERMOCALC and AX). Beyond achieving P-T estimates, I aimed to construct a 4km^2 map centred on the Tarfala station from where the field work was conducted in the Tarfala Valley July 2021.

Table of Contents

1. Introduction

1.1 Geological background

Tectonic history

The supercontinent Rodinia broke up during the late Proterozoic and early Palaeozoic and initial rifting at-, 650 Ma is marked by intruding dykes in Egersund, southwest Norway (Brasier et al. 1996). Continental rifting then developed in to sea-floor spreading leading to the appearance of the Iapetus-Ocean (Lundqvist 2001). Evidence from eg. U-Pb dating point to a timespan around 620-605 Ma for the initiation of the Iapetus-Ocean sea-floor spreading (Svenningssen 2001). Eventually, lithosphere of the Iapetus-Ocean begun to close and the continents, Baltica and Laurentia, started moving toward each other. These movements are called the Finnmarkian event and can be viewed upon as the start of the Caledonian orogeny (Lundqvist 2001), (Andréasson et al. 1998). Evidence for mountain building affecting the western parts of Baltica during this time exist in the form of tectonic deformation and metamorphism. However due to oblique movement the Iapetus-sea was still present and parts of it in the north-west continued to open at the same time (Lundqvist 2001, Brasier et al. 1996). Total disappearance of the Iapetus-Ocean occurred during the Silurian and Devonian resulting in the Caledonian orogeny (Lundqvist 2001). The assemblage of continents was between Laurentia, Baltica and Avalonia. By Permian times, these continents together formed the later super continent Pangea by collision with Gondwana. Pangea was a relatively short-lived super continent compared to Rodinia. The Caledonian orogeny was at least 700-800km wide before opening of the next ocean to appear: the Atlantic Ocean. Today the orogen outline the borders of the north Atlantic-Ocean with Greenland in the west and Scandinavia to the east (Brasier et al. 1996), (Gee et al. 2008). The Scandinavian part of the Caledonides consist of several nappes (fig. 1) thrusted on top of each other forming a 100-300 km wide belt stretching from Stavanger in the south to Nordkap and Varangerfjord in the north (Lundqvist 2001). In Scandinavia the thrusts verge east while the corresponding thrusts in Greenland verge toward the west (Gee et al. 2008).

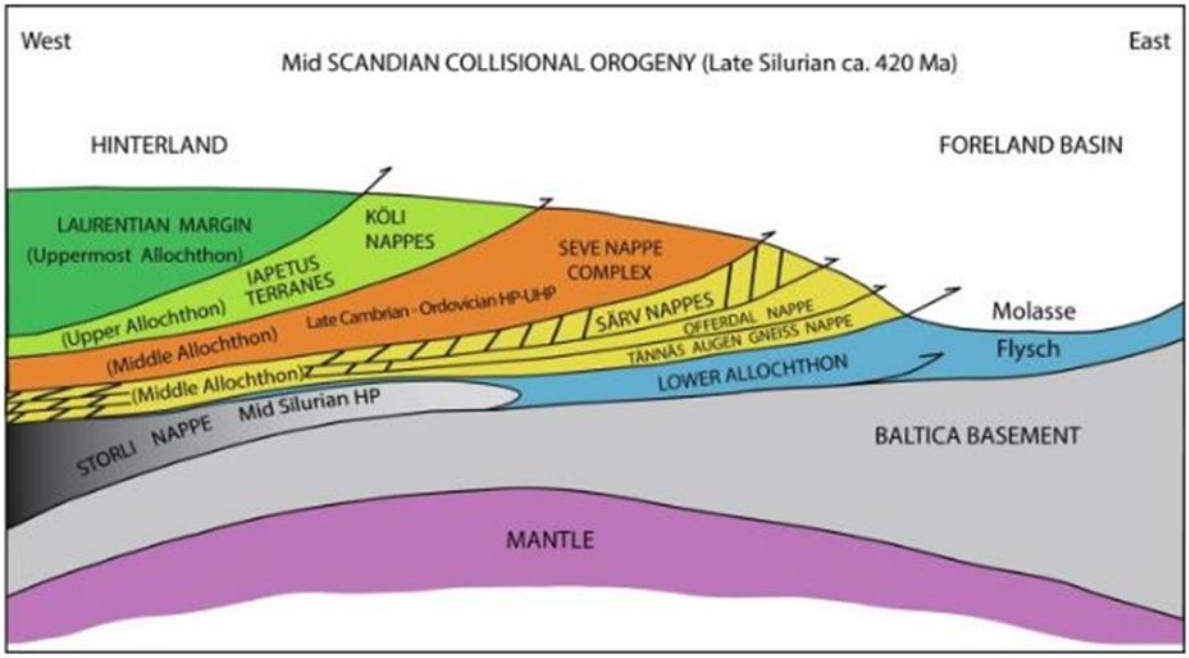

Figure 1. Simplified picture of the Scandinavian nappe succession in the Late-Silurian. Modified from (Gee 2021).

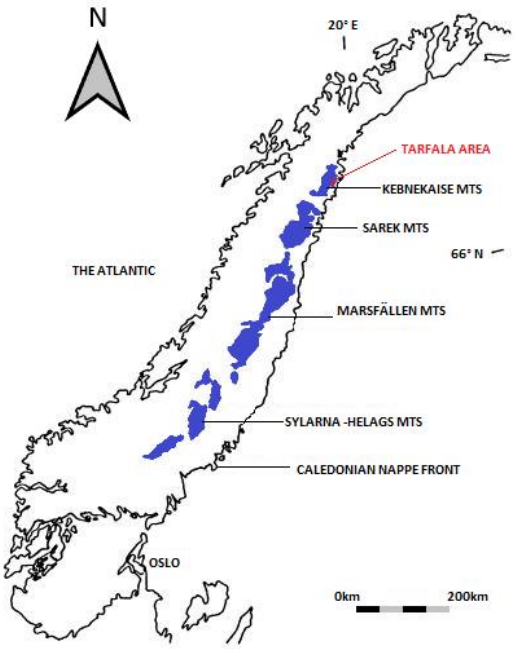

Figure 2. The Seve belt of the Scandinavian Caledonides. Modified from (Andréasson & Gee, Bedrock Geology and Morphology of the Tarfala Area, Kebnekaise Mts., Swedish, 1989)

Present tectonic setting and stratigraphy

The tectonostratigraphic thrust Sheets of the Scandinavian Caledonides consist of four separate major allochthons, -Lower, -Middle, -Upper and Uppermost Allochthon (fig. 1). These are thrusted on top of the Precambrian Autochthonous-Parautochthonous bedrock (Stephens et al. 1985). The Lower and Middle Allochthon are formed by rocks that originate from the Baltoscandian margin with both rocks of sedimentary origin and crystalline basement. The upper Middle Allochthon also contains intruding mafic dykes related to the opening of the Iapetus Ocean. Other terranes related to the Iapetus Ocean comprise the Upper Allochthon. The Uppermost Allochthon is considered to be derived from the Laurentian continent (Gee 2021). These major allochthons are divided in to smaller sub-allochthons (Stephens et al. 1985).

This project focuses on the Seve Nappe Complex which is a major sub-allochthon of the Swedish Caledonides (fig. 2) (Andréasson et al. 2018). At the present, there is an ongoing debate as to whether the Seve Nappe Complex belongs to the upper part of the Middle Allochthon (Baird et al. 2014); (Andreasson et al. 2018); (Gee et al. 2012) or the lower part of the Upper Allochthon (Greiling & Grimmer 2007); (Stephens et al. 1985); (Gee & Zachrisson, 1979); (Baird 2004). In this study, for convenience, I follow in line with Baird et al. (2014); Andreasson et al. (2018) and Gee et al. (2012). However, I acknowledge that it's Arbitrary. For almost 1000 km the Seve Nappe Complex forms a grand belt of geographically separated smaller thrust sheets along the mountain belt and lie under most of Scandinavia's highest mountains (fig. 2) (Andréasson 1998); (Andréasson 1989). These thrust sheets are all dominated by metamorphosed Baltoscandian rift basin infill and rift related magmatism in the form of metamorphosed mafic igneous dykes which intruded during opening of the Iapetus-sea (Andréasson et al., 1998).

This study is conducted in the Tarfala Valley, located in the Kebnekaise mountains (fig.2), in which the Seve nappe crops out (Andréasson et al. 1989). The Köli Nappe Complex (fig. 1) is in many places

thrusted on top of the Seve Nappe Complex and the border between them represent the boundary between continental and oceanic crust which is important to identify for understanding the orogens accretion and pre-collisional palaeography. Identification of the Köli Nappe Complex has been determined by the presence of fossils but due to strong tectonic influence and alteration this is often difficult. This difficulty of locating the border contributes to discussions on its nature regarding lithology, metamorphic history and classification as a major tectonic boundary (Andréasson 2020).

Tectono-stratigraphy of the Tarfala Valley

In previous studies conducted in the Tarfala Valley the Seve nappe is thought to consist of the Kebne Dyke Complex, Kebne Amphibolite, Storglaciären Mylonite Gneiss, Tarfala Amphibolite, Quartzo-feldspathic gneiss and Pelitic schist in order from top to bottom. The Jåkk Mylonite Gneiss of the Middle Allochthon serves as the lower contact for the Seve Nappe Complex (fig. 3) (Stephens et al. 1985); (Baird 2004). Beyond the aim of mapping the stratigraphical sequence of the Tarfala Valley this study will focus on making pressure and temperature estimates of metamorphic conditions from the Tarfala Amphibolite.

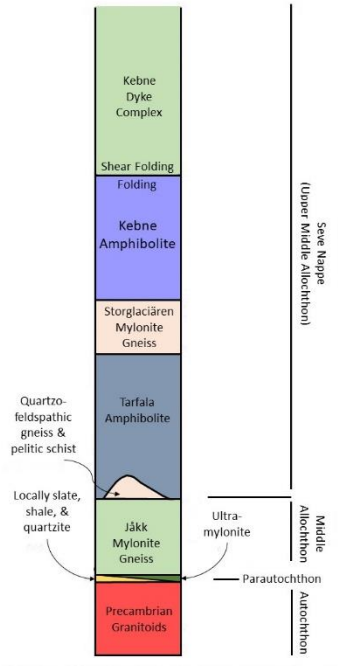

Figure 3. Left; local techtonostratigraphy of the Tarfala Valley. Right; regional techtonostatigraphic framework. Modified from (Stephens, Gustafsson, Ramberg, & Zachrisson, 1985).

Metamorphic history

The metamorphic facies provide a framework for determining the conditions at which a rock was metamorphosed based on which a tectonic setting can sometimes be elucidated. The concept was founded and developed by Pentii Eskola between 1915 and 1939 from an original idea of V.M. Goldsmith between 1911 and1912. The discovery was that the chemical bulk composition of a metamorphic rock could be directly related to equilibrium mineral assemblage at particular metamorphic grades. Eskola found that mineral assemblage could differ between rocks from

different areas but still had the same chemical bulk composition. He concluded that the reason for this must be physical differences between the regions in which the rocks had come from. Development on this idea by strict qualitative thermodynamic reasoning led to the conclusion on how the conditions of pressure and temperature affect the mineral assemblage. Eskola developed a diagram which relate pressure and temperature with specific mafic mineral assemblages which he named Facies. The metamorphic facies diagram used today (fig. 4) is further developed from Eskolas work. The modern diagram show facies areas with generally accepted temperature and pressure limits. The areas between represent mineral reaction isograds which is when key minerals either are lost or introduced thus changing the mineral assemblage (Winter 2014).

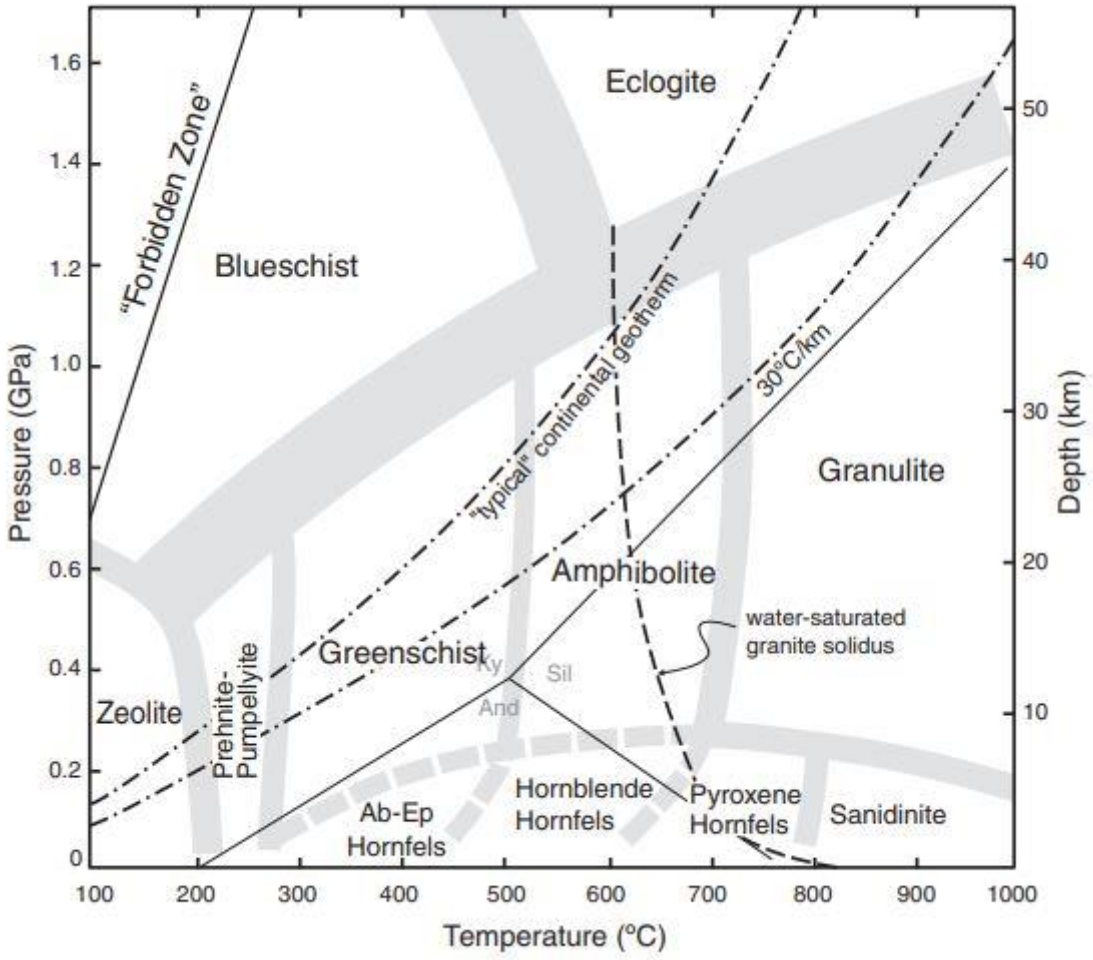

Figure 4. Pressure-temperature metamorphic facies diagram with approximate boundaries (Winter 2014).

In the studied area within the Kebnekaise mountains as well as within the Sarek mountains the Seve Nappe Complex crops out. In both of these locations the border between the continent ocean transition and the underlying gneisses of the Middle Allochthon is distinguished by a pressure increase of the metamorphic conditions for the continent ocean transition. In the area of Kebnekaise magmatic gneisses are thought to exist due to early subduction followed by exhumation (Andréasson, et al. 2018). The Middle Allochthon below the Seve Nappe Complex and the Köli Nappe Complex have experienced greenschist facies (fig.4) peak metamorphic conditions while the Seve Nappe Complex experienced high pressure metamorphic peak conditions, up to eclogite facies (fig.4) at some locations due to conditions resulting from the Finnmarkian orogeny. The order of processes

whereby this high-pressure nappe came to be and how it was placed between less metamorphosed nappes is poorly understood. Several theories exist but more research is needed for understanding the exact exhumation mechanisms involved (Baird 2008). There are however known areas of the Seve Nappe Complex which have been confirmed to have experienced Eclogite facies within Sweden. They are located in the southwest Norrbotten and in the northwest Jämtland. The latter area in Jämtland is believed to exist due to an episode of ultra high pressure caused by deep subduction of the Baltoscandian margin, this during the time when closure of the Iapetus Ocean was ongoing (Gee D.G., et al. 2012). In Jämtland, Ultra high pressure metamorphism at 4.1-4.2 GPa and 830-840°C has been recorded together with an overprint at granulite facies conditions at 1.0-1.1 GPa and 850-860°C. Eclogites and metasedimentary rocks from the Vaimok lens in south-western Norrbotten have been confirmed to have experienced peak conditions at 2.8-3.1 GPa and 660-780°C. In the Sarek area (fig. 2), records of blueschist to eclogite facies exist in a bedrock unit called the Tsäkkok lens. The Tsäkkok lens record minimum pressures of 2.2GPa and 590± 60 ◦C and overlies the Sarek lens which has experiensed amphibolite facies (Bukala M., et al. 2020).

Chemistry and age of the Kebne Dyke Complex

Previous research has shown that the Kebne Dyke Complex has similar geochemistry to other units in the Seve Nappe Complex e.g. Sarek dyke swarms and Indre-Troms dykes and that all of these units probably represent the continent ocean transition. The Kebne Dyke Complex differs from the Sarek dyke swarms and Indre-Troms dykes by being the least enriched and having T-MORB chemistry. The latter complexes also possess a greater proportion of metasedimentary country rock in to which the dykes are intruded (Baird & Chamberlain 2014). Due to geochemical similarities, a common origin for the Kebne Dyke Complex, Kebne Amphibolite and Tarfala Amphibolite has been suggested (Baird & Chamberlain 2014). The intrusive age of the Kebne Dyke Complex has been estimated by U-Pb dating of zircons to around 608-596 Ma thus 14 Myr younger than the similar Sarek dyke swarms (Baird & Chamberlain 2014).

1.2 Geothermobarometry

Theory of Geothermobarometry

The method for determining metamorphic conditions has evolved from being mostly qualitative towards being more quantitative today. Early methods included the classic Barrovian pelitic-index minerals as indicators of the metamorphic grade and were used for comparison across and between terranes. Some specific minerals would suggest high temperature while some would suggest low temperature conditions. Today the method has evolved through experimental petrology to become more quantitative. One quantitative method which has developed is named Geothermobarometry. This method has been developed from combining thermodynamic calculations with results from modelling natural systems in labs using varying temperature and pressure conditions. Geothermobarometry is used for determining metamorphic conditions by quantifying temperature and pressure estimates. Temperature and pressure conditions affect composition of solid-solution phases due to continuous, ion-exchange reactions and solid-solid net transfer reactions. By measuring the distribution of elements in phases which coexist equilibrium temperature and pressure can be calculated. Different reactions will result in various amount of change of volume. A small volume change as for example in most ion-exchange reactions will be suited for estimating temperature. On the contrary, a large volume change of a reaction, as often seen in solid-solid net transfer reactions, is better suitable for estimating pressure. This means that the amount of change in volume of a Geothermobarometer decides if it is more suitable for pressure or temperature

estimates. The general idea of geothermobarometry is, if based on an equilibrium texture the mineral composition related to these types of reactions record maximum metamorphic conditions. Zoning in crystals may in addition be used for determining the pressure-temperature-time path of metamorphism. Depending on reaction used this method can be a highly sensitive indicator of both temperature and pressure (Winter 2014).

Thermodynamic calculations

End-members of minerals can be used to calculate an independent set of reactions between an assemblage of minerals at equilibrium. Equilibrium relationship for the reactions can be expressed with the formula:

$0 = \Delta G^\circ + RT \ln K$ *(Equation 1)*

(Holland &Powell 1994)

In the formula, ΔG° is change of free energy of the reaction which is a function of pressure and temperature, R is the gas constant, T is temperature and K is the equilibrium constant which is calculated from the end-member activities. The formula is fundamental for Geothermobarometry because it relates temperature and pressure with the ratio between elements in co-existing minerals. The ratio is given by K in the formula. (Holland & Powell 1994).

An example of an experimentally calibrated reaction that is commonly used and good for Geothermometry is exchange between Fe and Mg in garnet and biotite:

$KFe_3AlSi_3O_{10}(OH)_2 + Mg_3Al_2Si_3O_{12} = KMg_3AlSi_3O_{10}(OH)_2 + Fe_3Al_2Si_3O_{12}$ *(Reaction 1)*

biotite + garnet = biotite + garnet

(Ferry & Spear 1978)

The above reaction yields a high slope on a pressure- temperature diagram when expressed as dP/dT, thus having low volume change and being suitable as a geothermometer (Winter 2014). An example of a commonly used geobarometer is GASP. It is based on a continuous net- transfer reaction between garnet, aluminosilicate, silica and plagioclase:

$3\ CaAl_2Si_2O_8 = Ca_3Al_2Si_3O_{12} + 2\ Al_2SiO_5 + SiO_2$ *(Reaction 3)*

anorthite = grossular (garnet) + kyanite + quartz

(Ferry & Spear 1978)

In contrast to the garnet-biotite exchange geothermometer, GASP yields a low slope on a pressure-temperature diagram expressed as dP/dT. Therefor the large volume change makes it a good geobarometer. By measuring distribution of elements and calculating the equilibrium constant (K) in natural assemblages a comparison to P-T conditions modelled and replicated in previous laboratory studies can be made. When two phases exist at equilibrium, almost all elements will distribute themselves between the phases. This process is called chemical fractionation and the distribution is fixed at a specific temperature and pressure. With a thermodynamic quantitative approach to mineral equilibria this distribution can be manifested as an equilibrium constant (K) (Winter 2014). As an example, for the reaction between garnet and biotite (reaction 1) K is calculated as:

$$K = \left(\frac{a_{Mg}^{Gt}}{a_{Fe}^{Gt}}\frac{a_{Fe}^{Bt}}{a_{Mg}^{Bt}}\right) \approx \left(\frac{\left(X_{Mg}^{Gt}\right)^3}{\left(X_{Fe}^{Gt}\right)^3}\frac{\left(X_{Fe}^{Bt}\right)^3}{\left(X_{Mg}^{Bt}\right)^3}\right) = \left(\frac{(Mg/Fe)_{Gt}}{(Mg/Fe)_{Bi}}\right)^3$$ *(Equation 2)*

(Ferry & Spear 1978)

In this equation 'a' is the activity of the element and with assumed ideal mixing the activity is given by its mole fraction cubed. X is mole fraction. The '3' is derived from the number of sites for Mg and Fe in the formula units in biotite and in garnet (Winter 2014). Analysis of coexisting biotite and garnet will yield a Distribution coefficient (Kd):

$$Kd = \frac{(Mg/Fe)_{Gt}}{(Mg/Fe)_{Bi}}$$ *(Equation 3)*

(Winter 2014)

The Distribution coefficient (Kd) is thus related with the Equilibrium constant by:

$$K = Kd^3$$ *(Equation 4)*

(Winter 2014)

In laboratory research made by Ferry and Spear (1978) the ratio between Mg and Fe in coexisting garnet and biotite for different temperatures were measured. The resulting data were then used to calculate 1/T and lnK. After this calculation they plotted 1/T and lnK against each other and obtained a best fit linear relationship with linear regression. An equation for a straight line ($y = m \times x + c$) was thus obtained where Y is lnK, X is 1/T and C is equal to change of entropy for the reaction divided by the gas constant (8.3144 J.mol^{-1}.K^{-1}). The negative change of enthalpy of the reaction minus the pressure used in the experiment times the change of volume of the reaction all then divided by the gas constant gives m.

$$y = -6327x + 2.346$$ *(Equation 5)*

(Ferry & Spear 1978)

A calibrated geothermometer was obtained by substituting the obtained values in to an equation which relates temperature (°K), pressure (MPa) and Kd:

$$T = \frac{52090 + 2.494P}{19.506 - 3 \times 8.3144 \ln Kd}$$ *(Equation 6)*

(Ferry & Spear 1978)

In a similar way Koziol & Newton (1988) studied the solid-solid net transfer reaction with a large change of volume and obtained the geobarometer called GASP with temperature (°T) related to pressure (MPa):

$$T = \frac{-48357 - 66.08P}{-150.66 - 8.3144 \ln K}$$ *(Equation 7)*

(Koziol & Newton 1988)

In the equation of a straight line which they developed Y equals pressure and X equals temperature. The equation for K used for GASP is:

$$K = \frac{\left(X_{Ca}^{Gt}\right)^3}{\left(X_{Ca}^{Plag}\right)^3}$$ *(Equation 8)*

(Koziol & Newton 1988)

THERMOCALC and the Average P-T method

During the past 30-40 years the evolution has evolved from using a few relevant calculations by hand. Today, microprobe data and different geothermo/barometers handled by computer programs and spreadsheets are used (Holland & Powell 1998). Instead of using single reactions with direct calibration by experimental studies, it is more common today to use an internally consistent thermodynamic data-set. Since 1990 a software named THERMOCALC has been available for calculating estimates of pressure and temperature. THERMOCALC was developed by Holland and Powell and the fundamental method was later described by them in Holland and Powell (1994). The benefit of using THERMOCALC is that the program uses all available and updated information from calibrated and experimentally developed data-sets. This leads to more precise estimates of the pressure and temperature conditions (Holland & Powell 1994). A problem which had become evident when using several thermometers and barometers for one mineral assembly was that the system became over-determined and a method for finding the optimal pressure and temperature estimates was needed. Holland and Powell came up with a solution to this problem by developing the now frequently used method; ´the average P-T method´. This method uses the least square method to find the average of calculated pressures from several independent reactions which represent all available equilibria in a rock. This gives the average pressure and temperature conditions of metamorphism (fig 5). In Optimal Geothermometry and Geobarometry (1994) Holland and Powell also press on the importance of including uncertainties and correlations of the calculated pressure (fig 5). The uncertainties in activities of end-members may originate from errors in the thermodynamic data eg. inaccurate enthalpies of the endmembers. Instrumental imprecision when measuring mineral composition and uncertain activity-composition relationships may also contribute to the uncertainties of the activity of the mineral end-members. Any uncertainty in the activity of mineral end-members pass on to lnK and thus also the position of the pressure and temperature estimate. Correlation between lnK values will occur directly when two reactions involve the same uncertain end-member. The correlation is important to include when combining many equilibria to estimate pressure and temperature. This is because movement of all points involving a specific end-member will occur in a predictable way if the activity of that end-member change (Holland & Powell 1994). Below (fig 5) the two ellipses define the regions for the conditions of equilibration in the pressure-temperature diagrams. A small ellipse suggests that all minerals have reached equilibrium and that the thermodynamic data, chemical analyses and activity models are of good quality. If equilibrium has not been attained or problems with the achieved data exists the pressure-temperature diagrams would contain reaction lines whose intersections would scatter across a larger area. Reaction-line c for example (fig 5b) could suggest this and might have to be excluded. However, if a good temperature estimate was added a smaller region for conditions of equilibrium could be achieved (Holland & Powell 1994).

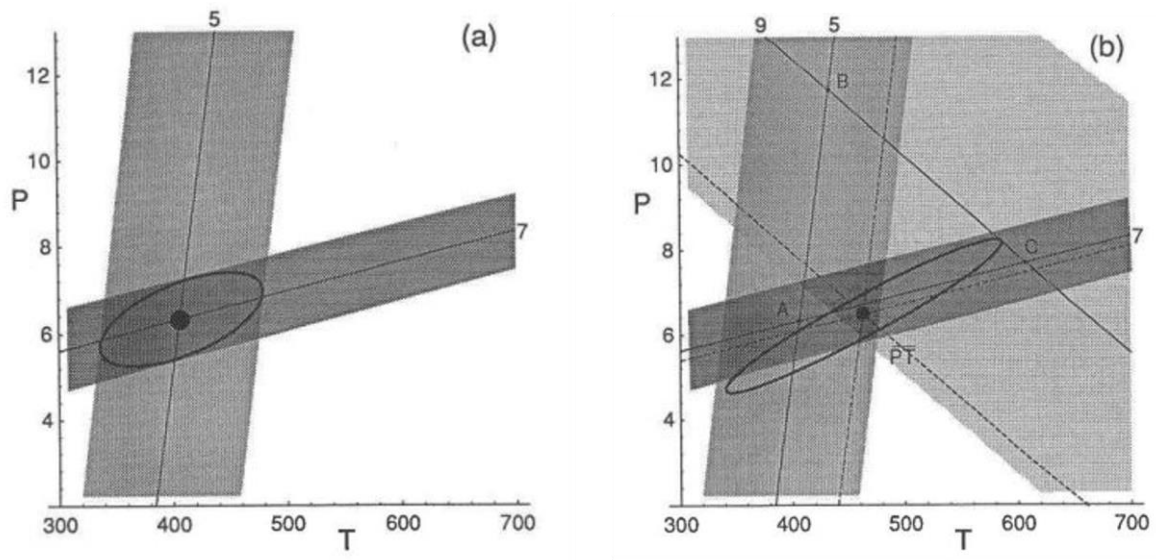

Figure 5. Pressure and temperature diagram showing how including uncertainties (grey areas) and several reactions (black lines) influence the point for pressure and temperature estimate (black dot). (a) Two reactions, one Geothermometer and one Geobarometer coalesce to give one P-T point. (b) One additional reaction with a large band of uncertainty (reaction-line c) has been added. The P-T point has moved and if a good temperature estimate can be added a well determined P-T estimate can be expected (Holland & Powell 1994).

2. Methods

2.1 Fieldwork: mapping and sampling

During 10 days in July mapping and collection of samples were carried out in the Tarfala Valley. 16 samples from 13 locations were collected and classified into 8 separate bedrock complexes. Due to garnet being an important indicator of pressure-temperature conditions used for geothermobarometry the most suitable samples included them. Some bedrock borders and sites were estimated from a distance and later compared to previous studies due to safety concerns. The mapping and measurements were accomplished by the use of an I-pad equipped with the app Field-move (Petroleum Experts 2015) and backed up by compass-clinometer measurements of the dip and dip-direction by hand.

2.2 Thin section preparation

All samples were taken to Stockholm University and trimmed down with a water-cooled diamond saw. Bulk material was reduced to sizes of approximately 2-4 cm^3 and cut perpendicular to foliation directions. The samples were then sent to Vancouver Petrographics (Canada) for further preparation of thin sections with standard thickness (30µm). In total 26 polished thin sections were prepared.

2.3 Petrographic analysis

During one week at Stockholm university the thin sections were analysed under optical microscope to determine their mineralogy and interpret their metamorphic evolution. One thin section, number 13 from sample 8 (fig. 6, A66, A70 & Table 1), was chosen to be focused on in this study. It was selected due to its content of both an amphibolite and a metapelite part.

2.4 Scanning Electron Microscopy (SEM) with Energy Dispersive Spectroscopy (EDS)

At the Laboratories for quantitative target mineralogy (QanTmin), Luleå University of Technology (LTU) the thin sections were analysed using a Scanning Electron Microscopy (SEM) with Energy Dispersive Spectroscopy (EDS). This work was supervised and explained by LTU Associated senior lecturer Thomas Aiglsperger. To prevent interference from surface charge and make the thin sections conductive to the electron dust they were first carbon coated. Carbon is suitable due to its low atomic number and that the peak of the Carbon X-ray graph is separate from the peaks of other elements. A ZEISS Sigma 300 VP scanning electron microscope fitted with energy dispersive spectroscopy was then used for the quantitative mineralogy.

The Scanning electron microscope operates by generating electrons which are accelerated towards an anode using high voltage. The electrons are then directed and through a series of passages and surrounding electromagnetic fields after which the focused electron beam is aimed and directed towards the sample. Mainly two physical phenomena occur when the electron beam hit the sample, generation of secondary electrons and backscattered electrons. These phenomena are then used for imaging. Energy of the incident electron beam generates secondary electrons originated in the sample which are then gathered and used by a detector to create a fluorescent material on its surface. A photomultiplier tube translates the fluorescent material to an electronic signal for which position is determined and compared to the position of the incident electron beam. Backscattered

electrons are the incident electrons which move around within the sample and then return out of the sample and detected by a high-definition backscattered detector (HDBSD). The backscattered electrons are used to identify areas with separate mean atomic number due to their lower energy level than secondary electrons and ability to expose the difference in absorption between elements. The mineral brightness on the screen is coupled to the atomic number. A heavy element will appear brighter than a light element.

In addition to imaging obtained by secondary and backscattered electrons chemical information is obtained by the fitted Energy Dispersive Spectroscopy detector (EDS). As secondary electrons are produced the affected atoms gets ionized and thus has to capture an outer shell electron to restore their ground state. This results in a photon being emitted due to the law of conservation of energy. The EDS detector then measures the energy of the emitted photon in the X-ray electromagnetic spectrum and compare it to the specific energy transitions of each element. The EDS detector is placed off axis from the incident electron beam and is composed by a crystal which is cooled down to superconductive temperature in order to achieve high quantum efficiency. With separation in to different energy channels the X-rays form a spectrum of energies with peaks that correspond to specific electron transitions. The specific electron transitions then relate and identify the corresponding element. The EDS technique coupled to the imaging of the SEM can also be used to form maps of data used for displaying high elemental concentrations (Carl Zeiss NTS ltd, 2011).

Running conditions

Running conditions for the SEM/EDS were as follows; Beam current= 464 Pa, Electron high tension (EHT) = 20.00kV and a working distance of 8.5mm.

2.5 Geothermobarometry- AX & THERMOCALC modelling

In this study, I used an activity-composition calculation program, AX_2 (Holland & Powell 1994) in which the SEM/EDS data were inserted. This data was recalculated by hand from obtained elemental composition to weight percent of oxides before being introduced to AX_2. The output file from AX_2 contain mineral endmember activities which can be inserted into the equilibrium constant expression for solving T and P. This file was then run in the software THERMOCALC 3.33 which uses ´the average P-T method´ and the P-T results could then be obtained (Holland & Powell, 1998).

3. Results

In this section I will present a geological map from the upper part of the Tarfala Valley along with descriptions of each unit which was mapped. The area of study and sampling is approximately 5km (north-south) and 3km (west-east) centred at approximately 67°55.35N / 18°35.24E in the Swedish part of the Scandinavian Caledonides (fig.6). Starting at the south from the valley Ladtjovagge the Tarfala Valley extend northwards toward the mountains Kaskasapakte and Kaskasatjåkka. The Kebnekaise massif, which is the highest mountain in Sweden borders the western side of the valley while the mountains Tarfalatjåkka, Tarfalapakte and Tarfalatjårro borders the eastern valley side. The Tarfala Valley floor rises from approximately 650 meters above sea level (MASL) in the south (measured by the Tarfala bridge with approximate coordinates; 67°52.08N / 18°39.03E) to approximately 1162 MASL in the north (measured on lake Tarfalajaure with approximate coordinates; 67°55.35N / 18°35.24E) forming an incision through the nappe succession. A large part of the area is covered with moraine, rockslide debris or glacial ice. Exposure of bedrock was sparse with increasing density higher up on the valley sides with steep inclination. Some of these sites were on steep slopes which could not be accessed safely. Within the mapped area, lower parts of the nappe succession dip approximately towards west to south-west and the upper parts of the nappe succession dips approximately towards north-west (fig. 7, A67-73). The measured dip-angle varies between 15° and 32° (fig. 7, A67-73).

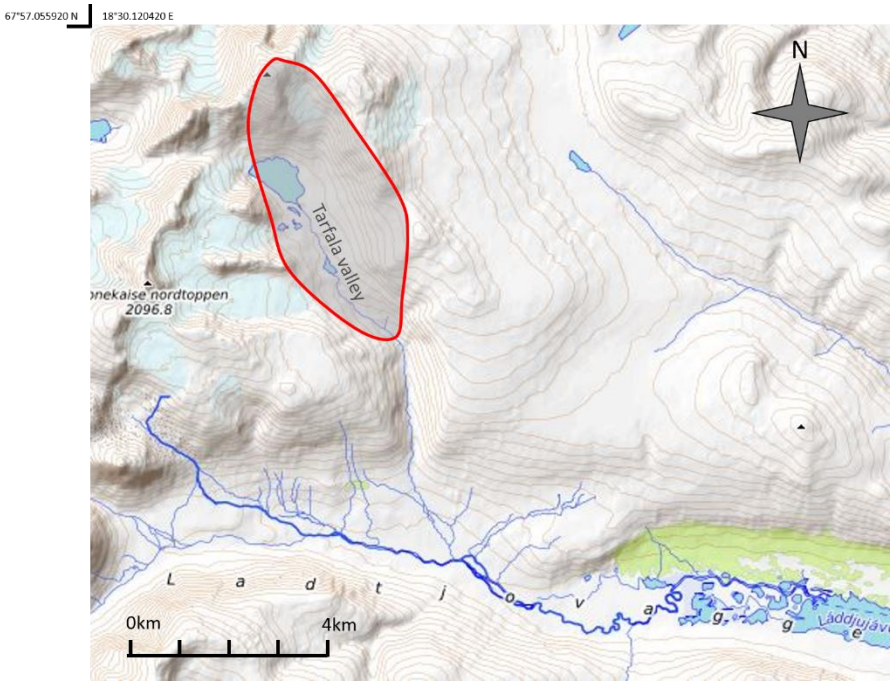

Figure 6. Tarfala Valley overview. The picture displays how the Tarfala Valley is located in relation to the larger Ladtjovagge in the south. The area surrounded by a red line shows the approximate research area for this study. The northern peak of Kebnekaise is annotated to the left on the map. Modified from (© OpenStreetMap contributors, 2022).

3.1 Geological map and corresponding description table

Below a Geological map (fig 7) with representative measurements is presented along with a related expositive table (table 1). For all measurements, see map-magnifications in appendix A.

Geological map

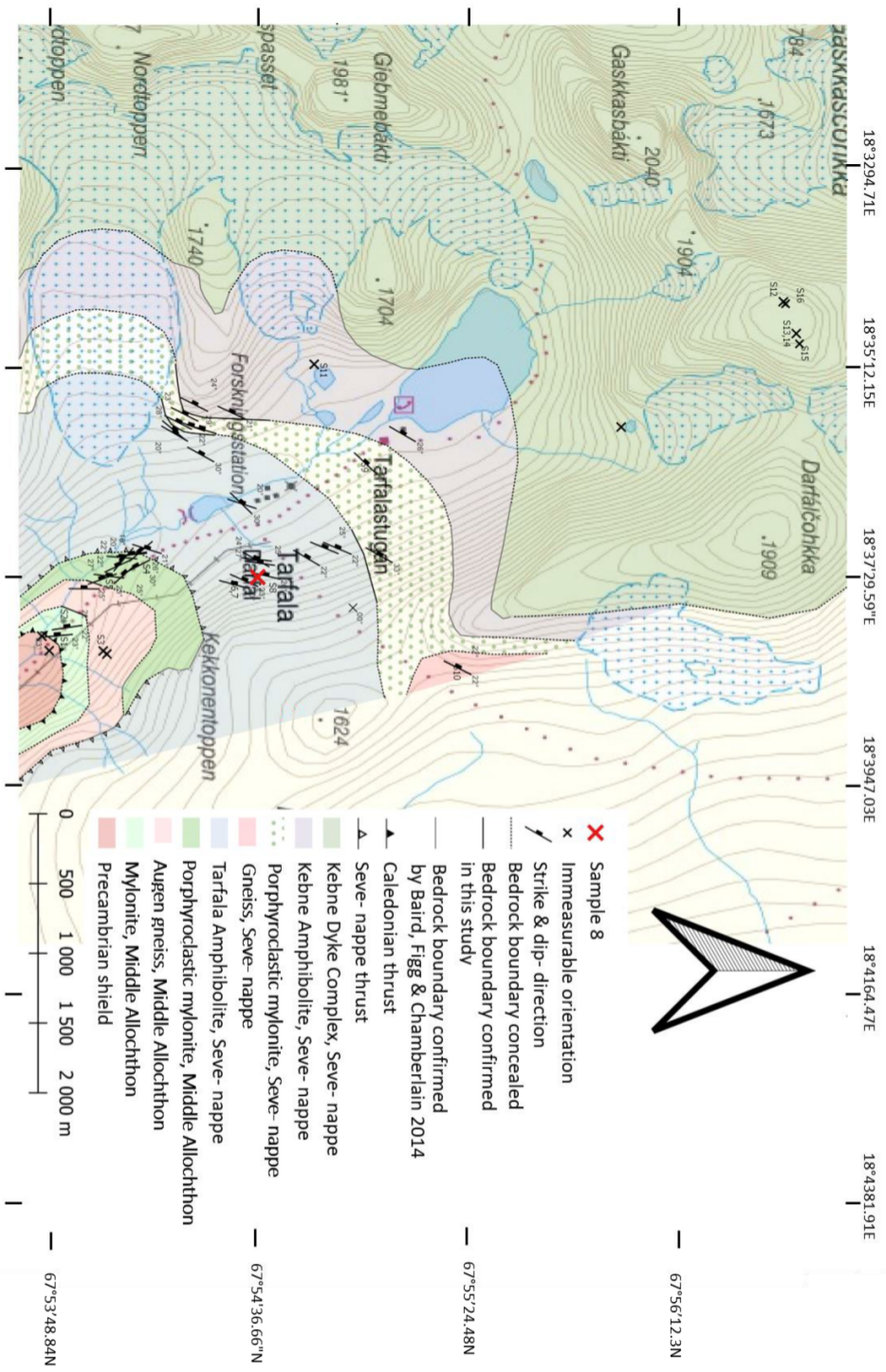

Figure 7. Geological map of the Tarfala Valley with representative values of selected locations for clarity. For full detail maps see Appendix A figure A67-73.

Table 1. List of collected samples with corresponding thin sections, locations and map-magnification in appendix.

Sample number	Thin-section number	Bedrock type	Thin section name	Location coordinates	Magnification number in Appendix
1	1	Mylonite	TA-MYL-L16-01	67°53'54.15"N/ 18°37'58.99"E	6
2	2	Mylonite	TA-MYL-L19-01A	67°53'57.02"N/ 18°37'53.37"E	6
2	3	Mylonite	TA-MYL-L19-01B	67°53'57.02"N/ 18°37'53.37"E	6
3	4	Augen Gneiss	TA-GNE-L13-01	67°54'04.80"N/ 18°38'07.25"E	6
4	5	Porphyroclastic Mylonite	TA-MEN-L11-01A	67°54'10.57"N/ 18°37'21.93"E	5
4	6	Porphyroclastic Mylonite	TA-MEN-L11-01B	67°54'10.57"N/ 18°37'21.93"E	5
5	7	Porphyroclastic Mylonite	TA-GNE/MEN-L12-01A	67°54'07.87"N/ 18°37'23.80"E	5
5	8	Porphyroclastic Mylonite	TA-GNE/MEN-L12-01B	67°54'07.87"N/ 18°37'23.80"E	5
5	9	Porphyroclastic Mylonite	TA-GNE/MEN-L12-01C	67°54'07.87"N/ 18°37'23.80"E	5
6	10	Tarfala Amphibolite	TA-AMN-L4-01	67°54'32.52"N/ 18°37'30.48"E	4
7	11	Tarfala Amphibolite	TA-AMN-L4-02A	67°54'32.52"N/ 18°37'30.48"E	4
7	12	Tarfala Amphibolite	TA-AMN-L4-02B	67°54'32.52"N/ 18°37'30.48"E	4
8	13	Tarfala Amphibolite	TA-AMN-L14-01	67°54'36.66"N/ 18°37'29.59"E	4
9	14	Porphyroclastic Mylonite	TA-MEO-L2-01	67°55'00.51"N/ 18°36'16.01"E	3
10	15	Gneiss	TA-MEO-L15-01	67°55'17.96"N/ 18°38'34.70"E	3
11	16	Kebne Amphibolite	TA-AMO-L1-01A	67°54'51.84"N/ 18°35'12.15"E	2
11	17	Kebne Amphibolite	TA-AMO-L1-01B	67°54'51.84"N/ 18°35'12.15"E	2
11	18	Kebne Amphibolite	TA-AMO-L1-01C	67°54'51.84"N/ 18°35'12.15"E	2
11	19	Kebne Amphibolite	TA-AMO-L1-01D	67°54'51.84"N/ 18°35'12.15"E	2
11	20	Kebne Amphibolite	TA-AMO-L1-01E	67°54'51.84"N/ 18°35'12.15"E	2
11	21	Kebne Amphibolite	TA-AMO-L1-01F	67°54'51.84"N/ 18°35'12.15"E	2
12	22	Kebne Dyke Complex	TA-KDY-L17-01	67°56'31.21"N/ 18°34'45.33"E	1
13	23	Kebne Dyke Complex	TA-KDY-L18-01	67°56'33.92"N/ 18°35'14.57"E	1
14	24	Kebne Dyke Complex	TA-KDY-L18-02	67°56'33.92"N/ 18°35'14.57"E	1
15	25	Kebne Dyke Complex	TA-KDY-L18-03	67°56'33.92"N/ 18°35'14.57"E	1
16	26	Kebne Dyke Complex	TA-KDY-L20-01	67°56'32.97"N/ 18°34'48.43"E	1

Table 1. List of collected samples with corresponding thin sections, bedrock-type, locations and map-magnification in appendix A. Sample number 1-5 belong to the Middle Allochthon and Sample number 6-16 belong to the upper part of the Middle Allochthon; Seve nappe. Sample 8 which in this study is investigated for metamorphic P-T conditions is highlighted. For sample locations see the referred magnification in appendix A.

3.2 Rock descriptions:

Below, you will find descriptions of the mapped rock units sequentially ordered, starting with the lowest Caledonian unit and moving upwards. Note that the underlying mapped Precambrian bedrock is excluded from this section due to the entirely visual estimation from a distance.

Mylonite (Middle Allochthon)

Resting on top of the Precambrian bedrock of the Baltic shield is a well-developed mylonite. The rock displays a distinct mylonitic foliation with altering bands of light and dark hues and an overall green hue of the rock is observed (Fig. 8). Grains are sheared to an unidentifiable state in hand- sample (fig.9). Centimetre- scale folding occurs in some locations (Fig. 8). A shallow dip towards west is shown by planar structures of the rock unit (fig.7 & A73). Samples collected: number 1 & 2 (fig. A67 & A73, Table 1).

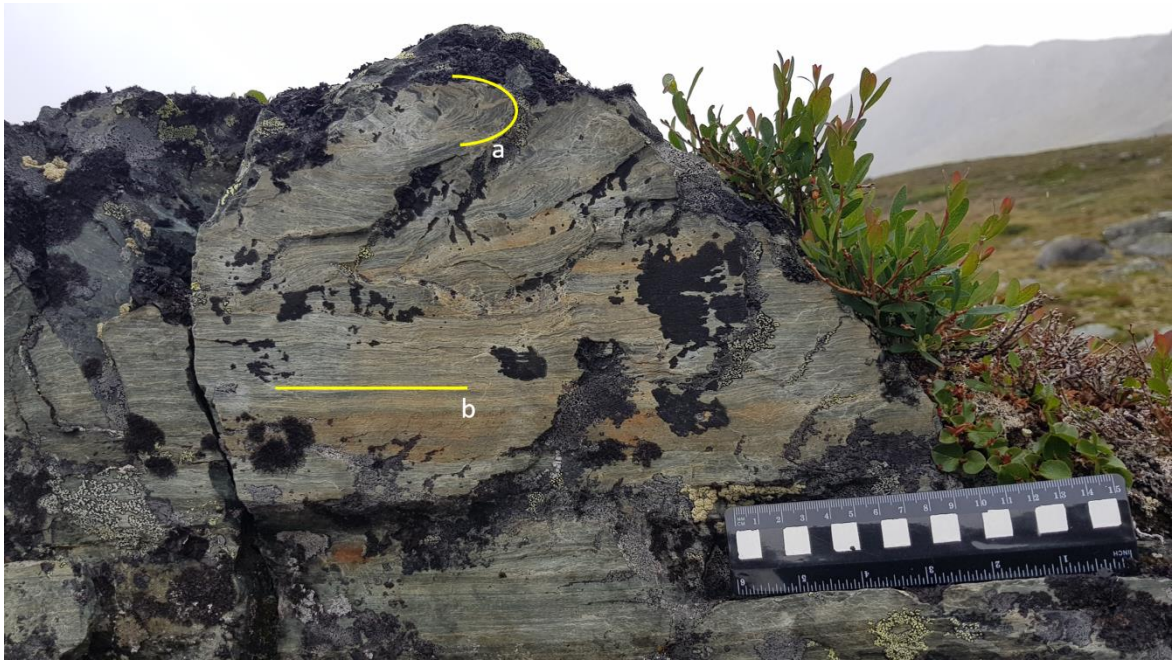

Figure 8. Outcrop surface in field, location is site of sample 2 with coordinates: 67°53'56.71"N/18°37'53.59"E (fig. A73) (a) example of centimetre-scale folding. (b) Orientation of foliation. Ruler for scale.

Figure 9. Close up of hand sample 2 (fig. A73 & table 1). (a) Foliation parallel to horizontal orientation of the image.

Augen Gneiss (Middle Allochthon)

A zone of Augen Gneiss sits structurally above the mylonite unit. The rock unit exhibits crystalline structure with clear foliation of medium to large grains. Small crystals of quartz and micas surround large K-feldspar crystals. The K-feldspar crystals are seen as lenticular Porphyroblasts (Augens) with sizes in the range of 1-5 mm (fig. 12). The westernmost location of this unit displays a planar surface with a shallow dip towards the west (fig.7, A73) in contrast to the eastern most location which displays no apparent orientation. A visual resemblance to sheared Granite was noted in field of the easternmost location (sample3, fig. A73). Samples collected: number 3 (fig. A67 & A73, table 1).

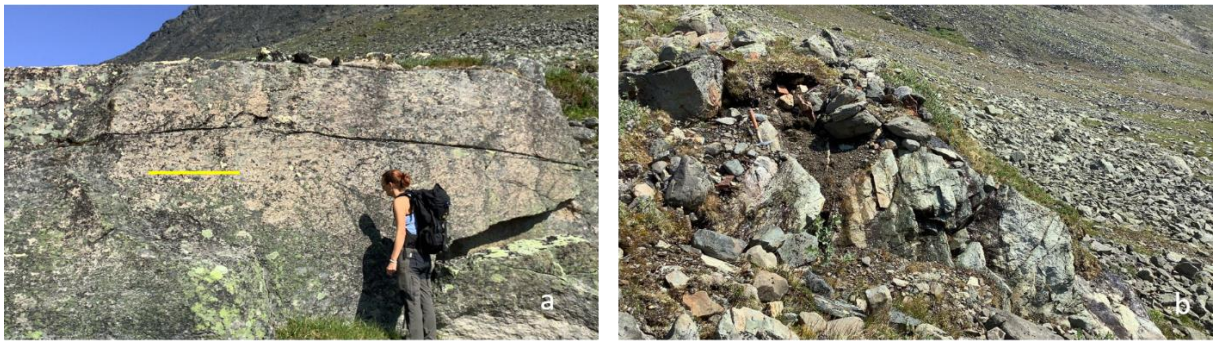

Figure 10. Outcrop on site of sample 3, (fig A73 & table 1). (a) View, approximately towards North-East. Yellow line show direction of foliation. (b) View, approximately towards South-East. Hammer for scale.

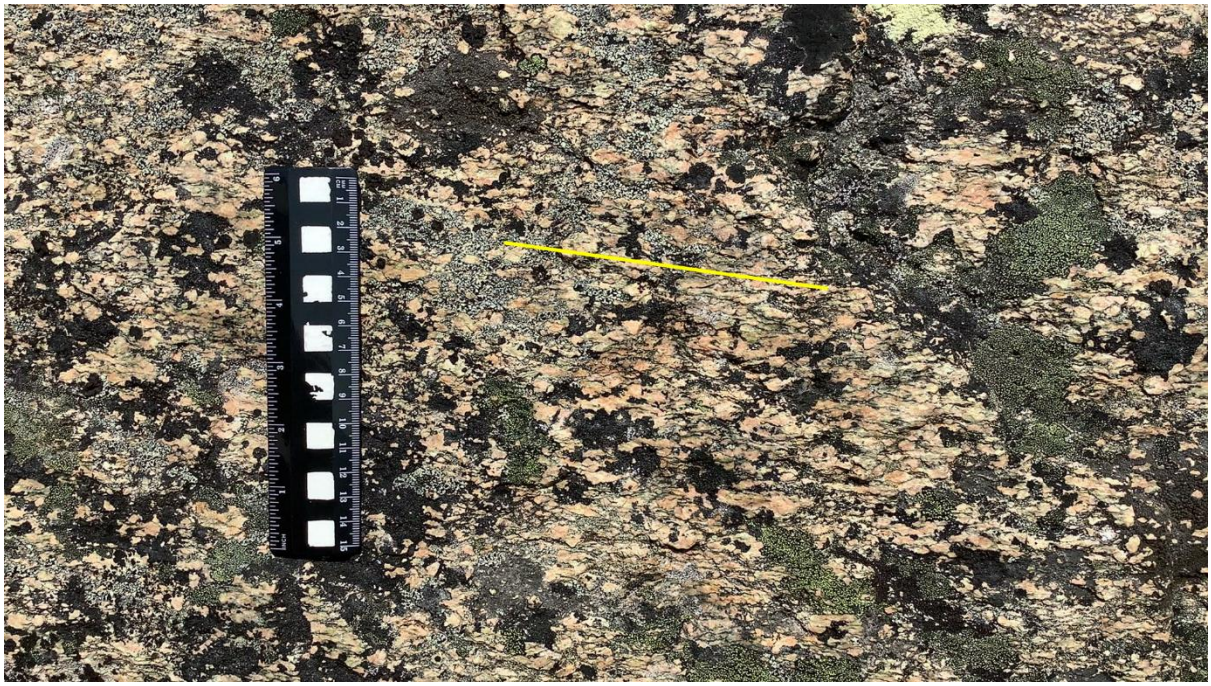

Figure 11. Close up of outcrop on site for sample 3 (fig. A73). Yellow line display orientation of foliation. Ruler for scale.

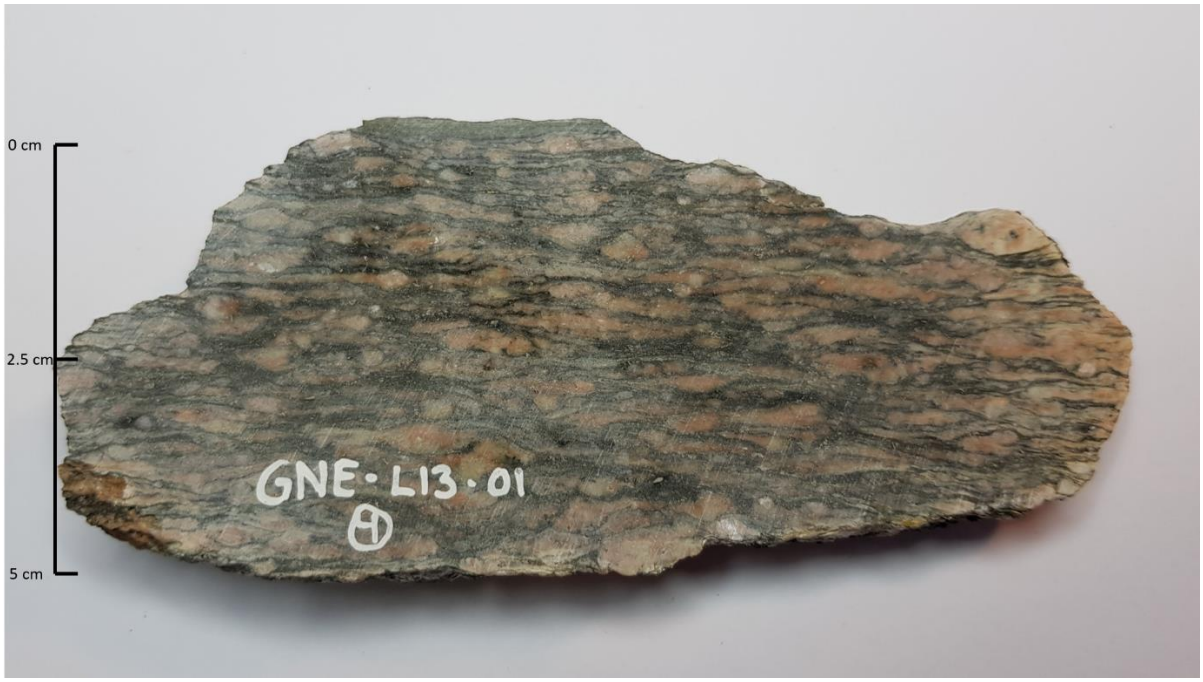

Figure 12. Hand-sample with cut surface from the easternmost location (sample 3) (fig. A73). The deformation of K-feldspar crystals (Augens) is clearly visible as foliation running parallel to the horizontal orientation of the picture.

Porphyroclastic mylonite (Middle Allochthon)

The bedrock unit sitting on top of the Augen Gneiss is another mylonite. Orientation of planar surfaces (fig 13a) in this unit is displaying a shallow dip towards west to south-west. In contrast to the previous mylonite, this mylonite displays less distinct banding and appears grey on fresh surfaces (fig. 13b). Weathered surfaces however display a brown hue due to muscovite content. Large deformed quartz-lenses of several centimetres (fig 15) are present along with porphyroclastic feldspar and garnets of approximately 0.5-1mm (fig 14). Samples collected: 4 (fig. A67 & A72, table 1)

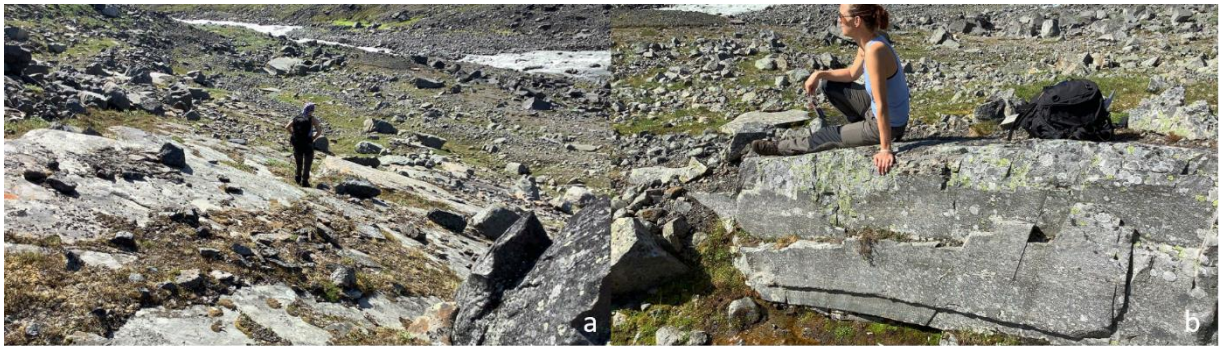

Figure 13. (a) Outcrop displaying a typical planar surface dipping towards the west, coordinates: 67°54'9.28"N / 18°37'23.03"E (b) Outcrop displaying a light grey hue, coordinates: 67°54'7.86"N/ 18°37'23.70"E

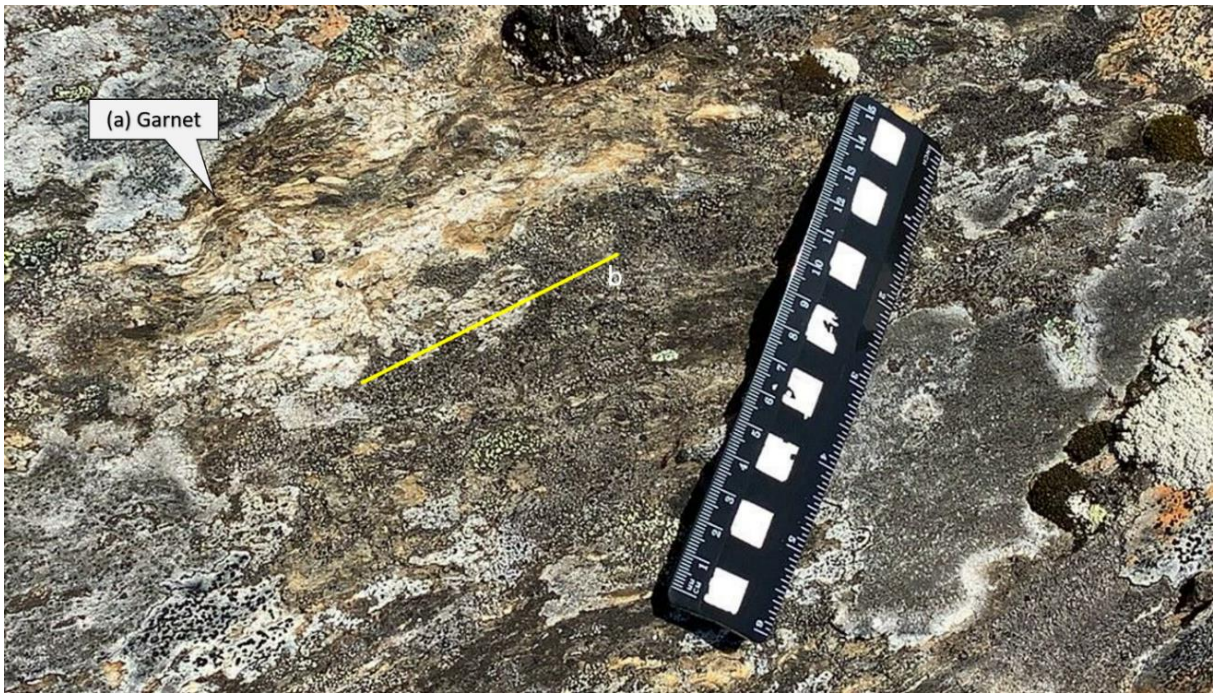

Figure 14. Close- up of surface displaying a slight brown hue. Ruler for scale. Coordinates: 67°54'10.67"N / 18°37'21.94"E. (a) Garnet. Note that the larger spot below to the right is not a garnet but a lichen. (b) Orientation of foliation.

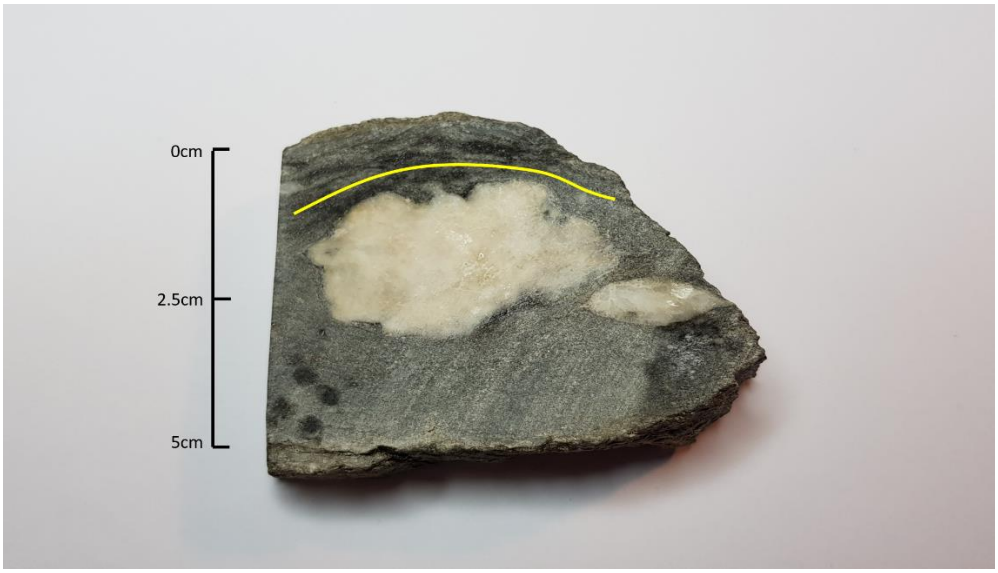

Figure 15. Cut surface of hand-sample (sample 4) (fig. A72 & table 1) with light grey appearance, displaying typical deformed Quartz lenses. Yellow line is showing the foliation plane and deformation around the quartz-lens.

Tarfala Amphibolite (Seve nappe, upper Middle Allochthon)

The Tarfala Amphibolite sits structurally above the Augen mylonite which was previously described. Orientation of planar structures exhibits a shallow dip towards west to north-west however some sites close to the underlying bedrock-unit exhibits a shallow dip towards West to south-west (fig. A72). The bedrock in this zone is a hornblende rich amphibolite which exhibits clear foliation parallel with the cleavage of the rock. Grain sizes are under 1mm and sporadically narrow bands of feldspar containing garnets are found. Near the contact with the underlying mylonite unit, fold structures visible as large bulging surfaces are found (fig.17). This study focuses on a sample (sample 8, fig. 7 & A71) from the Tarfala Amphibolite unit. The focus-sample was chosen due to a narrow, garnet rich pelitic layer (fig.19) running through the hornblende-rich amphibolite. Samples collected: 6-8 (fig. A67 & A71, table 1).

Figure 16. Outcrop displaying a typical appearance for the Tarfala Amphibolite. Cleavage of the rock in the picture is parallel to the foliation. Picture view is approximately north, coordinates: 67°54'22.56"N/ 18°35'50.46"E

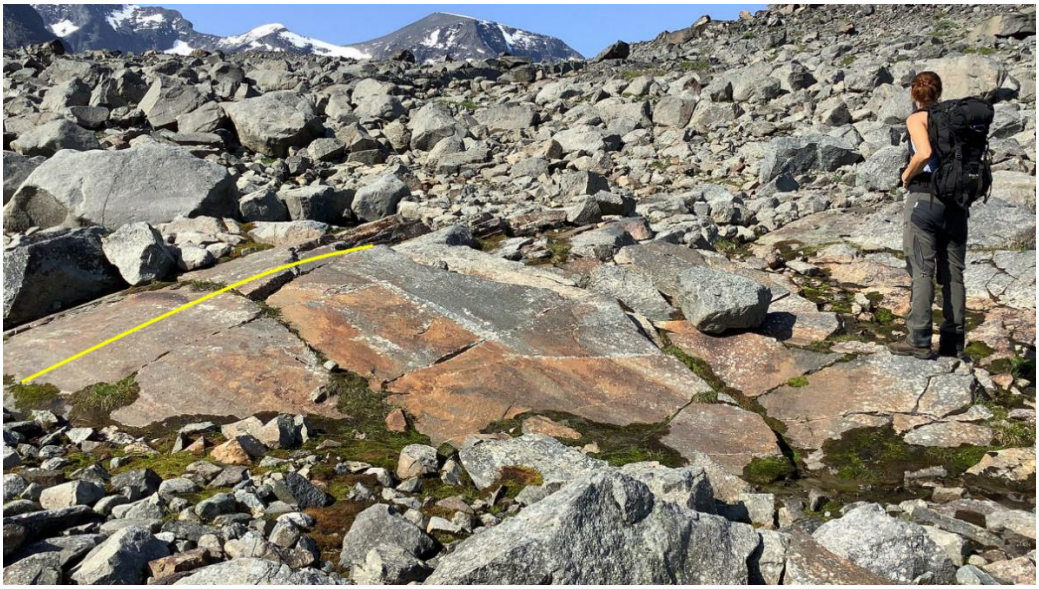

Figure 17. Outcrop with large bulging surface. Picture view towards north, Kaskasatjåkka mountain in the middle background. Fold hinge is marked with the yellow line. Coordinates: 67°54'12.89"N/ 18°37'10.50"E

Figure 18. (a) Close-up of weathered surface. Yellow line is parallel to foliation and cleavage. Ruler for scale. (b) Close-up of fresh surface. Yellow line is parallel to foliation and cleavage. Ruler for scale.

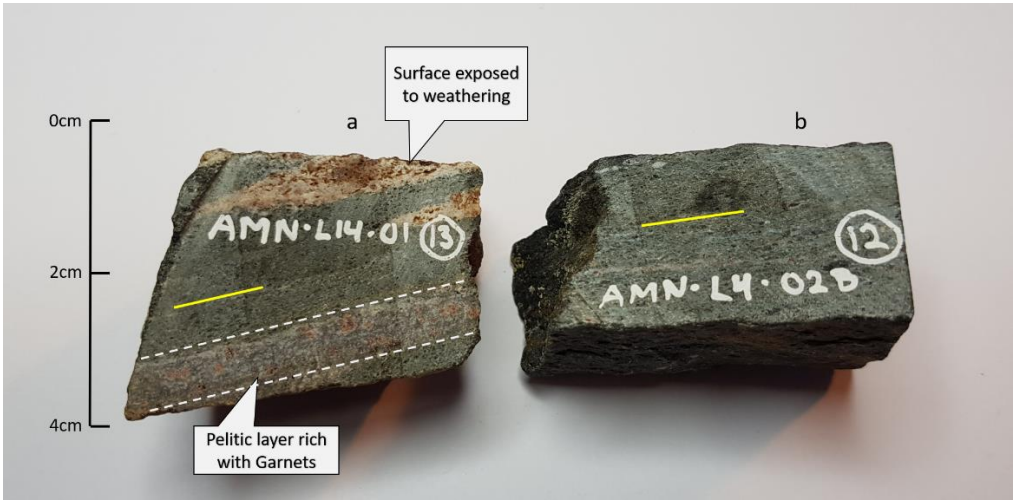

Figure 19. Hand- samples of the Tarfala Amphibolite with cut surfaces. Yellow line is parallel to foliation. (a) Sample 8, which in this study are examined for pressure and temperature (fig.71 & table 1). (b) Sample 7 (fig.71 & table 1).

Porphyroclastic mylonite (Seve nappe, upper Middle Allochthon)

Stratigraphically this zone lies between two amphibolite units, the underlying Tarfala Amphibolite and the overlying Kebne Amphibolite (fig.7). A shallow dip towards north-west dominates the planar structures in this zone (fig. A67, A69-A70). The texture is weathered mylonitic and the weathered surfaces displays a distinct brown hue due to the muscovite present in the rock. Foliation is clear and in the same orientation as the cleavage of the rock (fig 21). Deformed, elongated porphyroclasts of feldspar with sizes ranging from millimetre-scale to a couple of centimetres is common (fig. 21-22). Garnets with sizes up to 1mm also exists in this unit (fig22). Compared to the porphyroclastic mylonite of the Middle Allochthon, this mylonite is similar but contains more and larger porphyroclasts. A slightly darker and pink hue is also significant for this unit. Samples collected: 9 (fig. A67 &A70, table 1).

Figure 20. (a) Outcrop of site of sample 9 displaying a planar surface towards north-west (fig. A70 & table 1) View towards South-East. (b) Outcrop, coordinates: 67°54'24.24"N/ 18°35'40.49"E. Cleavage of the rock shown in this picture follows the orientation of the foliation.

Figure 21. Close-up of surface displaying Feldspathic porphyroclasts. Ruler is parallel to foliation and cleavage. Coordinates: 67°54'23.95"N/ 18°35'38.03"E.

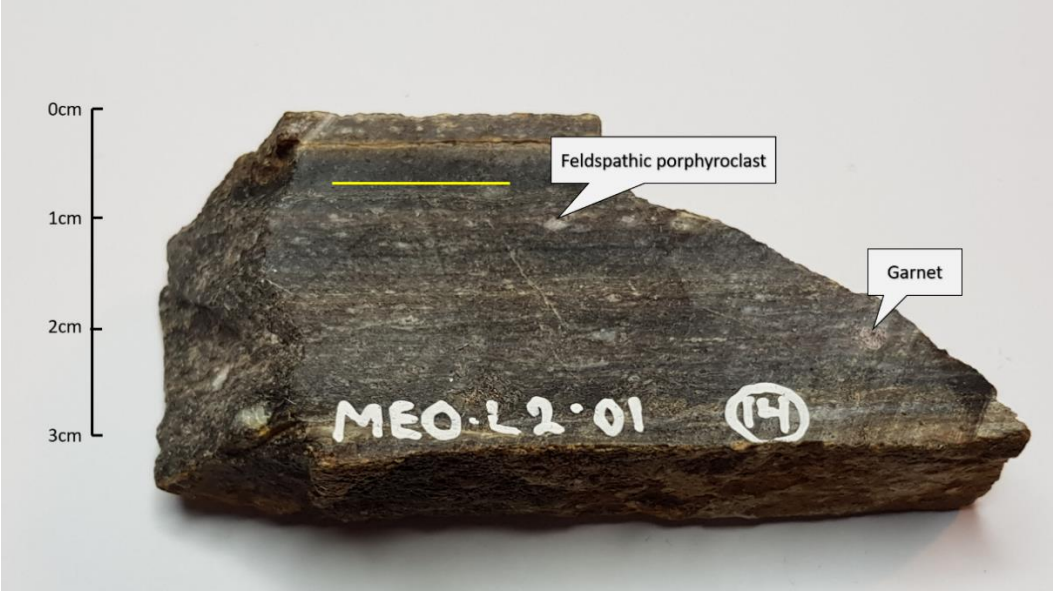

Figure 22. Sample 9, displaying Feldspathic porphyroclasts and Garnet on cut surface (fig. A70 & table 1.) Yellow line is parallel to foliation.

Gneiss, (Seve-nappe, upper Middle Allochthon)

One site to the east of the previously described Porphyroclastic mylonite of the Seve-nappe consists of gneiss (sample 10, fig. A67 & A70, table 1). This site displays a shallow dip towards North-West. Foliation and discrete banding occur parallel to cleavage in the rock. However, the foliation is much less pronounced than in the previously described augen-gneiss and mylonites. The colour appearance is light grey. Feldspathic eyes occurs occasionally and not as frequent and large as in the before mentioned porphyroclastic units. Garnets are sparsely scattered throughout the rock with sizes up to approximately 3mm (fig. 24). Samples collected: 10 (fig. A67 & A70, table1).

Figure 23. Outcrop from site of sample 10 (fig. A70 & table 1) displaying cleavage parallel to the yellow line. Discrete banding can be seen but are somewhat obscured by the cleavage in the picture. Water-bottle for scale reference.

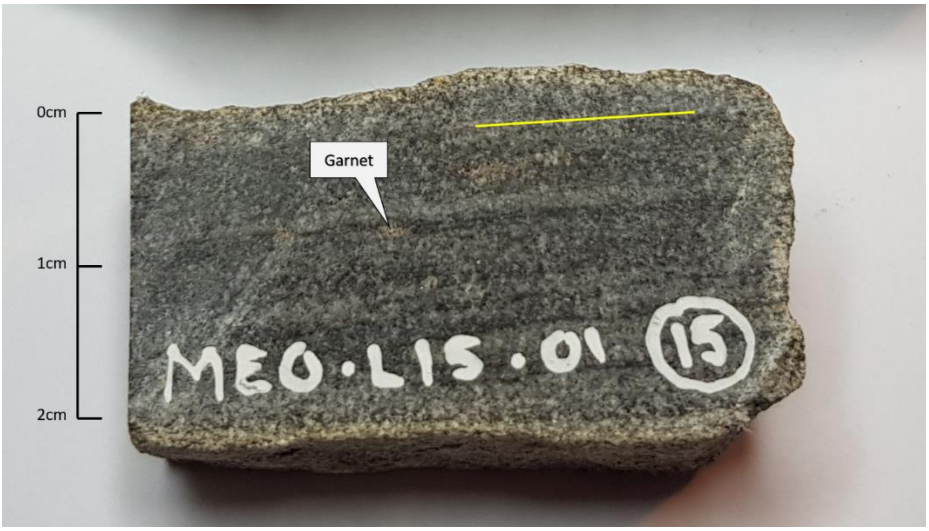

Figure 24. Cut surface of sample 10 (fig.70 & table 1). Yellow line display orientation of foliation and the discrete banding. Small deformed garnets are visible.

Kebne Amphibolite (Seve nappe, upper Middle Allochthon)

The Kebne Amphibolite is situated structurally above the porphyroclastic mylonite of the Seve-nappe which separates it from the Tarfala Amphibolite (fig.7). Planar structures are oriented with dip-direction towards West to North-West with a shallow dip angle. The planar structures coincide with foliation in the rock which is visible due to elongated Hornblende crystals. The unit exhibits very similar qualities to the Tarfala Amphibolite although the cleavage is less pronounced in the Kebne Amphibolite. Small scale folding occurs sporadically but larger folds are indicated high up in inaccessible areas. Visible hornblende crystals dominate this rock with subordinate feldspar and garnets that often are located in veins running parallel with foliation. Occasional signs of metasomatism are found throughout the unit seen as irregular light fields of feldspar, epidote and garnets (fig. 26). Samples collected: 11 (fig. A67 & A69, table 1).

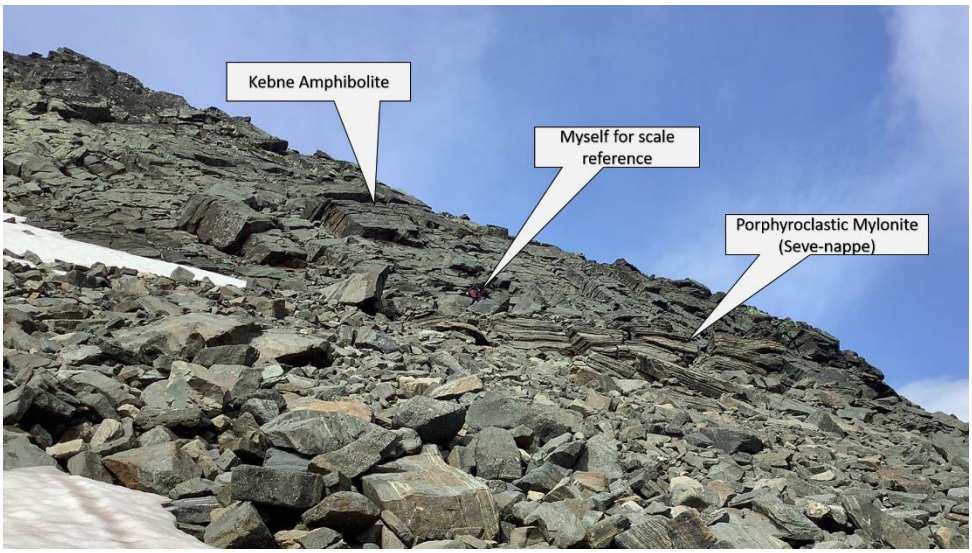

Figure 25. Contact between the Kebne Amphibolite and Porphyroclastic mylonite (Seve-Nappe). Kebne Amphibolite displays a typical appearance for the unit locations with steep inclination. The planar surfaces of the Kebne Amphibolite dips shallow towards North-West (fig. A67 & A69-A72). Coordinates: 67°54'25.10"N/ 18°35'37.11"E

Figure 26. Close-up of a Kebne Amphibolite outcrop (Sample 11, fig. A69 & table 1) with signs of Metasomatism. Yellow line display foliation direction. Glove for scale reference.

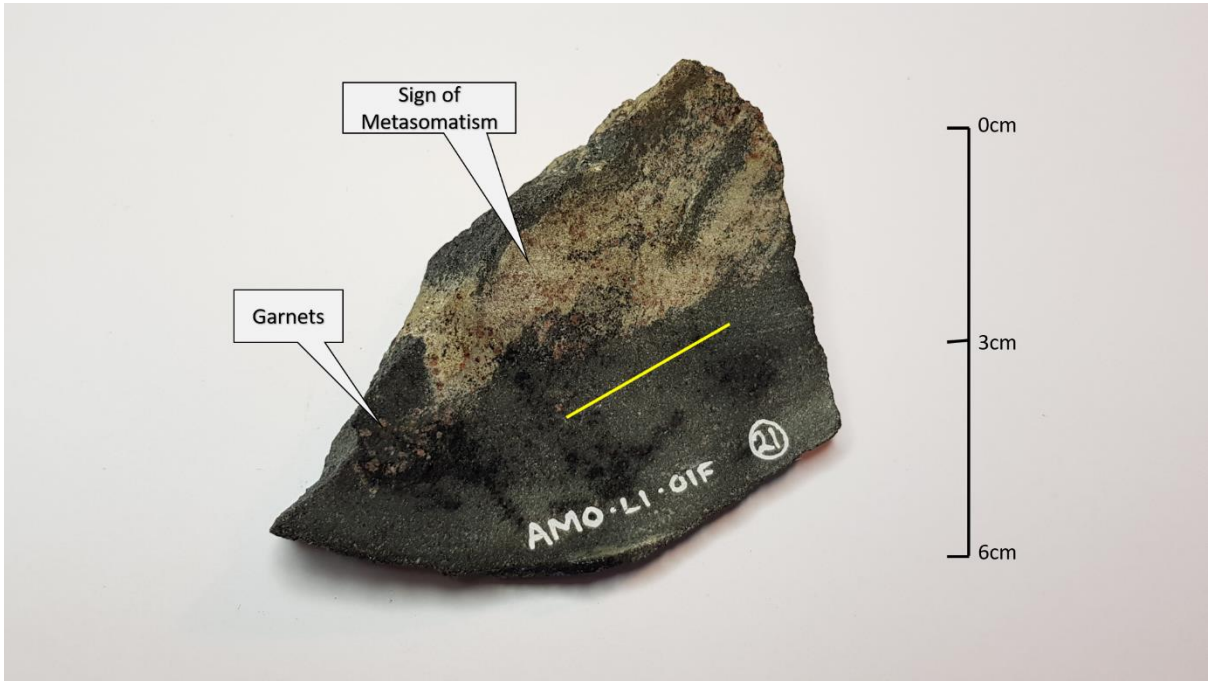

Figure 27. Sample 11 (fig. A69 & table1). Dark area is dominated by Hornblende crystals. Signs of Metasomatism are visible as light areas in the rock. Garnets are present and focused in and close to the Metasomatic altered area. Yellow line displays orientation of foliation.

Kebne Dyke Complex (Seve nappe, upper Allochthon)

The Kebne Dyke Complex sits structurally atop the Kebne Amphibolite and make up the highest bedrock unit mapped in this study (fig7). The localities of the Kebne Dyke Complex unit exhibit no measurable planar structures or foliation although a minimal amount of foliation is faintly hinted at some locations. Over all the Kebne Dyke Complex unit lacks apparent deformation. The zone contains two types of rock which both have phaneritic structure but is separated by one being slightly darker with smaller crystals. In hand-sample, mainly crystalline pyroxene and plagioclase can be identified. In addition, the Kebne Dyke Complex unit displays some evidence of later fluid-rock interaction indicated by veining (fig. 29-30). Several locations also contain xenoliths which occurs as irregular and angular areas, embedded in the lighter rock-type of the Kebne Dyke Complex (fig. 30). The xenoliths resemble the darker rock-type of the Kebne Dyke Complex and contains smaller crystals. Noted is that the veins cross-cuts the xenoliths. Samples collected: 12-16 (fig. A67 & A68, table 1).

Figure 28. Outcrop displaying a light colour. Compass for scale reference. Coordinates: 67°56'32.10"N/ 18°34'46.73"E.

Figure 29. Outcrop displaying a darker colour and veining. Compass for scale reference. Coordinates: 67°56'32.10"N/ 18°34'46.73"E.

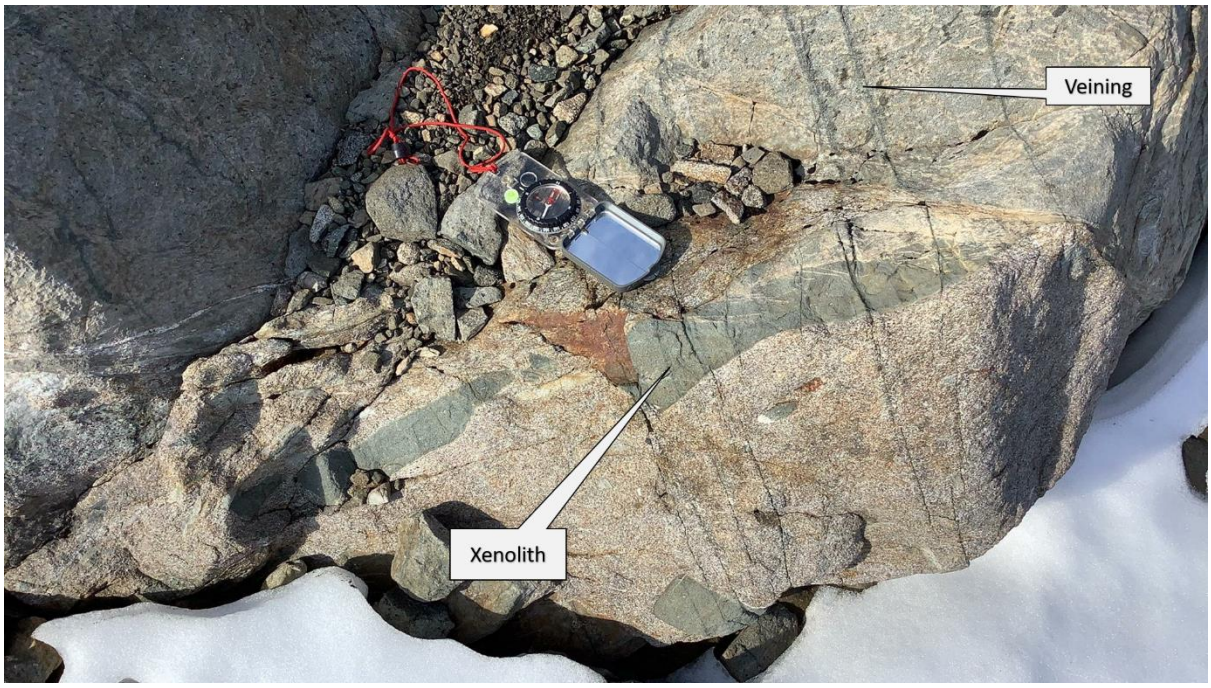

Figure 30. Outcrop displaying Xenoliths and veining. Compass for scale reference. Coordinates: 67°56'34.27"N/ 18°35'17.08"E

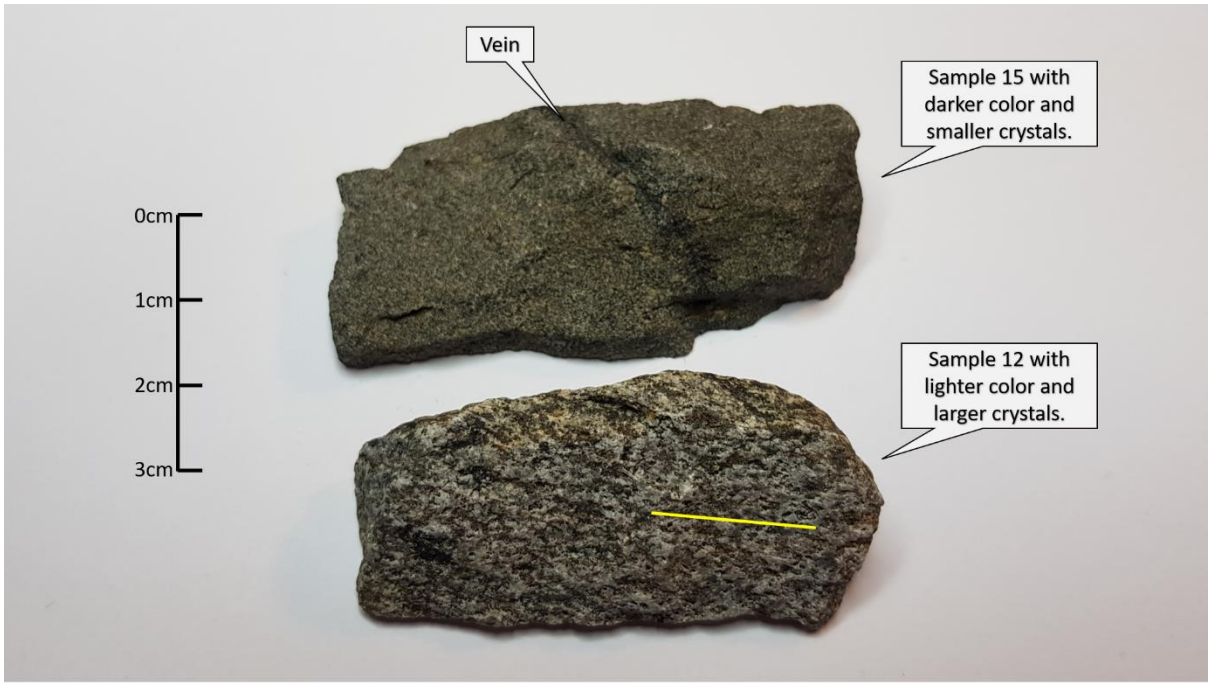

Figure 31. Sample 15 (top) and sample 12 (bottom). Yellow line display orientation of minimal foliation.

3.3 petrographic microscopy.

This section contains a presentation of the petrographic microscope-examinations of the thin-sections. The bedrock units are described below by using one representative thin-section each, however some bedrock-units are described by using an additional second thin-section as well. In total 26 thin-sections were studied at Stockholm University, department of Geological sciences. Each of the mapped bedrock-units are presented in order, starting with the lowermost unit. Note that the Precambrian bedrock is excluded due to the unit being entirely mapped by distance and no samples were retrieved.

Mylonite (Middle Allochthon)

Classification as a mylonite is based on the texture which show strong mylonitic foliation of the matrix with ductile deformation. The rock contains porphyroclasts which show signs of brittle deformation. All thin-sections of this bedrock unit contain feldspar, quartz and micas. In thin- section 2 (fig. 32 &table 1), feldspar occurs as small plagioclase porphyroclasts within a quartz and mica matrix (50-90%). A banded appearance of the matrix is visible in plane polarized light where dark bands are mainly biotite and light bands are mainly muscovite and quartz. The plagioclase porphyroclasts display proof of both ductile deformation, elongation in the direction of shear-planes, and brittle deformation consisting of microcracks. Both growth twinning and deformation twinning of the plagioclase is found, however the latter is more common. Quartz appears as small grained ribbons displaying recrystallization with grain boundary migration. The micas also display proof of ductile deformation with foliation along shear-planes, creating a banded impression together with the quartz. Small mica-fish is found which indicates the shear sense together with microscale folding (fig 32).

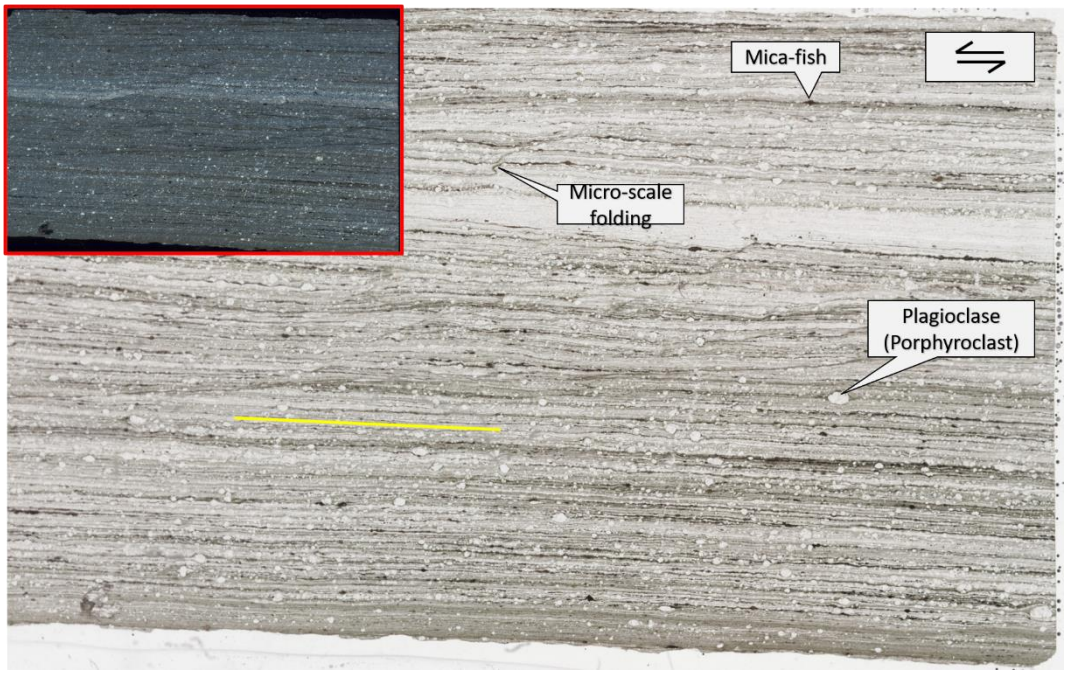

Figure 32. Scanned Thin-section (no;2, table 1) in plane polarized light (small inlet picture display the same view in crossed polarized light). Picture show a Sinistral movement indicated by micro-scale folding, Mica-fish and deformed Porphyroclasts of Plagioclase. The yellow line show foliation plane orientation.

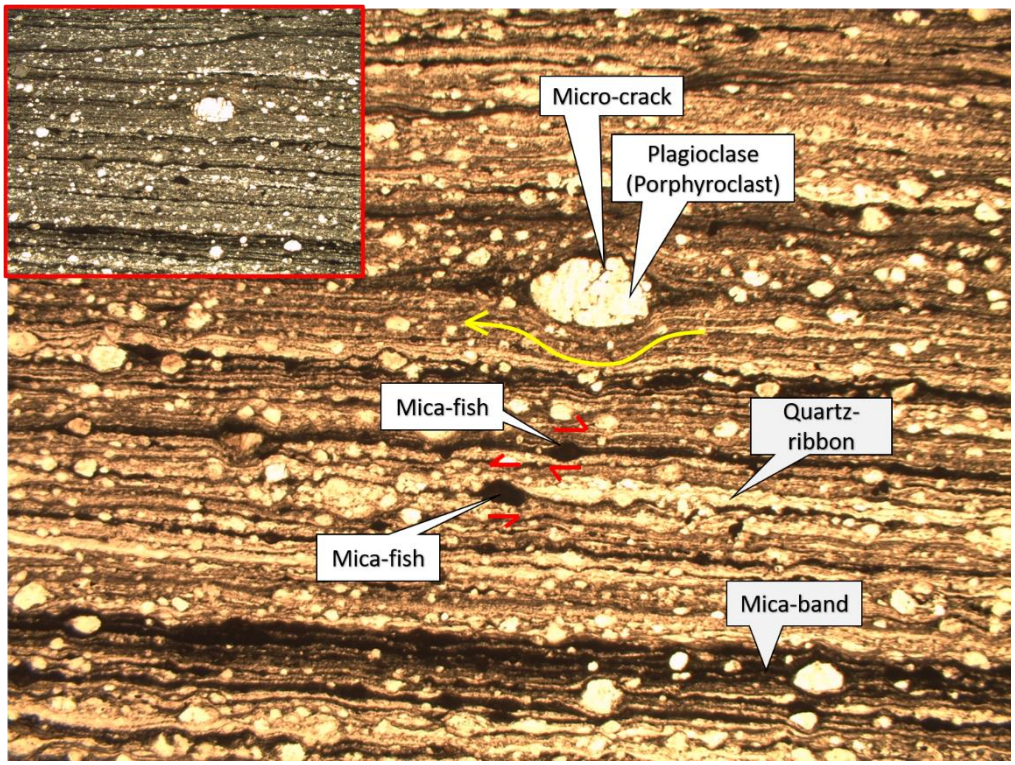

Figure 33. 2.5X magnification in Plane polarized light (inset picture show same view in crossed polarized light). The yellow arrow display plastic deformation around the Plagioclase porphyroclast. Micro-cracks in Plagioclase indicate brittle deformation. Note that the two Mica-fish crystals indicate Sinistral and Dextral shear-sense respectively.

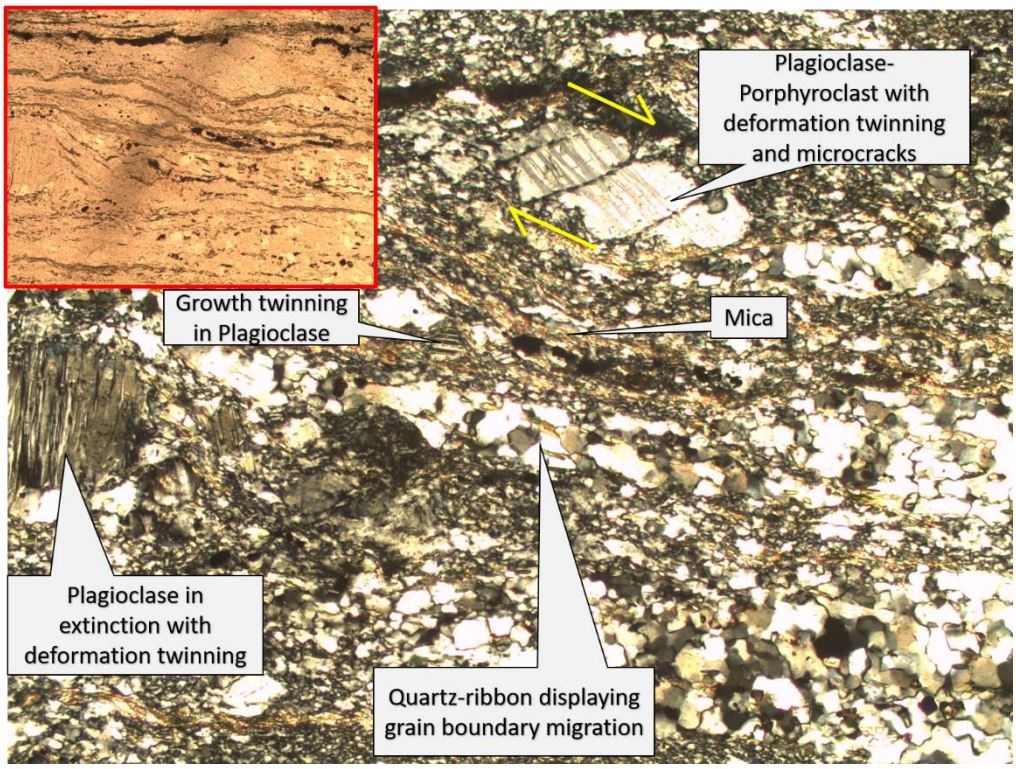

Figure 34. 10X magnification in crossed polarized light (small inlet display the same view in plane polarized light). Plagioclase porphyroclasts mostly display deformation twinning however some growth twinning can still be located. Brittle deformation, shearing and rotation Is apparent in the large un-extinct Plagioclase crystal. Mica, is foliated along shear-sense direction. Quartz crystals aligned in ribbons display plastic deformation and recrystallization by grain boundary migration.

Augen Gneiss (Middle Allochthon)

Very coarse grains (up to 0.6mm) of K-feldspar augens dominates this bedrock unit. Approximately 50-70% of the total crystal content consists of feldspars. The deformed groundmass surrounding the K-feldspar augens consists of quartz, plagioclase, micas (muscovite and biotite) and small amounts of rutile. The K-feldspar crystals are lenticular augens, sometimes with long tails grown by pressure-solution, that display two types of alteration features. Some of the K-feldspar augens displays a poikiloblastic texture with subgrains parallel to the (010) and (001) plane. Quartz appears as a mosaic texture with crystals displaying grain boundary migration, often located in halos surrounding the K-feldspar augens. The quartz crystals are also aligned in bands throughout the matrix which surrounds the K-feldspar augens. The micas, predominantly muscovite, are aligned along the foliation plane displaying a flaky appearance. The interference colour of the micas is moderate to strong and the crystals display birdseye extinction. Rutile appears as an accessory mineral visible as brown subhedral crystals with high relief. Signs of the rutile being affected by brittle deformation exist with small crystal pieces broken off and moved in the direction of foliation. In some of the resulting cleavage zones new rutile crystals have formed.

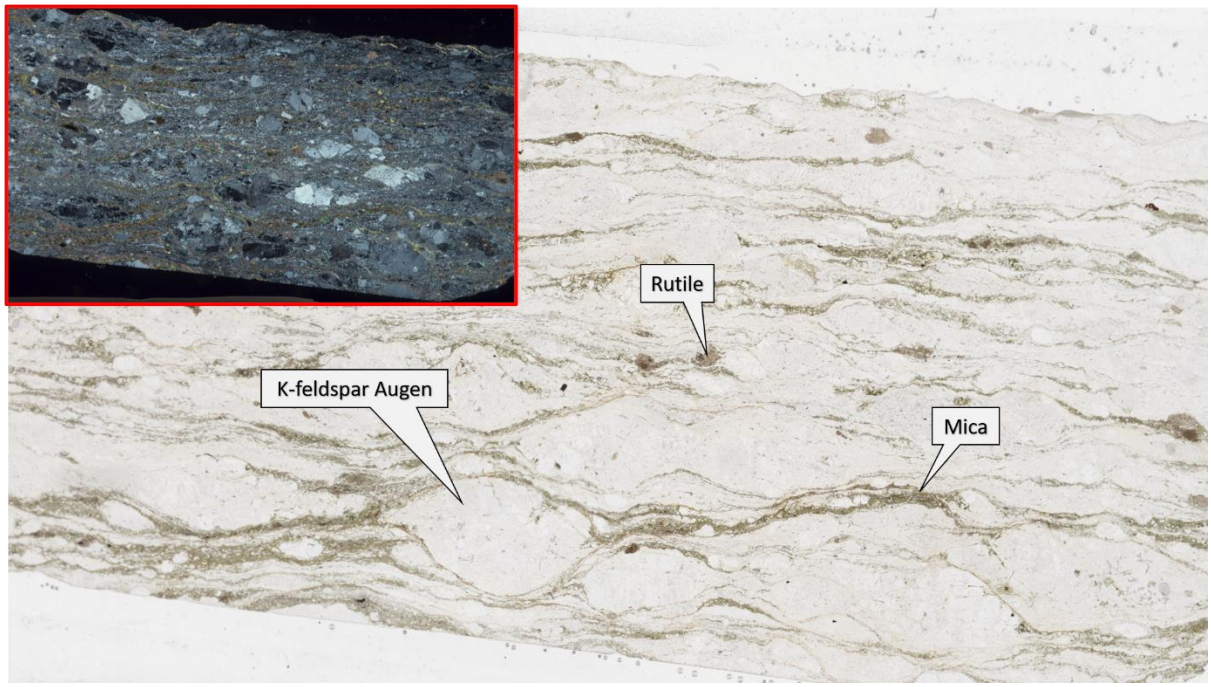

Figure 35. Scanned Thin-section (no. 4, table 1) in plane polarized light (small inlet picture displays the same view in crossed polarized light).

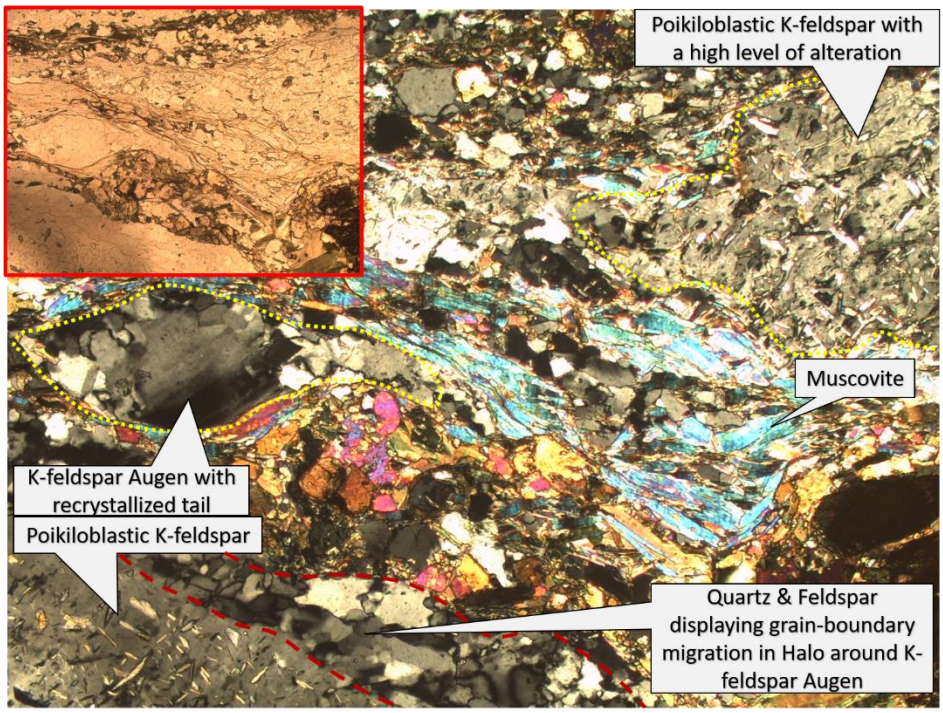

Figure 36. 2.5X magnification in crossed polarized light (small inset picture displays the same view in plane polarized light). Tails of recrystallize K-feldspar extruding from the Porphyroblast-augens can be seen in this picture growing in the direction of foliation. The elongated inclusions in K-feldspar (down left corner) are aligned parallel to the (010) and (001) crystal faces. The K-feldspar Augens are also surrounded by a halo of mixed quartz and feldspar displaying grain boundary migration. Quartz crystals can also be found aligned in bands parallel to foliation direction. The Muscovite are also aligned parallel with foliation and are easily located in crossed polarized light by displaying 3rd order interference colours

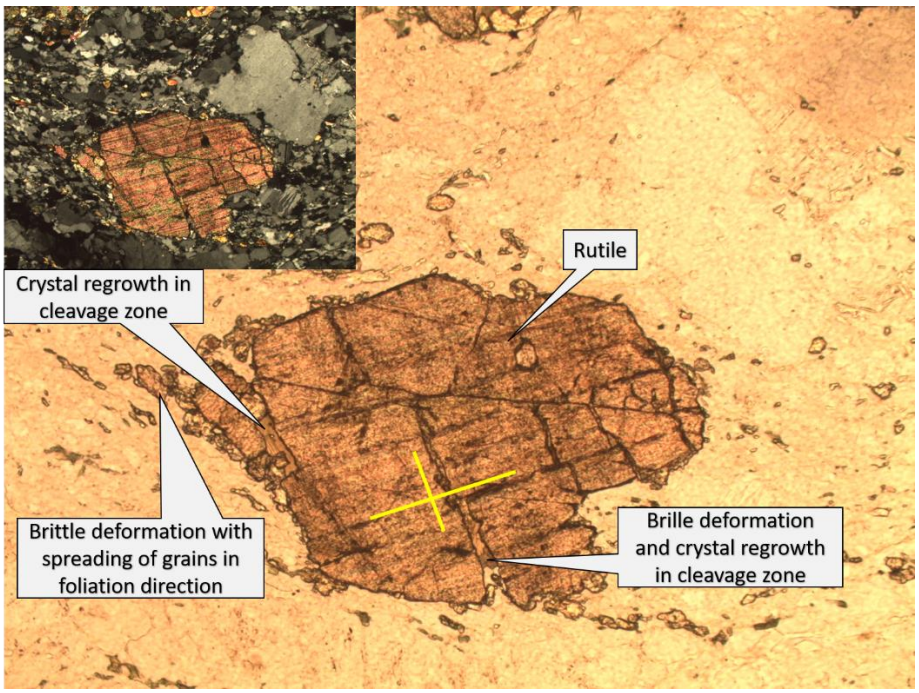

Figure 37. 10X magnification of a Rutile crystal within a matrix consisting of plagioclase and quartz. Yellow line displays orientation of the two directions of cleavage. Widening of the cleavage fractures by brittle deformation cause recrystallization within the fractures.

Porphyroclastic mylonite (Middle Allochthon)

Micas, quartz, feldspar, calcite, garnet and sillimanite surrounds very large quartz lenses in the thin sections of this bedrock unit. The classification as a mylonite is based on the texture which is composed of very flattened minerals in a strongly foliated and fine-grained matrix except for the large quartz lenses and garnets. The matrix crystals have aligned and created a banded appearance visible in thin section. Approximately equal parts of quarts and micas constitutes the matrix with lesser amount of calcite and sillimanite. Biotite is often found bordering the quartz lenses and in direct contact with the garnets. The sillimanite appear as small fibrous branches protruding from the mica crystals (fig 39). The quartz lenses contains intergrown, anhedral calcite crystals recognized by its high order birefringence and twin lamellae. Subhedral lenticular-shaped garnets are scattered sparsely throughout the thin-section (no;6, fig 38 & table 1).

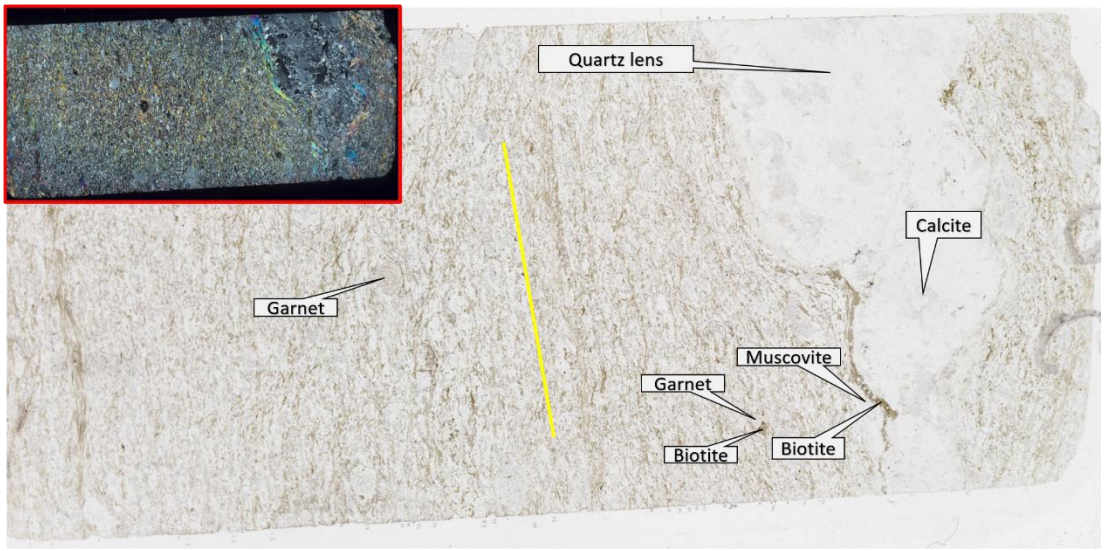

Figure 38. Scanned thin section (no.6, table 1) in plane polarized light (inset picture displays crossed polarized light). Yellow line show orientation of foliation. The Calcite is intergrown in the Quartz lens.

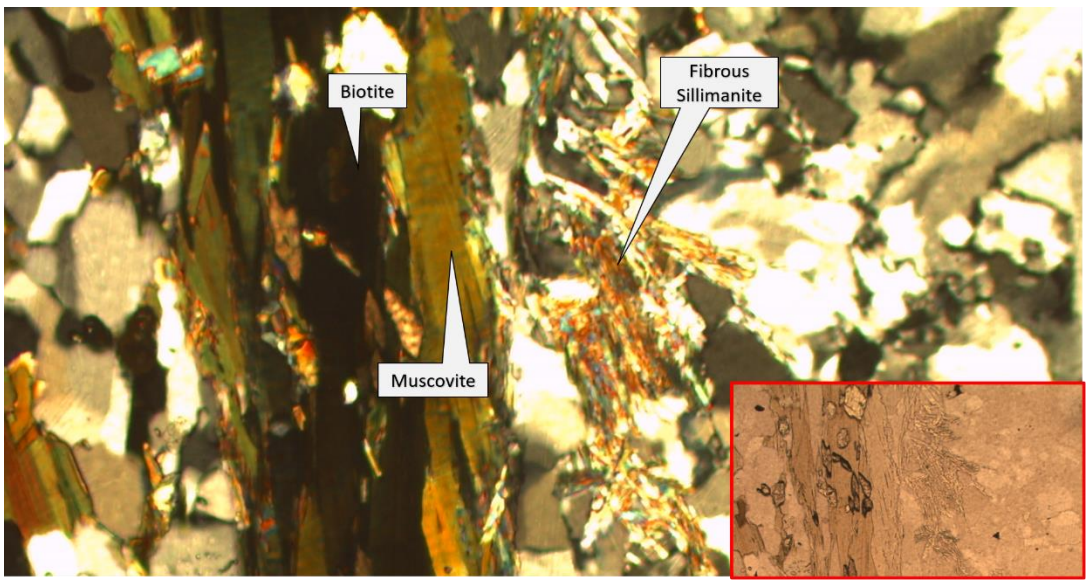

Figure 39. 10X magnification (thin-section no 6, table 1) displaying Biotite, Muscovite and Sillimanite.

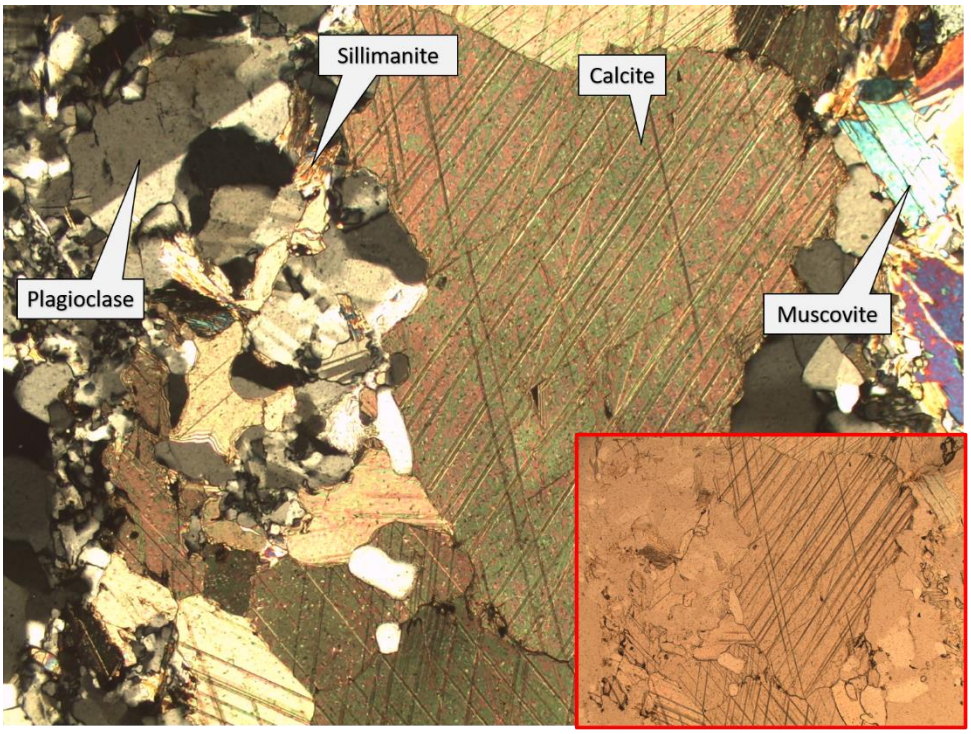

Figure 40. 10X Magnification (thin-section no 6, table 1) displaying Calcite, Plagioclase, Muscovite and Sillimanite.

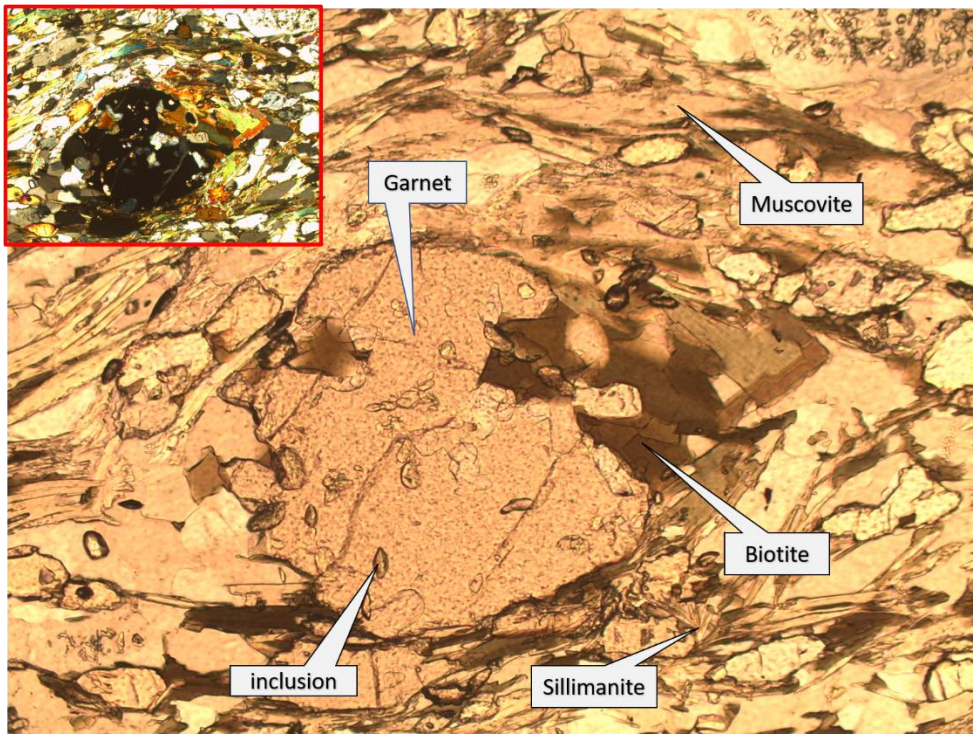

Figure 41. 10X magnification (thin-section no 6, table 1) displaying a Garnet with inclusions and in contact with Biotite. Sillimanite appears as small fibrous crystals in the lower part of the picture. Muscovite is found as flaky, elongated crystals contributing to the foliated appearance.

Tarfala Amphibolite (Seve-nappe, upper Middle Allochthon)

Thin-section 13 (fig. 42, table 1) displays the Tarfala Amphibolite with a feldspar-garnet rich band within. The latter is identified as a metapelite in microscopic view due to its mineral content of feldspar, quartz, micas and garnet. The amphibolite consists mostly of hornblende (approximately >90%) together with feldspar, micas and quartz. In the amphibolite seen in thin-section 12 (fig. 44, table 1), additional epidote is found appearing as crystals with third order interference colours in crossed polarized view. In thin-section 13, the structure appears foliated by aligned hornblende crystals that often has adopted a lenticular shape. Mica crystals appears in the amphibolite as bands running parallel with the foliation in the amphibolite. Plagioclase and quartz are often mixed alongside each other and sometimes occurs as bands in the amphibolite. The metapelite band displays a slightly foliated matrix consisting of plagioclase, quartz, biotite and muscovite. In the metapelite matrix porphyroblastic garnets with sizes up to approximately 2mm are surrounded by small amounts of titanite crystals. The metapelite band consist of approximately 30-40% garnets which are subhedral affected by deformation processes.

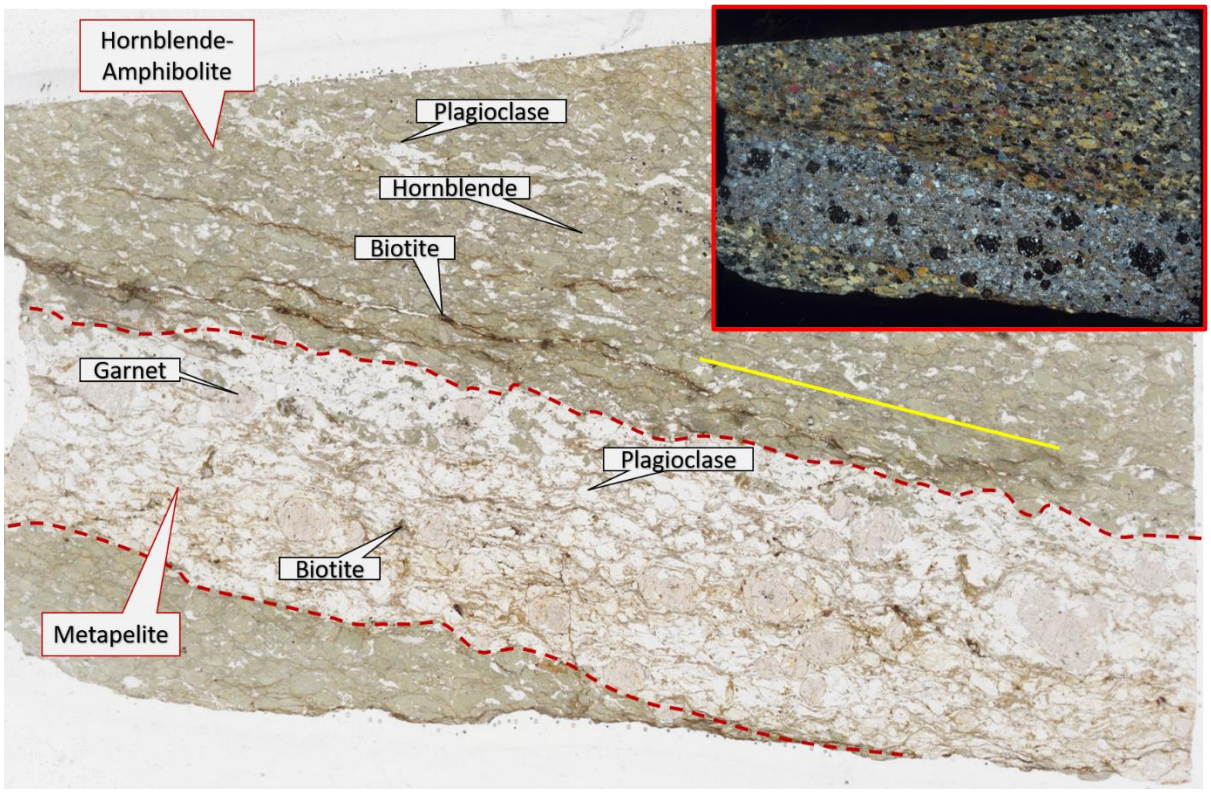

Figure 42. Scanning of thin-section 13 (table 1) in plane polarized light (inset picture displays the same view in crossed polarized light). Light band marked with a dashed line is a metapelite bounded by a Hornblende-Amphibolite on both sides. The Garnets are focused in the metapelite area. Yellow line displays foliation direction.

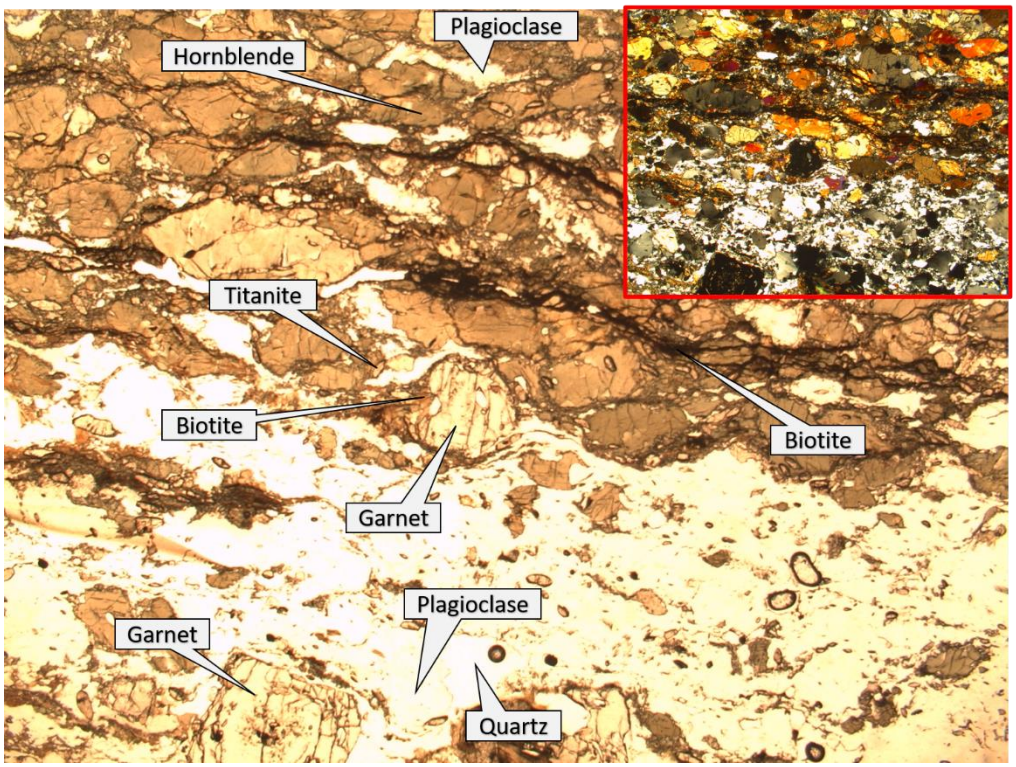

Figure 43. 2.5X magnification (thin-section 13, table 1) displaying the border between the Hornblende-Amphibolite (upper part of the picture) and the Metapelite band (lower part of the picture).

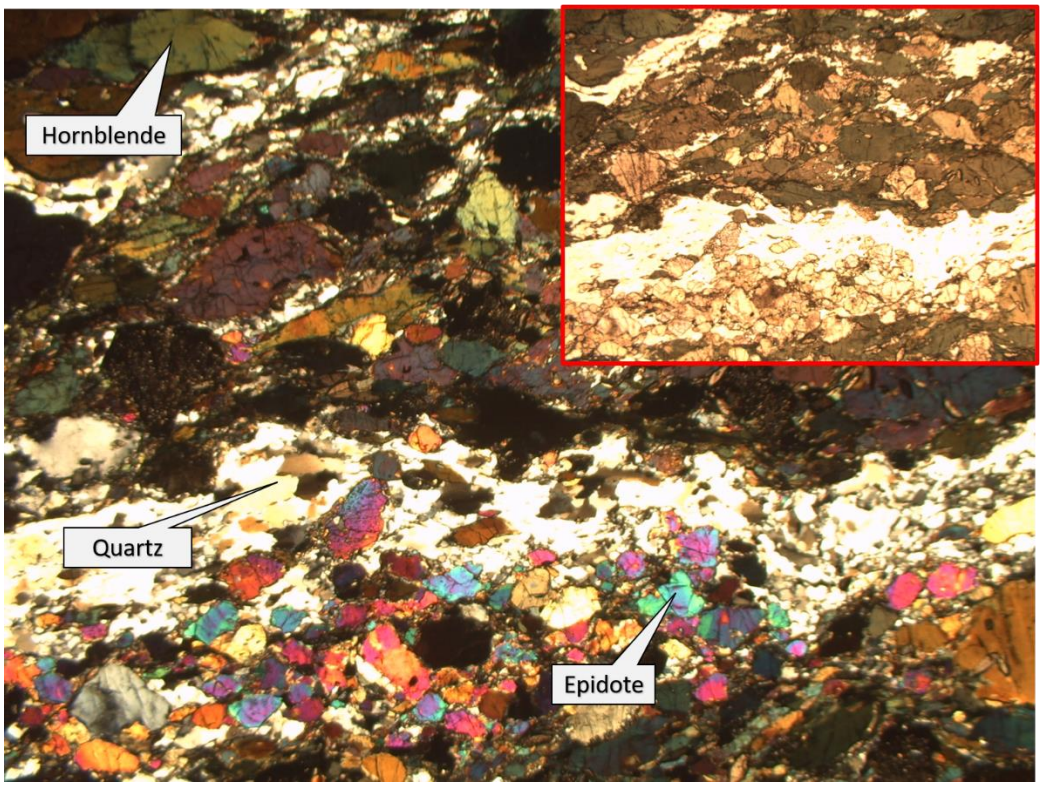

Figure 44. 2.5X magnification in crossed polarized light of thin-section 12 (table 1) containing Hornblende, Quartz and Epidote (inset picture displays the same view in plane polarized light).

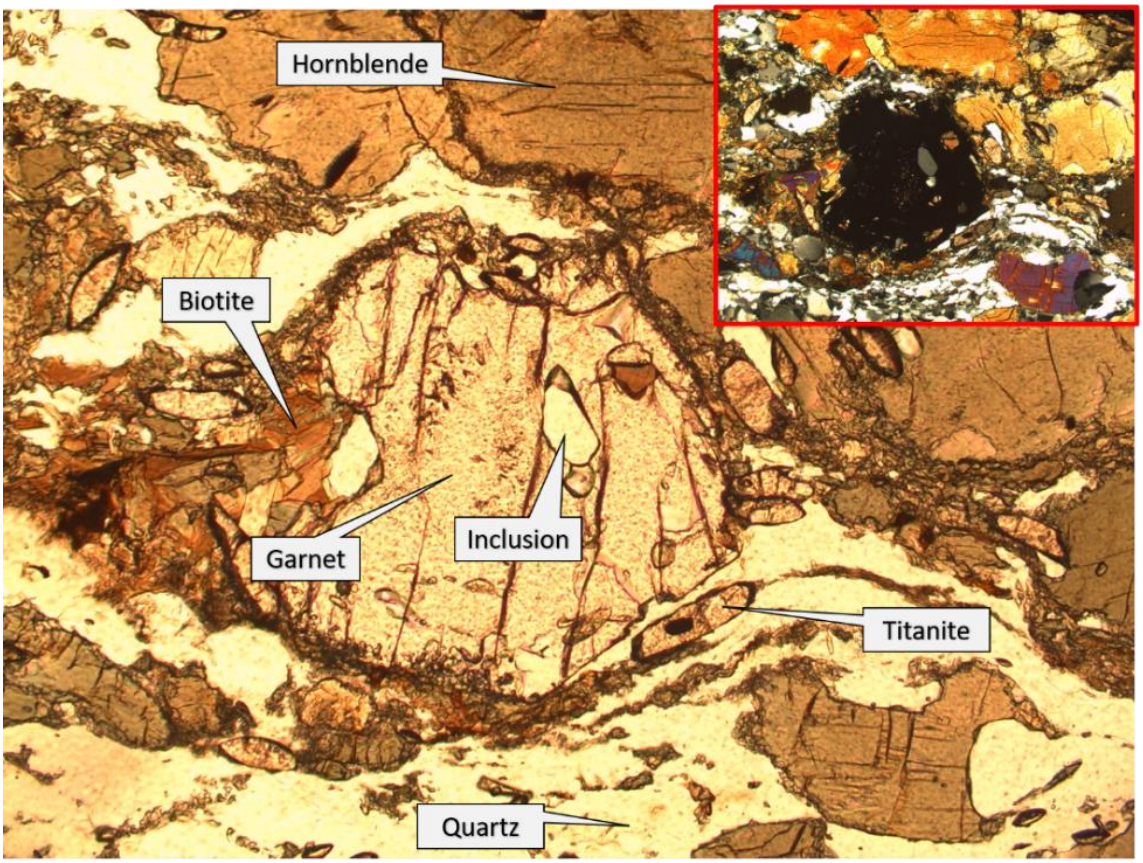

Figure 45. 10X magnification of thin-section 13 (table 1) viewed in plane polarized light (inset picture displays the same view in crossed polarized light).

Porphyroclastic mylonite (Seve-nappe, upper Middle Allochthon)

The matrix of thin- section 14 (fig. 46) shows a very foliated texture with a banded appearance. However, the matrix texture is interrupted by a large amount of deformed porphyroclasts. Ductile movement around the porphyroclasts are visible. Mineralogically, the matrix consists of micas. Darker bands are biotite while light bands are muscovite. Porphyroclastic minerals are mostly small feldspar crystals and garnets. However, some feldspar porphyroclasts are as large as a couple of centimetres. Most garnets display a large amount of deformation. Larger garnets are broken up and dragged along the foliation plane by brittle deformation. Ductile deformation of garnets is visible in some of the smaller garnets that displays a lenticular shape.

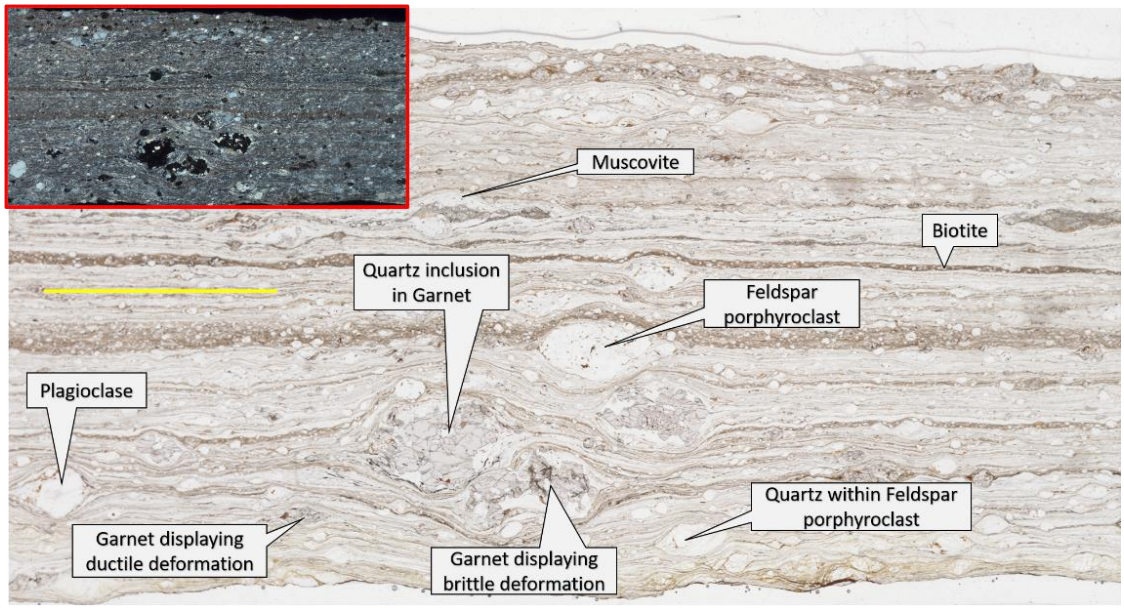

Figure 46. Scanning of thin section 14 (table1) in plane polarized light (inset picture displays the same view in crossed polarized light). Yellow line displays orientation of foliation. Most Garnets are very deformed and spread out in the direction of foliation however some signs of ductile deformation exist in smaller elongated crystals. Feldspar porphyroclasts displays recrystallization and are mixed with quartz. Mica bands of Biotite and Muscovite constitutes the very foliated matrix.

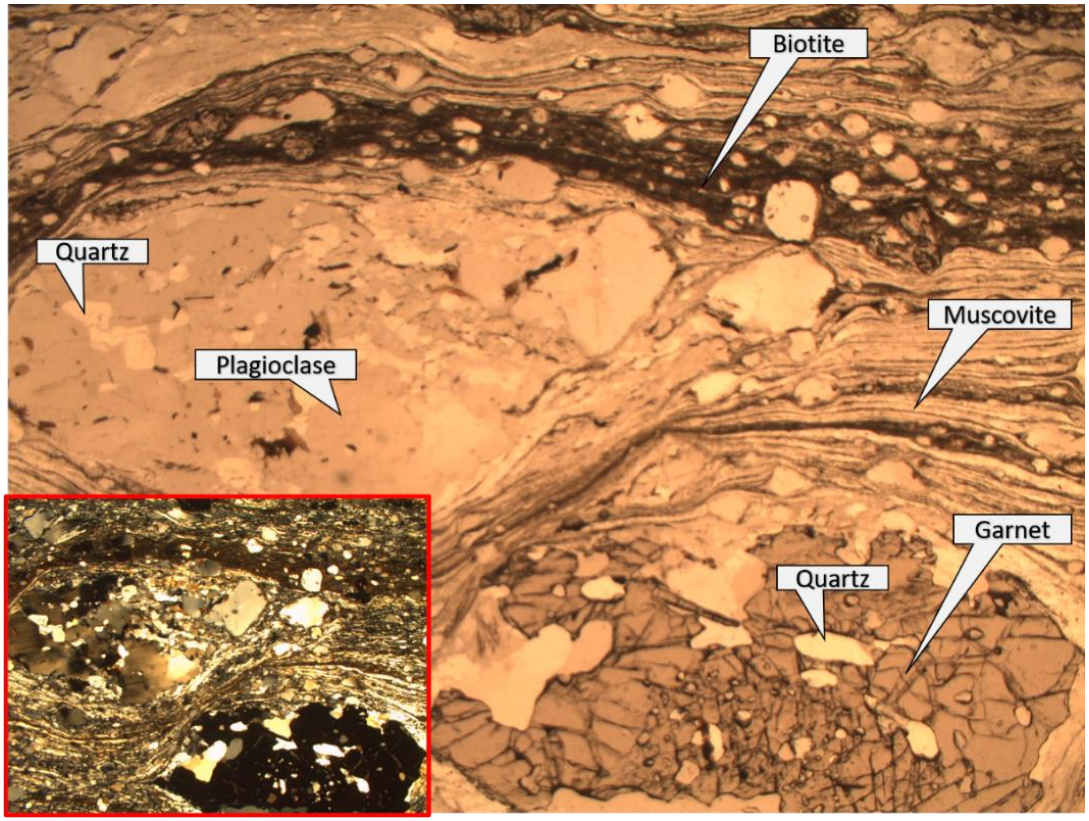

Figure 47. 10X magnification of thin-section 14 (table1) in plane polarized light (inset picture displays the same view in crossed polarized light). Inclusions of Quartz are found in both Garnet and Feldspar Porphyroclasts.

Gneiss (Seve-nappe, upper Middle Allochthon)

The texture of this bedrock unit in thin section 15 (fig. 48 & table 1) is displaying a slightly gneissose texture containing fine grained crystals and porphyroclasts of garnet (<2mm). However, a very sparse amount of feldspar porphyroclasts exists though not seen in the thin- section. The gneissose banding is somewhat enhanced by a slight foliation of the matrix running in the same direction. Mineral content consists of quartz, plagioclase, garnets, biotite and small amounts of muscovite. Mainly plagioclase and biotite make up the matrix with the biotite located in dark bands. Quartz crystals are scattered throughout the matrix and can also be found in some relict pressure shadows from the garnets and as inclusions within the same. The garnets are very deformed and biotite crystals are usually seen growing in widened cracks.

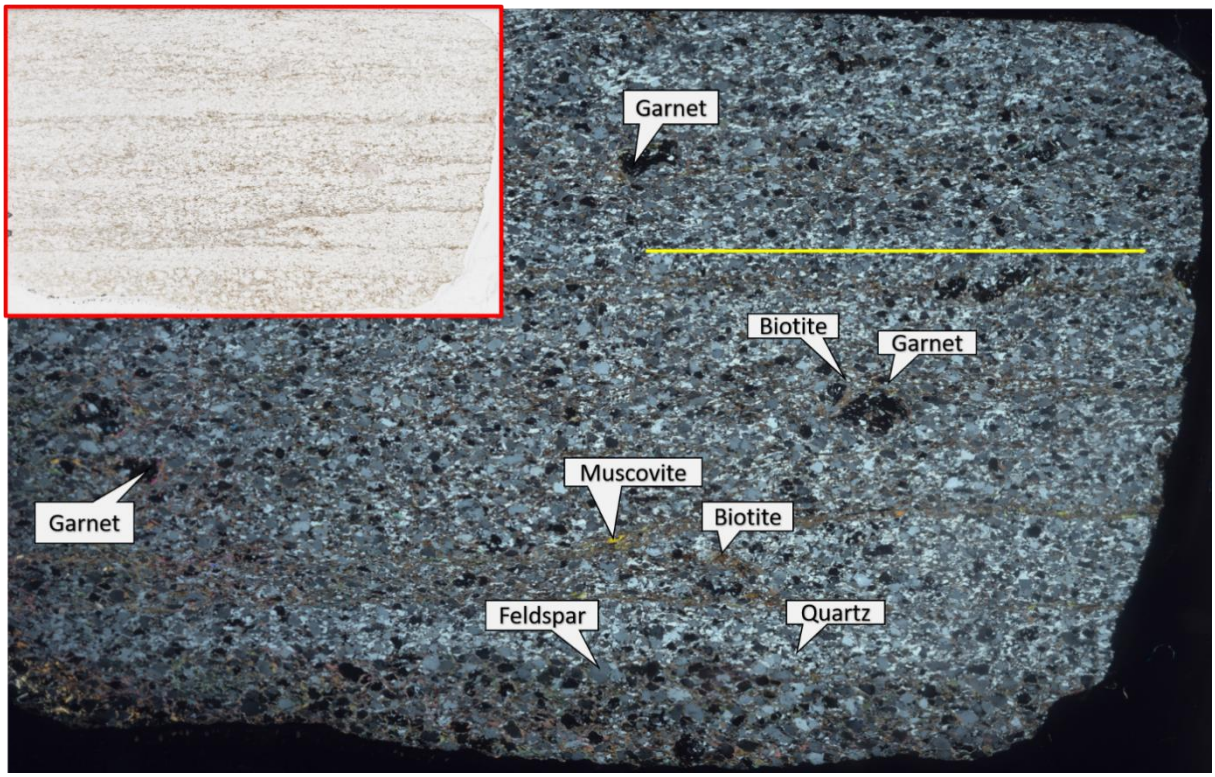

Figure 48. Scanning of thin section 15 (table 1) in crossed polarized light (inset picture displays the same view in plane polarized light). Yellow line displays the orientation of banding and foliation. Dark bands contain Biotite and a small amount of muscovite. Light bands contain Feldspar and Quartz. Porphyroclasts of Garnet are displaying brittle deformation with Biotite growing in some cracks.

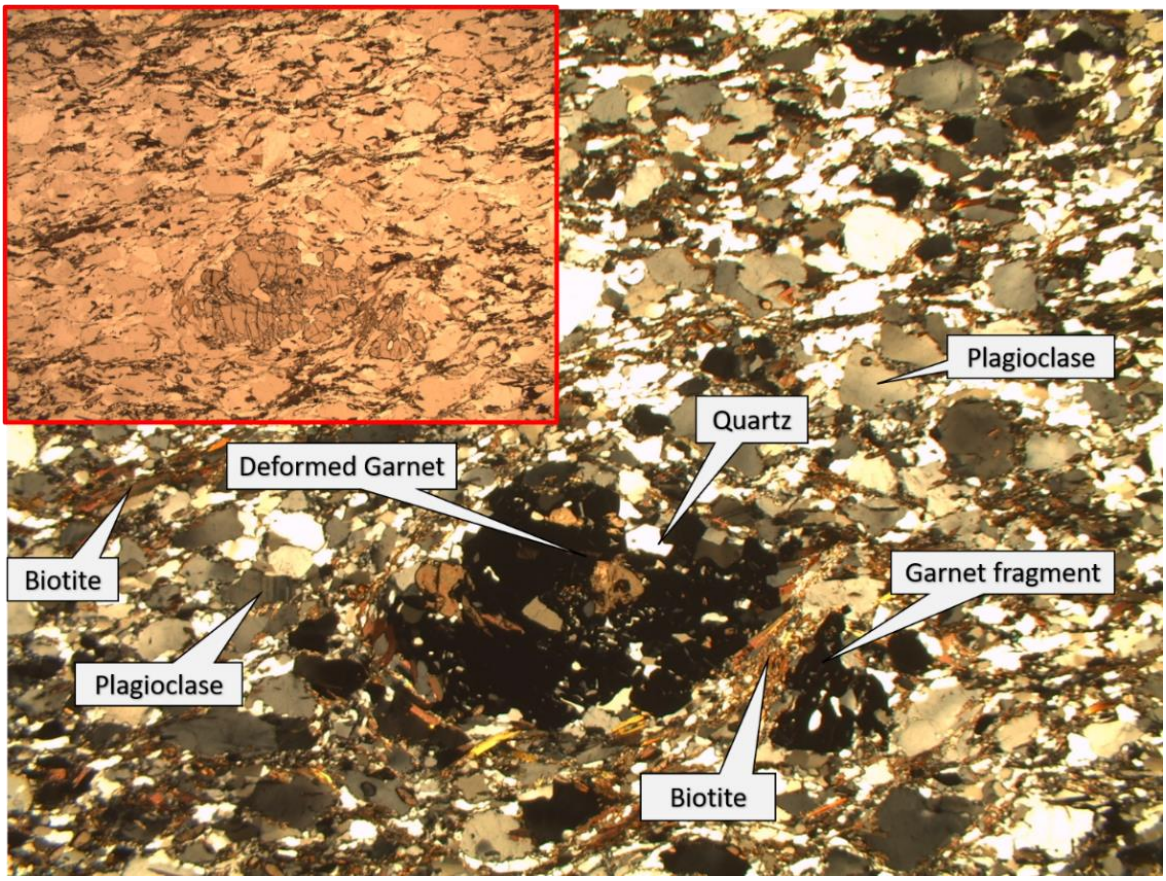

Figure 49. 2.5X magnification of thin- section 15 (table1) viewed in crossed polarized light (inset picture displays the same view in plane polarized light). The picture shows an anhedral Garnet which is very deformed along with formation of Biotite, seen in the cracks.

Kebne Amphibolite (Seve-nappe, upper Middle Allochthon)

Two thin-sections, number 18 and 20 (table 1) are described below as representatives for the Kebne Amphibolite unit. However, note that the actual hand-sample displayed signs of hydrothermal alteration and may perhaps not represent the whole bed-rock unit.

Thin-section 18 (fig. 50) exhibits two distinctly different areas with a somewhat diffuse border. The upper area displays an equigranular and slightly foliated texture. Mineralogically The upper area is dominated by hornblende crystals. Quartz crystals are sparse and scattered between the hornblende crystals. The lower area displays a non- foliated texture with an equigranular matrix surrounding porphyroclasts. Mineralogically the matrix is dominated by epidote, however some areas with quartz exists. The porphyroclasts are garnets and tend to be located in and in the vicinity of the lower area. The garnets are euhedral and some exhibits a poikiloblastic texture.

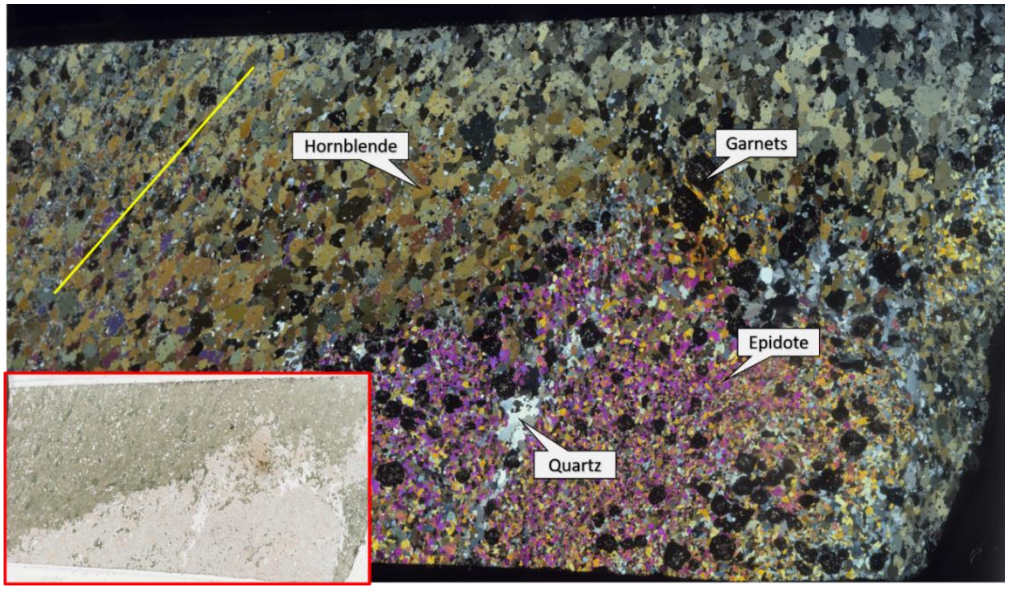

Figure 50. Scanning of thin- section 18 (table1) displayed in crossed polarized view (inset picture displays the same view in plane polarized light). Yellow line displays orientation of foliation.

Thin- section 20 (fig. 51 & table 1) displays the same types of areas as previously seen in thin section 18. However, additional minerals are found. The texture seen in thin section 20 is less foliated but otherwise the same as in thin- section 18. Mineralogically, thin-section 20 contains less hornblende and a greater area containing quartz. Embedded in the quartz area a single calcite crystal is found and identified by extreme birefringence and lamellar twinning. The upper right area contains epidote, garnets and actinolite.

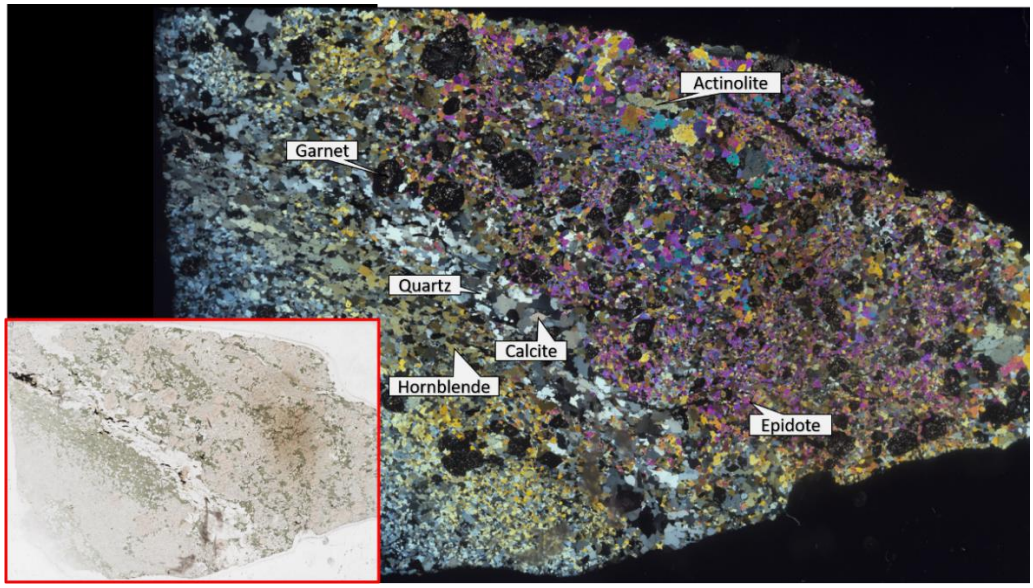

Figure 51. Scanning of thin- section 20 (table1) viewed in crossed polarised light (inset picture displays the same view in plane polarized light).

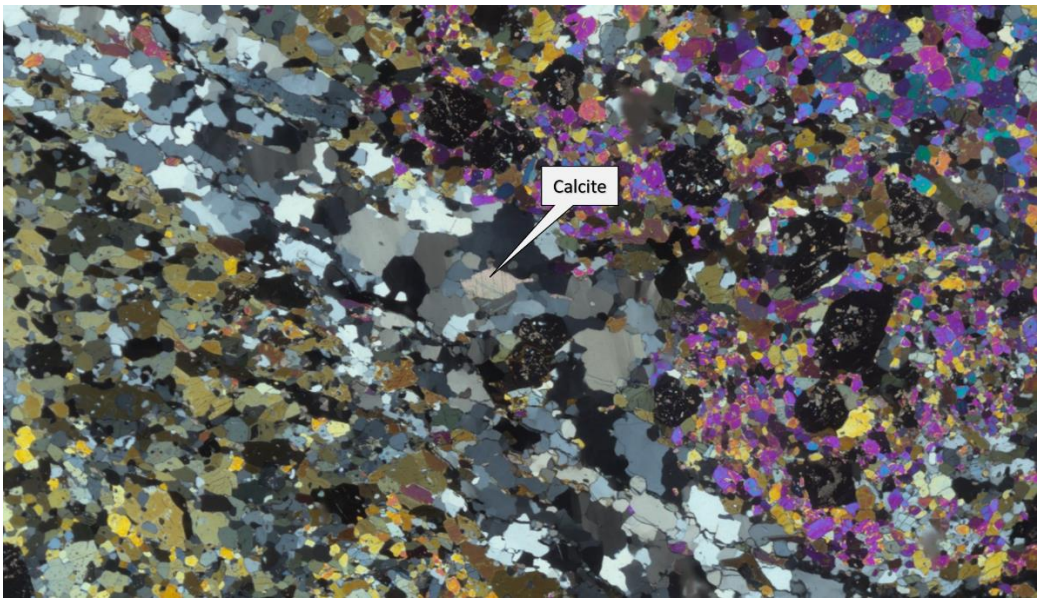

Figure 52. Enhancement of previous picture (fig. 51) displaying a single Calcite crystal surrounded by Quartz.

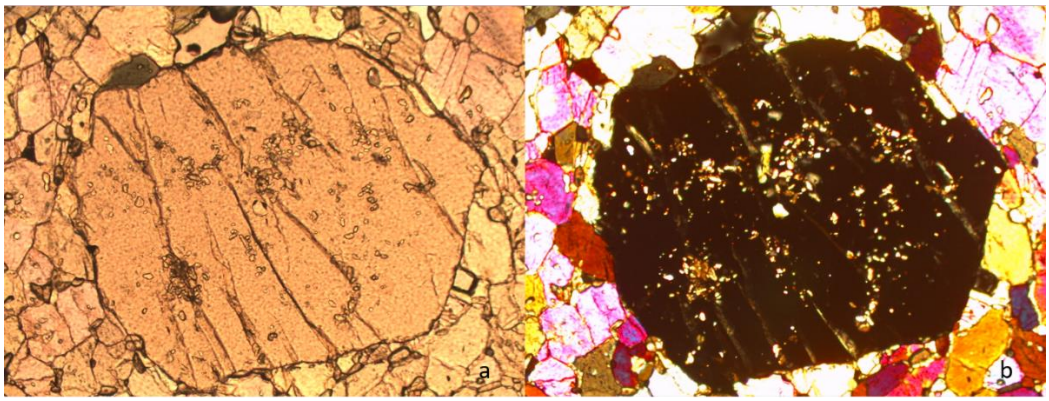

Figure 53. 10X magnification of thin-section 18 (fig.51 &table 18). (a) Euhedral garnet containing inclusions, surrounded by Epidote crystals viewed in plane polarized view (a) and crossed polarized view (b).

Kebne Dyke Complex (Seve-nappe, upper Middle Allochthon)

Thin section 25 (fig. 54, table1) displays a psuedomorphic texture without apparent foliation, however a slight foliation might be indicated (fig. 54). Uralitization texture and pyroxene to pyroxene alteration seen as corona structures is common. Mineralogy thin- section 25 contains plagioclase, orthopyroxene, clinopyroxene, amphibole, bronzite, inverted pigeonite, little Ilmenite and little biotite along with oxides. Bronzite occurs with coronas of inverted pigeonite which exhibits it's typical exsolution-lamellae. Orthopyroxene is surrounded by reaction rims of amphibole, mainly hornblende. The hornblende-rims resemble the hornblende in the previously described amphibolites by its colour and pleochroism. Between these alteration structures plagioclase exists and some plagioclase crystals have grown large and displays its characteristic polysynthetic twinning. Thin section 25 also contains a fair number of oxides which often displays rims of pyroxene.

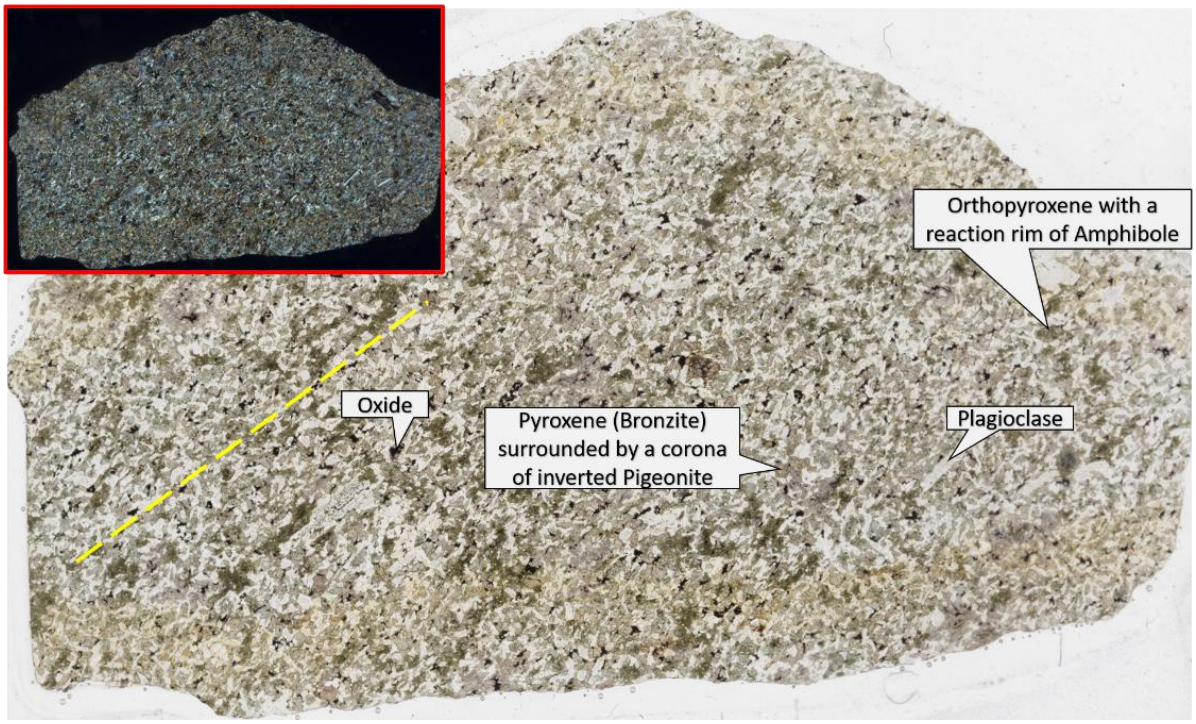

Figure 54. Scanning of thin- section 25 (table1) viewed in plane polarized light (inset picture displays the same view in crossed polarized view). Yellow dotted line displays a possible indication of foliation direction.

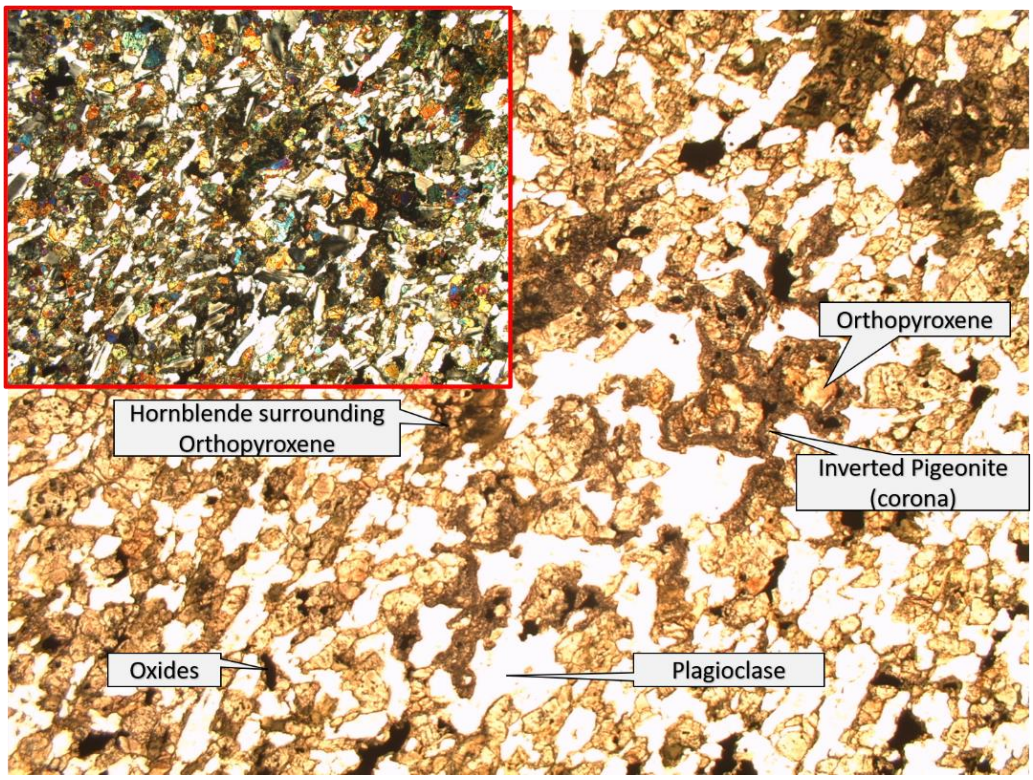

Figure 55. 2.5X Magnification of thin- section 25 (table1) viewed in plane polarized light (inset displays the same view in crossed polarized light).

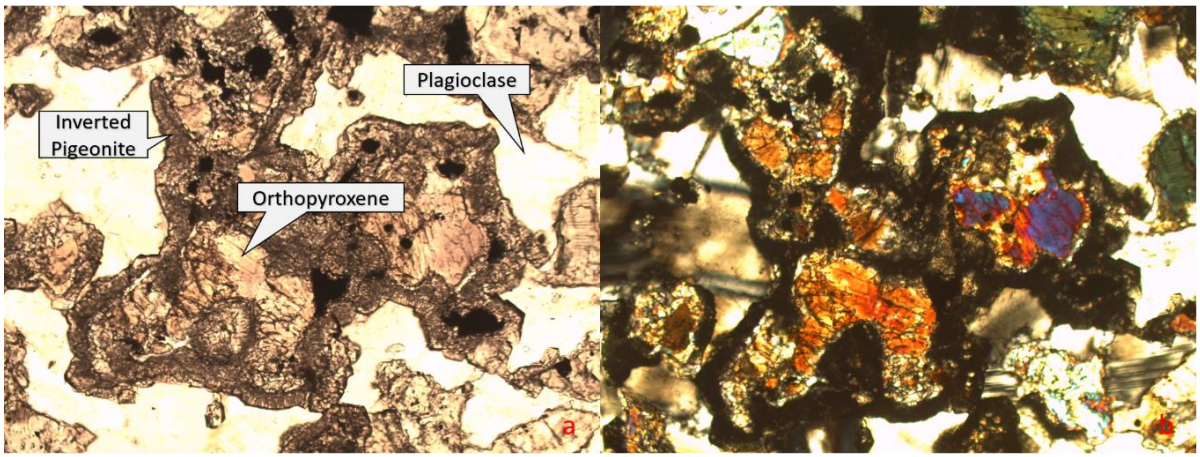

Figure 56. 10X magnification of thin- section 25 displaying an Inverted Pigeonite Corona structure surrounding Orthopyroxene. (a) Plane polarized view. (b) Crossed polarized view.

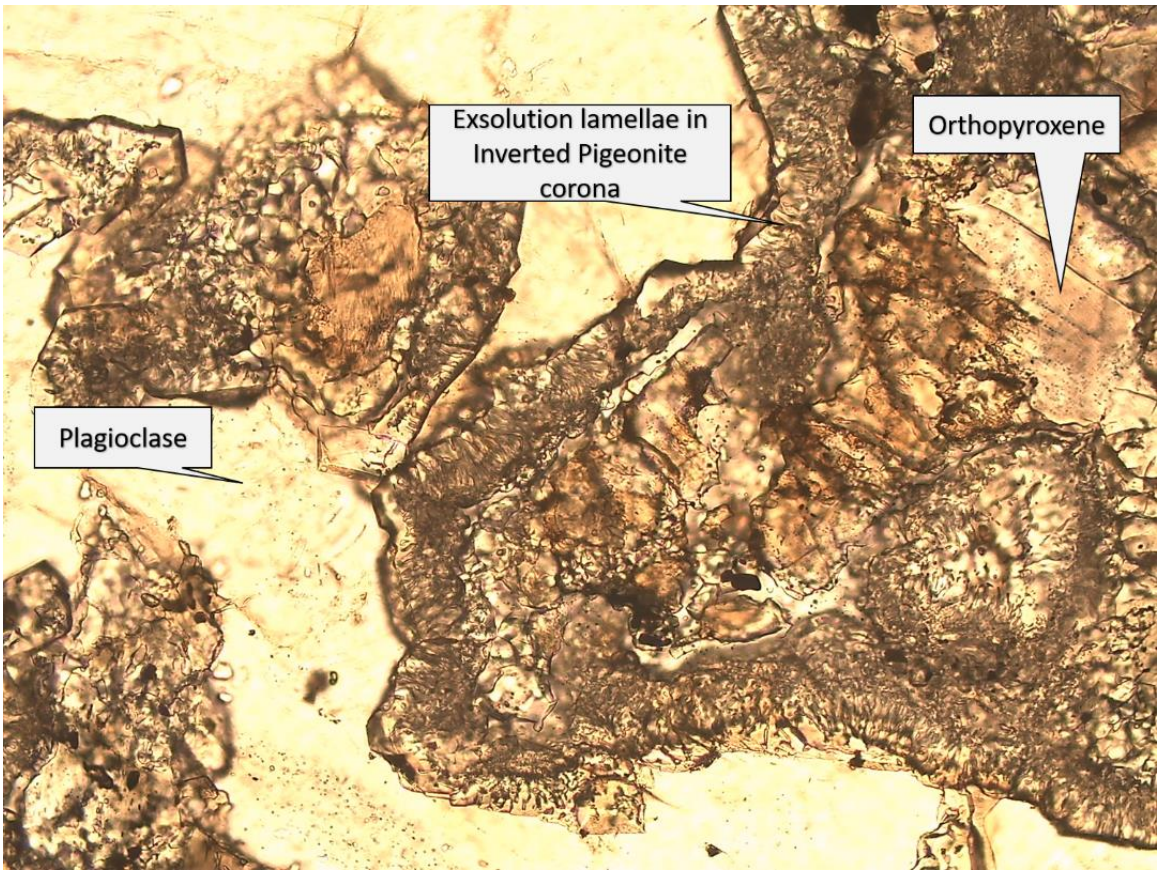

Figure 57. 20X Magnification of thin- section 25 viewed in plane polarized light. Exsolution-lamellae in Inverted Pigeonite corona is visible.

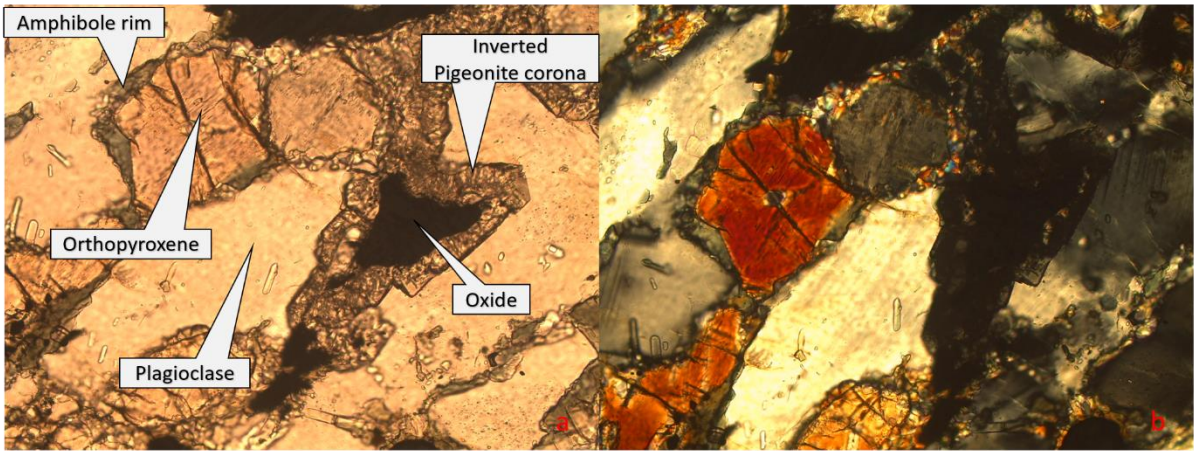

Figure 58. 20X Magnification of thin- section 25 displaying Orthopyroxene with a reaction rim of Amphibole and an oxide with a corona of inverted Pigeonite. (a) Plane polarized view. (b) Crossed polarized view.

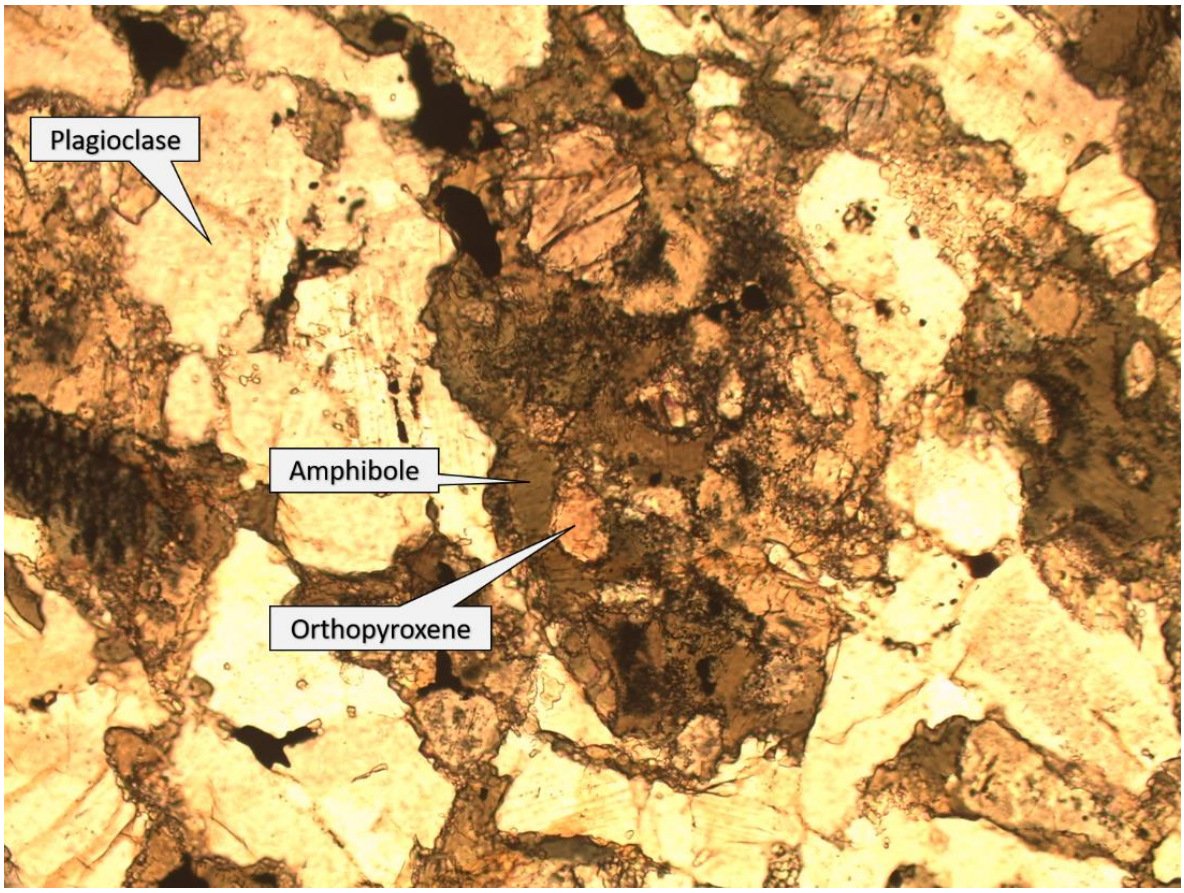

Figure 59. 20X Magnification of thin- section 25 viewed in plane polarized light. The picture displays alteration of Orthopyroxene to Amphibole (Hornblende).

3.4 SEM/EDS data

In this section data from thin section 13 (fig.42 & table1), obtained using the Scanning Electron Microscope (SEM) with fitted Energy-dispersive detector (EDS) at Luleå University of technology is presented. Representative compositional chemistry tables and backscattered electron images from each of the present minerals are presented along with comments (see appendix B for all obtained SEM/EDS data). The tables show contents of elemental oxides however the data was obtained as pure elemental content. Conversion to oxides was done by hand using the conversion factors displayed below (table 2). Additionally, some measurements were taken from thin section 25 (fig.54 & table 1) and the results therefrom are found in appendix D. Note that all analyse values are rounded off to two decimals.

Table 2. Oxide conversion factors

MgO	1.6582760749
Al2O3	1.8894636852
SiO2	2.1393352442
CaO	1.3991866267
MnO	1.2912264735
FeO	1.2864862929
TiO2	1.6680334029
Na2O	1.3479678135
K2O	1.2046048038
ZrO2	1.3507871081
HfO2	1.1792750294

Table 2. Table displays the oxide conversion factors which were used to convert elemental content to oxides by multiplication.

Garnet

The bulk material of the analysed grains consists of an almost homogenous chemical composition except for small elemental differences which can't be coupled with a zoning pattern. However, all garnets show signs of being affected by reactions along the rims, such as biotization. Inclusions of zircon (Table 13 & 14, Fig. 65) are common and displayed as white specks within the crystals.

Table 3. Garnet elemental compositional Chemistry table

Site	Oxygen	Magnesium	Aluminium	Silicon	Calcium	Manganese	Iron	total
1	37.17 (39.13)	1.25 (1.32)	11.21 (11.8)	15.28 (16.09)	7.94 (8.36)	1.62 (1.7)	20.51 (21.6)	94.98 (100)
2	37.68 (39.27)	1.25 (1.3)	11.19 (11.66)	15.25 (15.89)	7.95 (8.28)	1.07 (1.11)	21.57 (22.48)	95.96 (100)
4	37.52 (38.8)	1.36 (1.4)	11.62 (12.02)	15.97 (16.52)	8.16 (8.44)	1.73 (1.79)	20.35 (21.04)	96.71 (100)
9	39.14 (40.18)	1.13 (1.16)	11.38 (11.68)	15.44 (15.85)	8.29 (8.51)	0.76 (0.78)	21.27 (21.84)	97.41 (100)

Table 3. Compositional elemental data from Garnet achieved by SEM/EDS At Luleå University of technology. Normalized values are displayed within parentheses.

Table 4. Garnet elemental-oxide Chemistry table

Site	MgO	Al2O3	SiO2	CaO	MnO	FeO	total
1	2.19 (2.18)	22.30 (22.17)	34.42 (34.22)	11.70 (11.63)	2.20 (2.18)	27.79 (27.63)	100.6 (100)

2	2.16 (2.15)	22.03 (22.00)	33.99 (33.95)	11.59 (11.57)	1.43 (1.43)	28.92 (28.89)	100.12 (100)
4	2.32 (2.29)	22.71 (22.36)	35.34 (34.80)	11.81 (11.63)	2.31 (2.28)	27.07 (26.65)	101.56 (100)
9	1.92 (1.94)	22.07 (22.31)	33.91 (34.28)	11.91 (12.04)	1.01 (1.02)	28.10 (28.41)	98.92 (100)

Table 4. Garnet elemental-oxide composition calculated from elemental composition times the oxide conversion factors. Normalized values are displayed within parentheses.

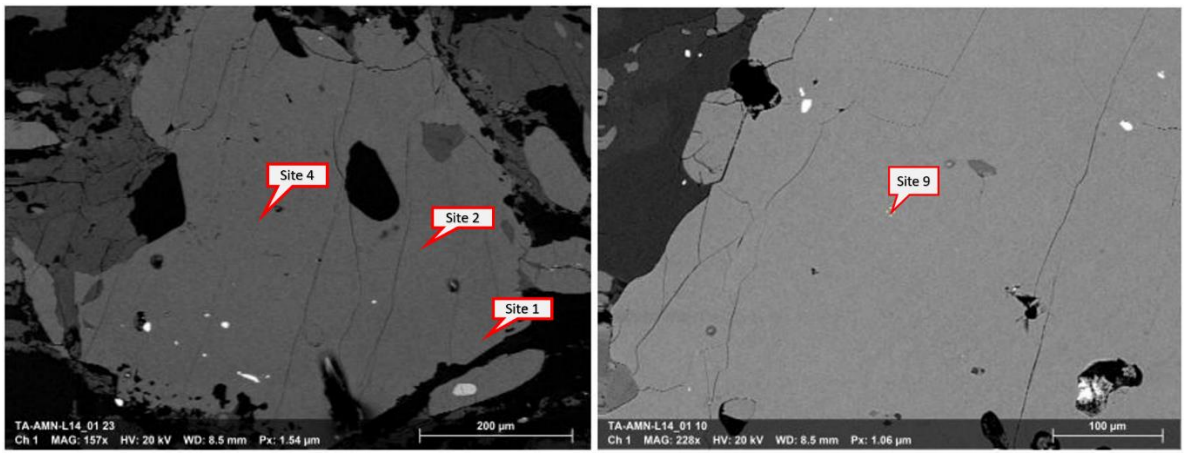

Figure 60. Backscattered electron image of two Garnets displaying site locations for SEM/EDS analyse. Alteration to Biotite is seen clearly to the left in the left picture, (also seen in fig. 45). The left picture displays a Garnet which is in contact with the Amphibolite while the right picture displays a Garnet embedded within the Metapelite band.

Hornblende

Two amphibole crystals were analysed with the Scanning electron microscope. One crystal was located in direct contact with the metapelite part of the thin-section while the second was located within the amphibolite part of the thin-section. The rim of the crystal in contact with the metapelite displays a more uneven edge with signs of alteration than the crystal within the amphibolite. Both of the hornblende crystals contain inclusions of titanite (based on one analyse of an inclusion within the crystal from the amphibolite, for analyse result see appendix B). Geochemical analyse of the two crystals doesn't show any large elemental variations although a slight increase of Mg and K along with a slight decrease of Ca occurs in the crystal in direct contact with the metapelite.

Table 5. Hornblende elemental compositional Chemistry table

Site*	Oxygen	Sodium	Magnesium	Aluminium	Silicon	Potassium	Calcium	Titanium	Iron	Sum
1	40.35 (41.84)	1.53 (1.58)	5.28 (5.48)	7.41 (7.68)	17.48 (18.12)	0.9 (0.94)	8.83 (9.15)	0.57 (0.6)	14.08 (14.6)	96.44 (100)
2	38.83 (41.42)	1.49 (1.59)	5.05 (5.39)	7.55 (8.05)	17.33 (18.49)	0.89 (0.95)	8.84 (9.43)	0.58 (0.62)	13.18 (14.06)	93.75 (100)
3	39.29 (41.58)	1.5 (1.59)	5.41 (5.73)	7.41 (7.84)	17.33 (18.34)	0.97 (1.03)	8.62 (9.12)	0.58 (0.62)	13.38 (14.16)	94.49 (100)
4	39.74 (41.59)	1.55 (1.62)	5.5 (5.75)	7.52 (7.87)	17.61 (18.44)	0.95 (1.00)	8.58 (8.98)	0.58 (0.61)	13.51 (14.14)	95.53 (100)

*Table 5. Compositional elemental data from Hornblende achieved by SEM/EDS At Luleå University of technology. Normalized values are displayed within parentheses. *Site 1 & 2 lies in direct contact with the Metapelite part of the thin-section, site 3 & 4 lies within the Amphibolite part of the thin- section.*

Table 6. Hornblende elemental-oxide Chemistry table

Site*	Na2O	MgO	Al2O3	SiO2	K2O	CaO	TiO	FeO	Sum
1	2.13 (2.17)	9.09 (9.25)	14.51 (14.78)	38.76 (39.47)	1.13 (1.15)	12.80 (13.03)	1.00 (1.02)	18.78 (19.12)	98.2 (100)

2	2.14 (2.16)	8.94 (9.00)	15.21 (15.32)	39.56 (39.83)	1.14 (1.15)	13.19 (13.29)	1.03 (1.04)	18.09 (18.21)	99.3 (100)
3	2.14 (2.17)	9.50 (9.60)	14.81 (14.97)	39.24 (39.65)	1.24 (1.25)	12.76 (12.90)	1.03 (1.05)	18.22 (18.41)	98.94 (100)
4	2.18 (2.21)	9.54 (9.63)	14.87 (15.02)	39.45 (39.84)	1.20 (1.22)	12.56 (12.69)	1.02 (1.03)	18.19 (18.37)	99.01 (100)

*Tabell 6. Hornblende elemental-oxide composition calculated from elemental composition times the oxide conversion factors. Normalized values are displayed within parentheses. *Site 1 & 2 lies in direct contact with the Metapelite part of the thin- section, site 3 & 4 lies within the Amphibolite part of the thin- section.*

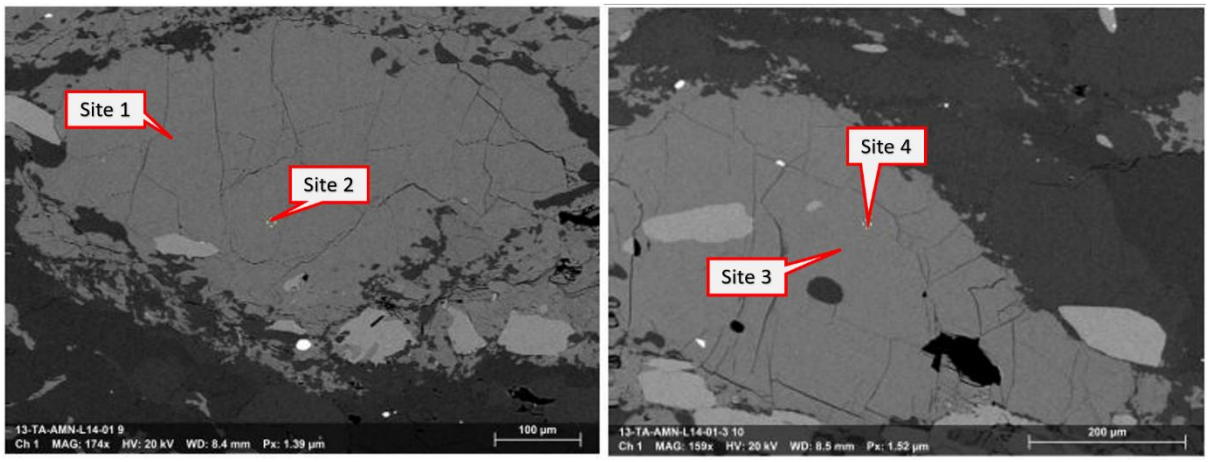

Figure 61. Backscattered electron images of two Hornblende crystals displaying site locations for SEM/EDS analyse. Left crystal (containing site 1 & 2) lies in direct contact with the Metapelite part of the thin- section. Right crystal (containing site 3 & 4) lies within the Amphibolite part of the thin- section.

Biotite

One biotite crystal was analysed and chosen due to its somewhat larger size than other biotite crystals. The crystal was located intergrown and surrounded by plagioclase, garnet and quartz.

Table 7. Biotite elemental compositional chemistry table

Site	Oxygen	Magnesium	Aluminium	Silicon	Potassium	Titanium	Iron	Sum
1	38.10 (42.05)	6.09 (6.72)	8.33 (9.19)	14.43 (15.92)	6.92 (7.64)	1.80 (1.98)	14.95 (16.49)	90.62 (100)
2	36.83 (40.69)	6.23 (6.88)	8.55 (9.44)	14.97 (16.53)	7.19 (7.94)	1.80 (1.99)	14.96 (16.52)	90.46 (100)
3	37.02 (40.98)	6.10 (6.75)	8.47 (9.38)	14.78 (16.35)	7.22 (7.99)	1.93 (2.14)	14.83 (16.41)	90.35 (100)
4	37.14 (41.17)	6.31 (7.00)	8.2 (9.09)	14.64 (16.23)	6.9 (7.65)	1.69 (1.87)	15.33 (17.00)	90.21 (100)

Table 7. Compositional elemental data from Biotite achieved by SEM/EDS At Luleå University of technology. Normalized values are displayed within parentheses.

Table 8. Biotite elemental-oxide Chemistry table

Site	MgO	Al2O3	SiO2	K2O	TiO	FeO	Sum
1*	11.14 (11.57)	17.36 (18.03)	34.06 (35.37)	9.20 (9.56)	3.30 (3.43)	21.21 (22.03)	96.27 (100)
2	11.41 (11.55)	17.84 (18.06)	35.36 (35.81)	9.56 (9.69)	3.32 (3.36)	21.25 (21.52)	98.74 (100)
3	11.19 (11.40)	17.72 (18.05)	34.98 (35.62)	9.62 (9.80)	3.57 (3.64)	21.11 (21.50)	98.19 (100)
4	11.61 (11.88)	17.18 (17.58)	34.72 (35.54)	9.22 (9.43)	3.12 (3.19)	21.87 (22.38)	97.72 (100)

*Table 8. Biotite elemental-oxide composition calculated from elemental composition times the oxide conversion factors. Normalized values are displayed within parentheses. *Analyse-time shorter.*

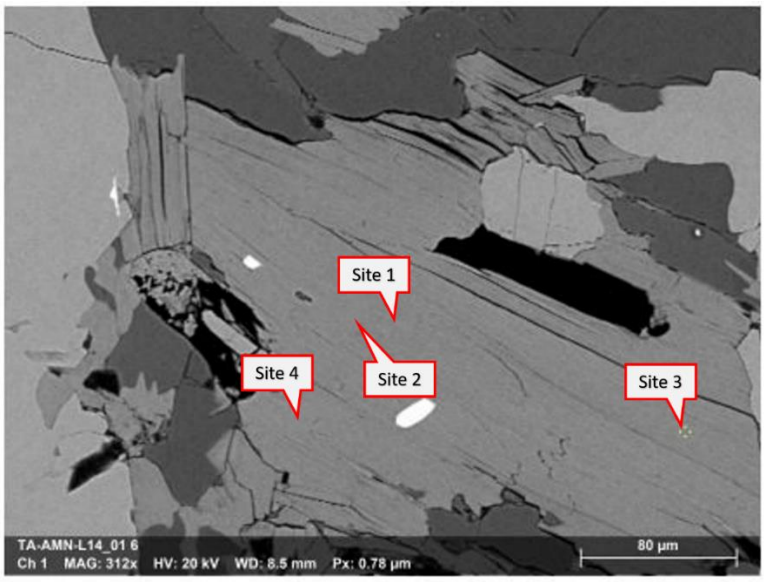

Figure 62. Backscattered electron images of Biotite displaying site locations for SEM/EDS analyse.

Plagioclase

Two plagioclase crystals were analysed, one from each part of the thin-section. In the metapelite part, the plagioclase crystals are intergrown to a great extent with quartz which show almost similar grades of brightness in a backscattered electron image. No apparent variation of chemical content between was detected between the two crystals.

Table 9. Plagioclase elemental compositional chemistry table

Site*	Oxygen	Sodium	Aluminium	Silicon	Calcium	Sum
1	42.14 (47.46)	5.98 (6.73)	11.81 (13.31)	25.7 (28.95)	3.16 (3.56)	88.79 (100)
2	40.83 (47.29)	5.62 (6.51)	11.65 (13.49)	24.81 (28.73)	3.44 (3.98)	86.35 (100)
3	40.66 (47.6)	5.82 (6.81)	11.18 (13.09)	24.83 (29.07)	2.93 (3.43)	85.42 (100)
4	39.68 (47.69)	5.47 (6.57)	10.93 (13.13)	24.04 (28.89)	3.1 (3.72)	83.22 (100)

*Table 9. Compositional elemental data from Plagioclase achieved by SEM/EDS At Luleå University of technology. Normalized values are displayed within parentheses. * *Site 1 & 2; Analyse made within Metapelite part of thin-section, site 3 & 4; Analyse made of Plagioclase within &Amphibolite part of thin- section.*

Table 10. Plagioclase elemental-oxide Chemistry table

Site*	Na2O	Al2O3	SiO2	CaO	Sum
1	9.07 (8.97)	25.15 (24.87)	61.93 (61.24)	4.98 (4.93)	101.13 (100)
2	8.78 (8.66)	25.49 (25.16)	61.46 (60.68)	5.57 (5.50)	101.3 (100)
3	9.18 (9.10)	24.73 (24.51)	62.19 (61.63)	4.80 (4.76)	100.9 (100)
4	8.86 (8.80)	24.81 (24.64)	61.81 (61.39)	5.20 (5.17)	100.68 (100)

*Table 10. Plagioclase elemental-oxide composition calculated from elemental composition times the oxide conversion factors. Normalized values are displayed within parentheses. *Site 1 & 2; Analyse made within Metapelite part of thin-section, site 3 & 4; Analyse made of Plagioclase within &Amphibolite part of thin- section.*

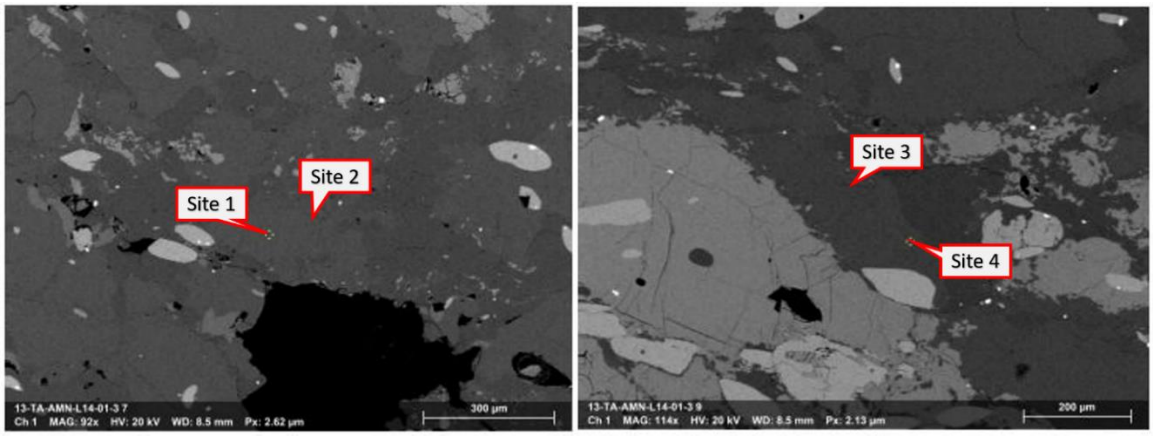

Figure 63. Backscattered electron images of two Plagioclase crystals displaying site locations for SEM/EDS analyse. Site 1 & 2, left picture is located in Metapelite part of the thin- section. Site 3 & 4, right picture is located in Amphibolite part of the thin- section.

Titanite

Titanite appear as elongated oval shaped crystals, both solitary and as embedded in hornblende crystals. Two titanite crystals which were analysed are presented here, for data referring to titanite appearing as inclusions, see appendix B. No great geochemical differences were detected between the two crystals however the amount of Ti is measured to be slightly higher on site 4 (table 11 &12). Bright inclusion within the titanite crystal (fig. 64) contains oxides of Fe and Ti (appendix B, table 15 & 16). Note that site 1 and 2 (table 11 &12, fig. 64) are measured with a shorter analyse time and might not be quantifiable.

Table 11. Titanite elemental compositional chemistry table

Site	Oxygen	Aluminium	Silicon	Calcium	Titanium	Sum
1*	40.74 (41.33)	1.02 (1.03)	12.46 (12.64)	21.94 (22.26)	22.4 (22.73)	98.56 (100)
2*	37.71 (39.98)	1.15 (1.22)	13.25 (14.05)	20.18 (21.4)	22.02 (23.35)	94.31 (100)
3	40.62 (41.95)	0.88 (0.9)	12.47 (12.88)	19.6 (20.24)	23.25 (24.02)	96.82 (100)
4	39.61 (40.7)	0.9 (0.92)	12.51 (12.85)	20.3 (20.86)	24.02 (24.67)	97.34 (100)

*Table 11. Compositional elemental data from Titanite, achieved by SEM/EDS At Luleå University of technology. Normalized values are displayed within parentheses. *Analyse time shorter.*

Table 12. Titanite elemental-oxide Chemistry table

Site	Al2O3	SiO2	CaO	TiO	Sum
1*	1.95 (1.98)	27.04 (27.58)	31.15 (31.77)	37.91 (38.67)	98.05 (100)
2*	2.31 (2.28)	30.06 (29.69)	29.94 (29.57)	38.95 (38.47)	101.26 (100)
3	1.70 (1.74)	27.55 (28.22)	28.32 (29.00)	40.07 (41.03)	97.64 (100)
4	1.74 (1.75)	27.49 (27.61)	29.19 (29.31)	41.15 (41.33)	99.57 (100)

*Table 12. Titanite elemental-oxide composition calculated from elemental composition times the oxide conversion factors. Normalized values are displayed within parentheses. * Analyse time shorter.*

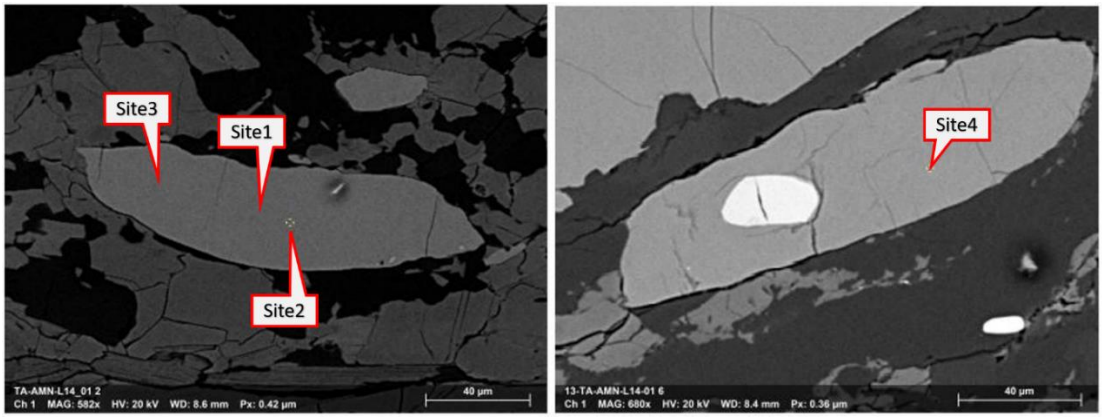

Figure 64. Backscattered electron images of two Titanite crystals displaying site locations for SEM/EDS analyse. Site 1, 2 & 3, left picture. Site 4, right picture.

Zircon (inclusion in Garnet)

Zircon crystals appear as inclusions within garnets displaying a light, with colour in. The analysed crystal show substitution with hafnium replacing zirconium to a small extent.

Table 13. Zircon (inclusion in Garnet) elemental compositional chemistry table

Site	Oxygen	Silicon	Iron	Zirconium	Hafnium	Sum
1	29.40 (31.75)	14.03 (15.15)	1.00 (1.08)	47.26 (51.03)	0.92 (0.99)	92.61 (100)

Table 13. Compositional elemental data from Zircon inclusion within a Garnet, achieved by SEM/EDS At Luleå University of technology. Normalized values are displayed within parentheses.

Table 14. Zircon (inclusion in Garnet) elemental-oxide Chemistry table

Site	SiO2	FeO	ZrO2	HfO2	Sum
1	32.41 (32.83)	1.39 (1.41)	63.84 (64.66)	1.08 (1.10)	98.72 (100)

Table 14. Zircon elemental-oxide composition calculated from elemental composition times the oxide conversion factors. Normalized values are displayed within parentheses

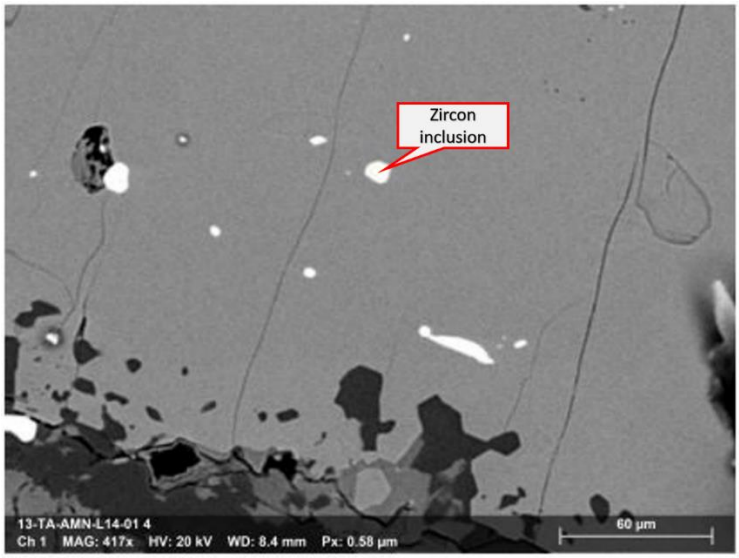

Figure 65. Analyse-site for Zircon inclusion within Garnet.

3.5 Pressure and temperature estimates

Three sets of pressure-temperature estimates for thin section 13 (fig. 42, table 1) are presented in this section. One set represents the metapelite-layer, one represents the amphibolite and one set represents the both the metapelite layer and amphibolite area together. For the metapelite, the SEM/EDS data selected to run in AX_2 are values for garnet, biotite, feldspar and titanite. SEM/EDS data selected for the amphibolite part of the thin section are values for garnet, biotite, feldspar, hornblende and titanite. Note that all input values were normalized before being inserted to AX_2. Their exchange reactions together with other end-members present in the sample was then processed in THERMOCALC 3.33. The three pressure- temperature sets which were below a best fit value were then selected from the resulting output data. A best fit value (sigfit) below 1.73 and 1.54 respectively in this case gives a confidence of 95% for the result. This parameter assesses how well the data interacts and is depending on the activity uncertainties. It is effectively a measure on how much the end-member activity has to be varied for the reaction line to run through a single pressure-temperature point. All diagnostic data with a higher best fit value can be found in appendix C.

Metapelite layer
T = 600±34 C (1 s.d)
P = 1.11±0.13 GPa (1 s.d)
sigfit = 1.34 compared with a threshold value of 1.73 for 95% confidence

Amphibolite area
T = 613±42 C (1s.d)
P = 1.18±0.16 GPa (1 s.d)
sigfit = 1.65 compared with a threshold value of 1.73 for 95% confidence

Metapelite layer and Amphibolite area combined
T = 606±27 C (1 s.d)
P = 1.13±0.1 GPa (1 s.d)
sigfit = 1.08 compared with a threshold value of 1.54 for 95% confidence

3.6 Sources of error

In this study there are a number of uncertainties to be taken into account. The data collected from the electron microscope (SEM/EDS) should be considered as a possible uncertainty source mainly due to the fact that some variation in accuracy exists between element measurements. Electron probe micro analyses (EMPA) would have been a better option but were beyond the budget of this candidate thesis. Errors in Geothermobarometry might also result from geochemical composition variation between sites in a mineral. If a mineral is heterogenous, variation of calculated pressure and temperature will be the result between sites. Any resulting errors from the electron microscope analysis will propagate to affect the result from THERMOCALC along with effects from possible errors in the datasets used by THERMOCALC, thus the usage of normalized values in this study may have a small impact of the result. The use of standard deviation values by both THERMOCALC and AX_2 should also be considered as an uncertainty in this study.

4. Discussion

As can be observed on the map in this study, the Tarfala Valley constitutes an area that is well suited for studies on the Caledonian nappe succession. The orientation and location of the valley within the well eroded Scandinavian Caledonides combined with the sub-horizontal orientation of the nappe sequence emphasizes the stratigraphic relationship between the nappes. In the following discussion I comment on the tectono-stratigraphy and discuss the metamorphic conditions. Finally, the Kebne Dyke Complex is discussed and compared with the amphibolites in the valley.

Tectono-stratigraphy

The Tarfala Valley mostly consists of bedrock-units from the Seve Nappe Complex, underlain by bedrock-units which are often thought to derive from the upper part of the Middle Allochthon. By looking at the lower mapped bedrock-units a sequence consisting of mylonite -gneiss -amphibolite was found. At the present and according to the common notion the mylonite and gneiss belongs to the Middle Allochthon and the amphibolite belong to the Seve nappe. However, a somewhat different interpretation could also be considered. The aforementioned sequence can be seen repeated further up the valley, involving the northern most gneiss and the Kebne Amphibolite of the Seve nappe. This repetition could imply repetition of the same thrust sheet which in turn would imply that the mylonite and gneiss of the Middle Allochthon instead would be assigned to the Seve nappe. In turn this would mean that the Middle Allochthon was absent in this area. The clear similarities of the two amphibolites could further support this interpretation although further investigation e.g. pressure-temperature studies and isoptopic analyzes would be necessary to confirm this conclusion. On the contrary, the two gneiss units are visually different which might contradict the thrust duplication interpretation. A larger area mapped along with more pressure-temperature investigations from each bedrock unit could provide a better basis for choosing between these hypotheses.

Metamorphism

The best pressure-temperature estimate for the Tarfala Amphibolite (sample 8) is 1.13±0.1 GPa and 606±27 C. This corresponds to the high-pressure end of the Amphibolite facies (fig.4 &66). The temperature and pressure estimate plots on the “typical” continental geotherm which is of higher pressure than the more expected typical gradient for a collisional mountain belt (fig. 66). However, pressure-temperature estimates from different parts of this sample yield different temperatures for metapelite and amphibolite portions of the same sample. This might imply disequilibrium. On the other hand, poor sigfit values for these estimates might imply that phases are missing, and that the aforementioned estimate which was made for the entire sample is more representative.

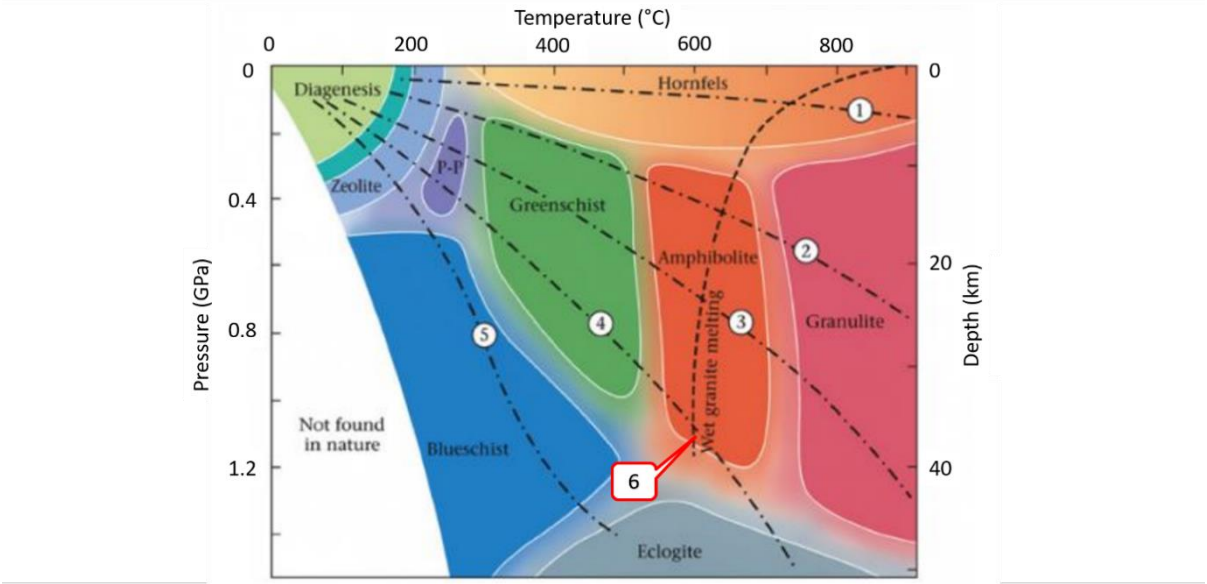

Figure 66. Pressure-temperature metamorphic facies diagram with approximate boundaries and typical gradients for different typical conditions of metamorphism. 1) Contact (thermal) metamorphism. 2) Volcanic arc. 3) Collisional mountain-belt. 4) stable continent. 5) Accretionary prism, subduction zone. 6) Pressure and temperature estimate of the combined Metapelite layer and Amphibolite area (sample 8). Modified from Marshak (2001).

The high-pressure end of the amphibolite facies is close to the Eclogite facies conditions which have been recorded at other locations within the Seve Nappe Complex. By looking at the recorded pressure estimates of corresponding bedrock units from Jämtland (4.1-4.2 GPa), Vaimok lens (2.8-3.1 GPa), Tsäkkok lens (2.2GPa) and up to the Kebnekaise area in Norrbotten a trend with decreasing pressure towards the north is indicated. Although the rock examined in this study don't display the same ultra high pressure metamorphic facies as the eclogites from Jämtland, the high pressure Amphibolite facies might still be related to the previously mentioned subduction event. The somewhat lower pressure estimate of 1.13±0.1 GPa from the Tarfala Amphibolite might be a result from overprint by the later orogenic events similar to the previously mentioned overprint pressure estimates of the Jämtland location (1.0-1.1 GPa). However, more studies regarding the amphibolites within the Seve Nappe Complex are needed to constrain the pressure and temperature regime leading to a better understanding of the Seve Nappe Complex evolution.

A better understanding of the individual mineral grains might also improve the knowledge about the evolution of the Seve Nappe Complex. To illustrate this, the garnets and zircons in this study can serve as examples. The garnets in the examined sample do not display any apparent visual or chemical zoning. Most garnets posess zoning and the lack thereof should be due to a short growth duration along with a greatly fractioned bulk-rock composition. Also, metamorphism that greatly exceeds 600°C along with fast exhumation could lead to the small and last garnets to nucleate being without zoning. Some zoning might also be lost due to diffusion within the crystal (Etzel & Catlos, 2021). The lack of zoning in the garnets of the Tarfala Amphibolite might thus possibly be related to fast exhumation after the previously proposed subduction event. Moreover, zircons found within the amphibolite can be used for U-Pb dating as seen in previous work on other locations, eg. dating of the Kebne Dyke Complex (baird & Chamberlain, 2014). Zircons within the amphibolites in the Tarfala Valley could proove useful for a time- correlation with other bedrock units within the Caledonides if studied further.

Kebne Dyke Complex

Setting the Kebne Dyke Complex apart from the other present bedrock units within the Tarfala Valley is it's more igneous appearance. However, the findings of some slightly foliated areas first raised the question; was the Kebne Dyke Complex metamorphosed? The xenoliths together with the non-foliated texture indicate an igneous nature of the bedrock unit in hand sample. Also, the presence of Ilmenite as seen in petrological examinations (confirmed in the additional SEM analyse, appendix D) could further support the theory of an igneous nature due to its habit of breaking down to titanite or rutile during metamorphism (Angiboust & Harlow 2017).

However, in the petrological investigation some metamorphic alteration is visible. A uralitization process can be suspected from the petrographic investigation due to orthopyroxene crystals surrounded by reaction rims of hornblende. This together with the findings of a vague foliation supports the theory of The Kebne Dyke Complex being metamorphosed. It may be that the Kebne Dyke Complex is a slightly altered gabbro and the amphibolites are the far more altered equivalent. This theory is based on the similarities between the hornblende crystals along with titanite and rutile being present in the amphibolites.

Thus, it might not be different metamorphic conditions that are responsible for the difference between the Kebne Dyke Complex and the amphibolites. If considering the possibility that the two units have experienced the same metamorphic conditions, something else must be the cause for their differences. This cause could possibly be due to the units originating from two different types of protoliths with different permeabilities. It is possible that the Kebne Dyke Complex derives from a gabbroic protolith and the amphibolites derives from a basaltic protolith. Gabbro usually is less permeable than basalt and therefor may survive metamorphism better with only a partial overprint. The similarity between the hornblende in the amphibolites and the hornblende rims surrounding the orthopyroxene in the Kebne Dyke Complex supports this interpretation as well. The breakdown of ilmenite to titanite or rutile might in addition to pressure and temperature depend on the composition of reacting fluids and therefor be more resistant and unaltered within the Kebne Dyke Complex. Additionally in the result we see the presence of epidote within the amphibolites. This suggests that the occurrence of metamorphic alteration may be due to a more permeable protolith. The veins which are often seen running through xenoliths within the Kebne Dyke Complex suggest a later occurrence of hydrothermal activity. This activity might be due to a rock with low permeability restricting fluid flow to fractures. These veins therefore gives yet another supporting evidence for this theory of metamorphism affecting separate protoliths with different permeability.

The Kebne Dyke Complex bedrock units equivalent in the Sarek mountains is considered to be the Sarektjåkkå nappe (Andréasson 2020). These two bedrock units display similar traits with less obvious signs of metamorphism. The estimated metamorphic conditions of the Tarfala Amphibolite are of high-pressure Amphibolite facies in this study and may be compared to the high pressure and temperature estimates from the Vaimok and Tsäkokk lenses which surrounds the Sarektjåkkå nappe. Although not proven, the similarity between the two areas containing a bedrock unit with less obvious signs of metamorphism surrounded by bedrock units with higher pressure and temperature estimates may imply a relationship between them. The similarities could imply a continuation of high-pressure metamorphic conditions to the north. The trend with a decrease of pressure and temperature towards the north might be the result of the oblique motion during closing of the

Iapetus-Ocean when a proposed subduction event might have occurred. On the whole, more research is needed to better understand the geological history of the Caledonian orogen.

5. Conclusions

Conclusions that can be made in this study, based on field observations, petrographic analysis, geochemical analysis and pressure-temperature modelling with THERMOCALC are;

- There is some evidence of thrust duplication of the Seve nappe recorded by the repetition of the mylonite -gneiss -amphibolite sequence. However, more evidence is needed for a confident conclusion to be reached.

-The Tarfala Amphibolite has experienced peak metamorphic conditions in the high-pressure Amphibolite facies with a temperature of approximately 606±27 °C and a pressure of approximately 1.13±0.1 GPa.

-The Kebne Dyke Complex displays signs of metamorphic alteration in the form of faint foliation and hornblende reaction rims surrounding orthopyroxene.

-Hydrothermal alteration is found in the Tarfala Amphibolite and the Kebne Amphibolite as areas displaying epidotization. Hydrothermal activity is also indicated by veining of the Kebne Dyke Complex rocks.

-At this point we can't rule out the possibility of the Kebne Dyke Complex being metamorphosed at the same Amphibolite-facies conditions as the amphibolites and preserved due to lower permeability.

-Zircons are found in the Tarfala Amphibolite which could be used for U-Pb isotopic analysis.

6. Acknowledgements

First and foremost, I would like to thank my supervisor Alasdair Skelton. I thank him for his valuable support and sharing of knowledge in both distance supervision by computer and in field studies. This project would also not have been possible without the great accommodation and support from the staff at the Tarfala research station. A special thank you I would like to direct to Nina Kirschner, Annika Granebeck and Per Holmlund. Nina and Annika for being sources of inspiration as well as great early morning company and Per for his sharing of knowledge and guidance of the local area. Thank you to Susanne Hjerp for good company during long fieldwork and lab-work days. Finally, I will direct a thank you to my family for their endless support and inspiration.

7. References

Andréasson, P. G. (2020). The continent-ocean (Seve-Köli) boundary in the Sarek-Padjelanta Mts. revisited: Swedish Caledonides. *GFF, 142(2)*, 125-138. doi:10.1080/11035897.2020.1748898

Andréasson, P. G., & Gee, D. G. (1989). Bedrock Geology and Morphology of the Tarfala Area, Kebnekaise Mts., Swedish. *Geografiska Annaler, 71*, 235-239.

Andréasson, P. G., Allen, A., Aurell, O., Boman, D., Ekestubbe, J., Goerke, U., Nilsson, P., Sandelin, S. (2018). Seve terranes of the Kebnekaise Mts., Swedish Caledonides and their amalgamation, accretion and affinity. *GFF, 140(3)*, 264-291. doi:10.1080/11035897.2018.1470200

Andréasson, P. G., Svenningsen, O. M., & Albrecht, L. (1998). Dawn of Phanerozoic orogeny in the north Atlantic tract; Evidence from the Seve-Kalak superterrane, Scandinavian Caledonides. *GFF, 120*, 159-172. doi:10.1080/11035899801202159

Baird, G. B. (2004). *On the Bedrock of the Tarfala Valley: Preliminary Results of 2003 and 2004 Fieldwork.* Tarfala Research Station Annual Report 2003/2004. Retrieved from https://bolin.su.se/data/tarfala/reports.php

Baird, G. B. (2008). *Summary of the summer 2008 field investigations on the bedrock geology of the Tarfala Valley.* Tarfala Research Station Annual Report 2007/2008. Retrieved from https://bolin.su.se/data/tarfala/reports.php

Baird, G. B., & Chamberlain, K. R. (2014). Intrusive age and geochemistry of the Kebne Dyke Complex in the Seve Nappe Complex, Kebnekaise Massif, arctic Sweden Caledonides. *GFF, 136(4)*, 556-570. doi:10.1080/11035897.2014.924553

Bukała, M., Majka, J., Walczak, K., Włodek, A., Schmitt, M. & Zagórska, A. (2020). U-Pb Zircon Dating of Migmatitic Paragneisses and Garnet Amphibolite from the high-pressure Seve Nappe Complex in Kittelfjäll, Swedish Caledonides. *Minerals, 10(295).* doi:10.3390/min10040295

Carl Zeiss NTS ltd. (2011). *Operator's User Guide, ΣIGMA^TM FESEM* (en01 ed.). Carl Zeiss NTS ltd.

Etzel, T. M., & Catlos, E. J. (2021). Garnet Chemical Zoning Based Thermobarometry: Method Evaluation and Applications in the Menderes Massif, Western Turkey. *Geosciences, 11 (12)*, 505. doi:https://doi.org/10.3390/geosciences11120505

Ferry, J. M., & Spear, F. S. (1978). Experimental Calibration of the Partitioning of Fe and Mg Between Biotite and Garnet. *Contributions to Mineralogy and Petrology, 66*, 113-117.

Gee, D. G. (2021). Caledonides of Scandinavia, Greenland and Svalbard. *Encyclopedia of Geology*, 311-327. doi:10.1016/B978-0-08-102908-4.00119-3

Gee, D. G., & Zachrisson, E. (1979). The Caledonides in Sweden.

Gee, D. G., Fossen, H., Henriksen, N., & Higgins, A. K. (2008). From the early Palaeozoic platforms of Baltica and Laurentia to the Caledonide orogen of Scandinavia and Greenland. *Episodes, 31(1)*, 55-51. doi:10.18814/epiiugs/2008/v31i1/007

Gee, D. G., Janák, M., Majka, J., Robinson, P., & van Roermund, H. (2012). Subduction along and within the Baltoscandian margin during closing of the Iapetus Ocean and Baltica-Laurentia collision. *Lithosphere, 5 (2)*, 169-178. doi:doi: 10.1130/L220.1

Greiling, R. O., & Grimmer, J. C. (2007). Köli nappes in the north-central Swedish Caledonides -new views on stratigraphy and structural evolution. *GFF, 129*, 141-153.

Holland, T. J., & Powell, R. (1998). An internally consistent thermodynamic data set for phases of petrological interest. *Journal of metamorphic Geology, 16*, 309-343.

Holland, T., & Powell, R. (1994). Optimal geothermometry and geobarometry. *American Mineralogist, 79*, 120-133.

Koziol, A. M., & Newton, R. C. (1988). Redetermination of the anorthite breakdown reaction and improvement of the plagioclase-garnet-Al2SiO5-quartz geobarometer. *American Mineralogist, 73*, 216-223.

Lundqvist J., L. T. (2001). *Sveriges geologi från urtid till nutid* (3rd ed.). Lund: Studentlitteratur AB.

Marshak, S. (2001) *EARTH Portarait of a planet* (5th ed.) New York: W.W Norton & Company, inc.

OpenStreetMap Contributors (2022) *Online coordinates converter. Website:* https:// coordinates-converter.com accessed: 2022-03-04

Petroleum Experts. (2015). Field Move. Google Commerce Ltd. Retrieved 2021, from https://www.petex.com/products/move-suite/digital-field-mapping/

Stephens, M. B., Gustafsson, M., Ramberg, I. B., & Zachrisson, E. (1985). The Caledonides of the central-north Scandinavia - a techtonostratigraphic overview. In D. G. Gee, & B. A. Sturt (Eds.), *The Caledonide Orogen - Scandinavia and related areas* (pp. 135-162).

Svenningssen, O. M. (2001). Onset of seafloor spreading in the Iapetus Ocean at 608 Ma: precise age of the Sarek dyke swarm, northern Caledonides. *Precambrian research, 110 (1-4)*, 241-254. doi:10.1016/S0301-9268(01)00189-9

Torsvik, T. H., Smethurst, M. A., W. S., Meert, J. G., Van der Voo, R., McKerrow, W.S., Brasier, M. D., Sturt, B. A., Walderhaug, H. J. (1996). Continental break-up and collision in the Neoproterozoic and Palaeozoic- A tale of Baltica and Laurentia. *Earth-Science Reviews 40*, 229-258.

Winter, J. D. (2014). *Principles of Igneous and Metamorphic Petrology* (2 ed.). Edinburgh gate: Pearson.

8. Appendix

8.1 Appendix A, Maps

Overview map

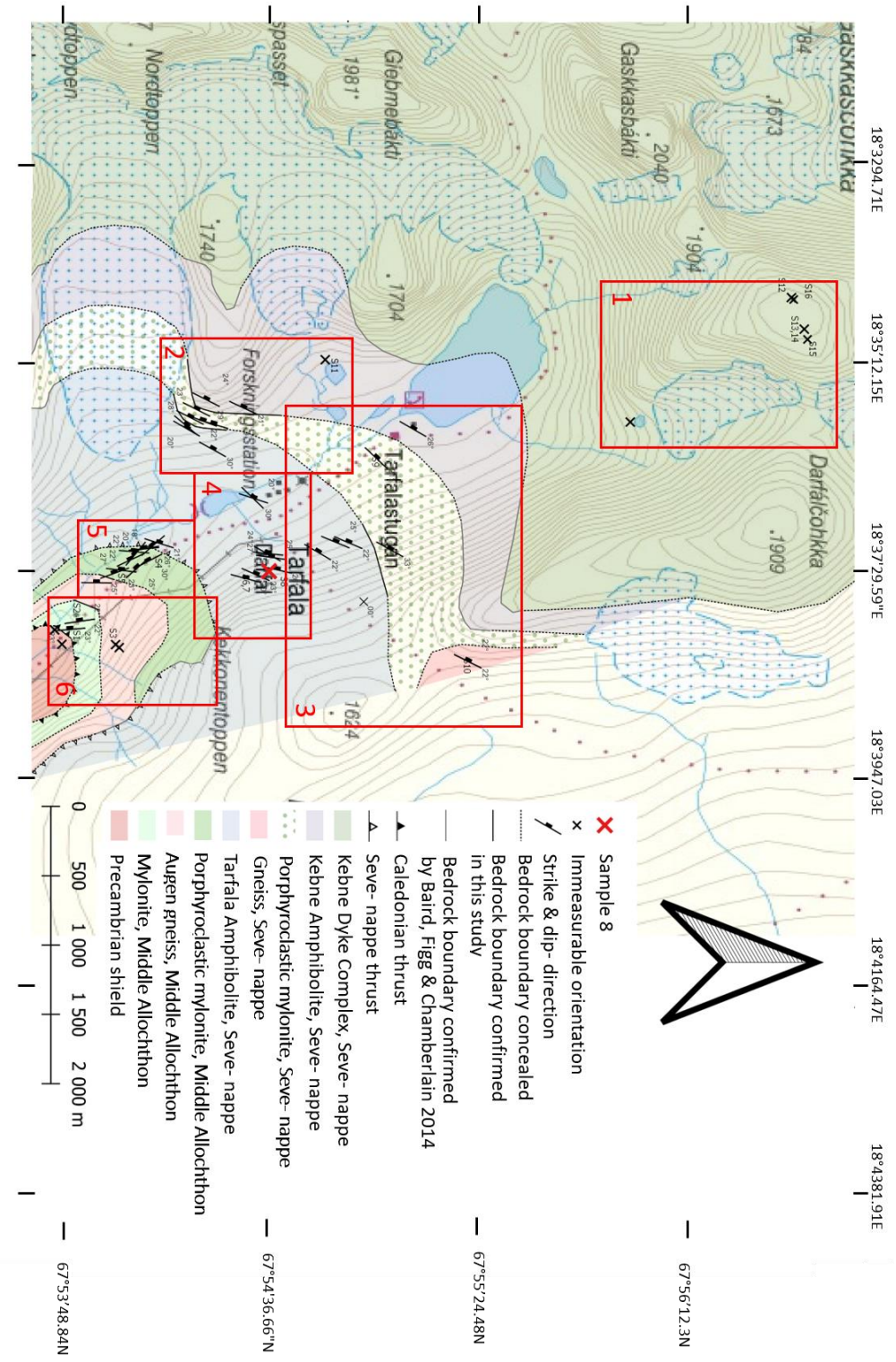

Figure 67. Overview map showing the areas for the magnifications.

Magnifications

Magnification 1.

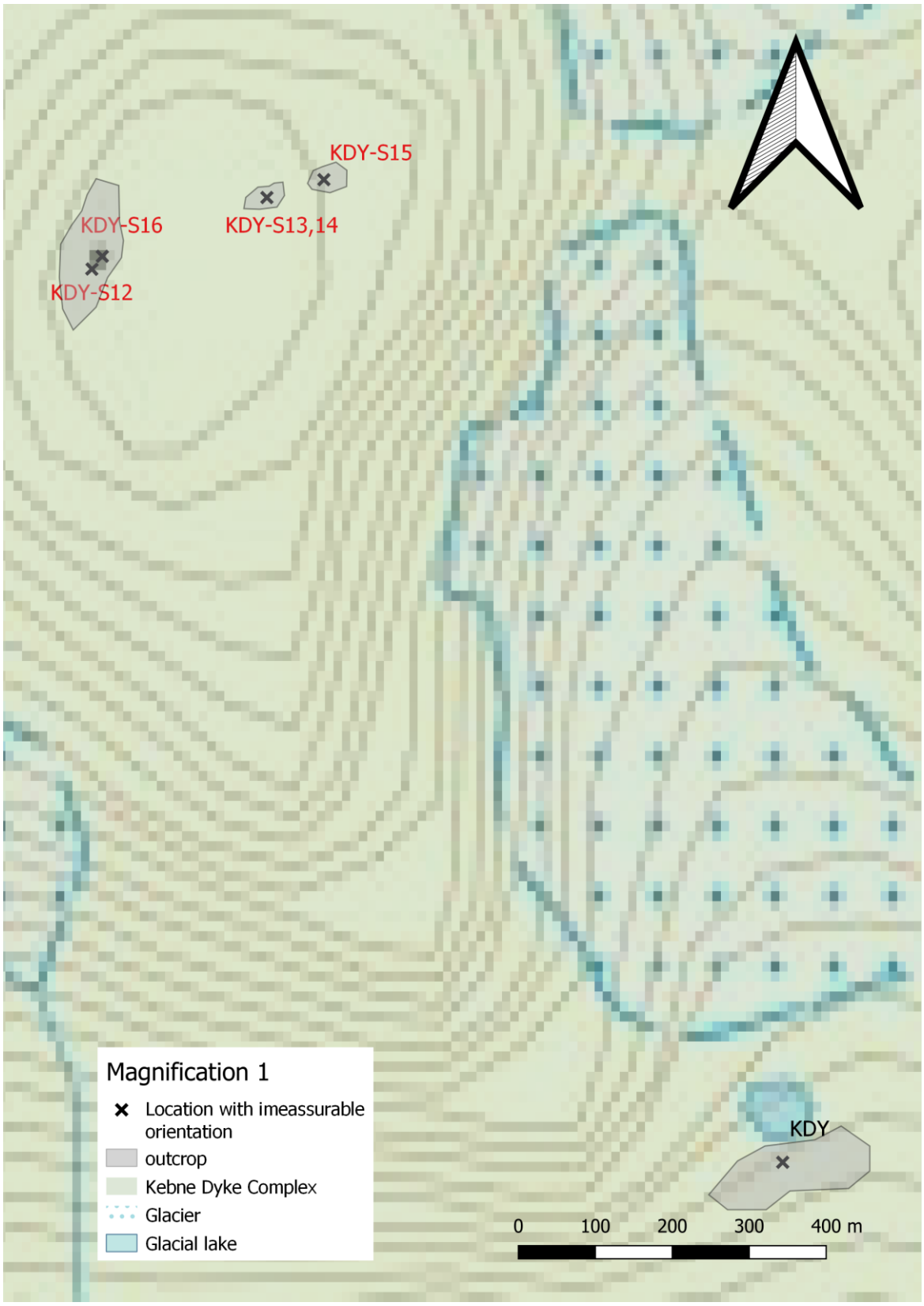

Figure 68. Magnification displaying sample locations and approximate shape of outcrop. KDY stands for Kebne Dyke Complex.

Magnification 2

Figure 69. Magnification displaying all collected measurements of Strike and dip-direction, sample locations and approximate shape of outcrops.

Magnification 3

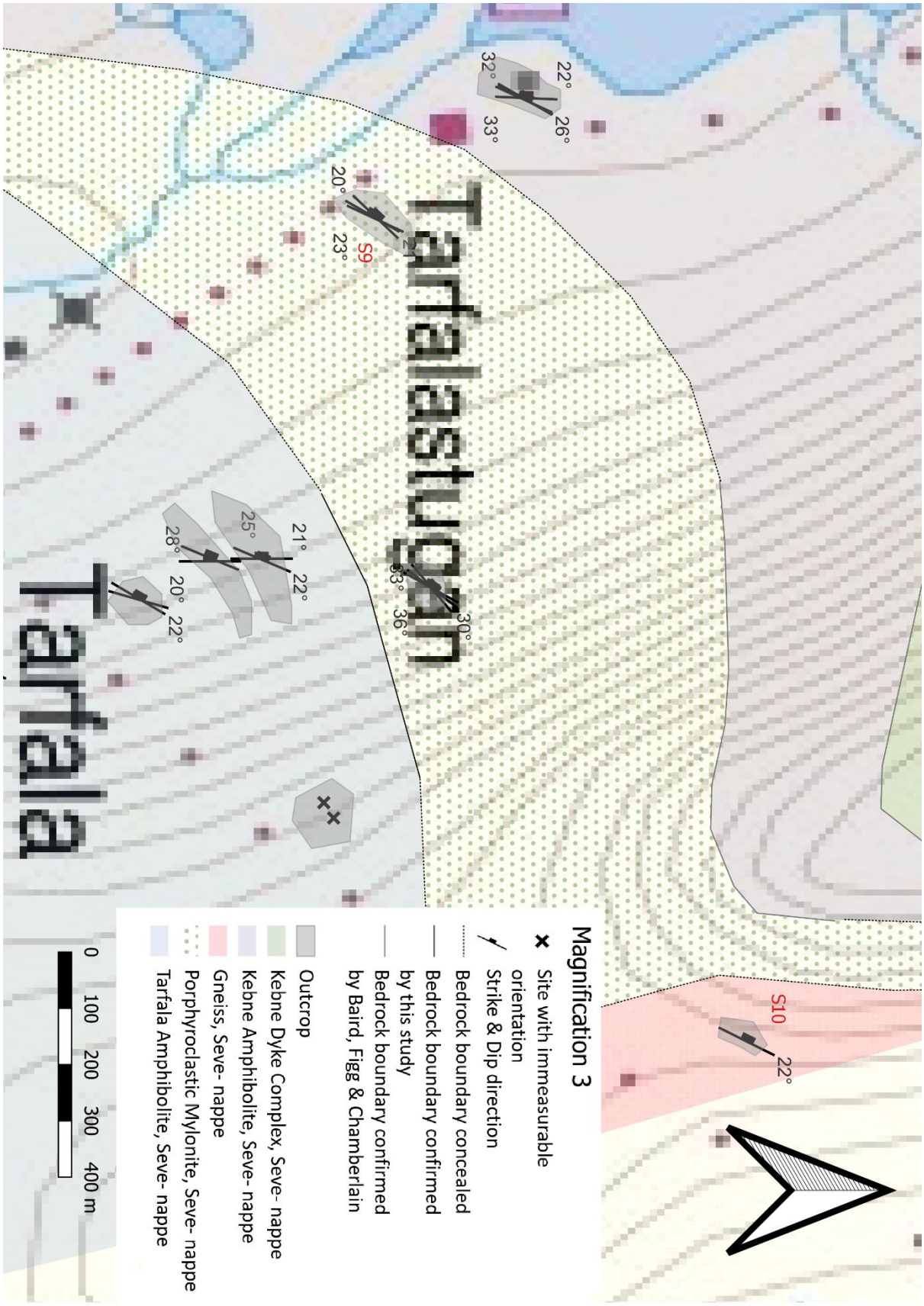

Figure 70. Magnification displaying all collected measurements of Strike and dip-direction, sample locations and approximate shape of outcrops.

Magnification 4

Figure 71. Magnification displaying all collected measurements of Strike and dip-direction, sample locations and approximate shape of outcrops. Note that the thrust symbols (fig. 7) are excluded in this magnification.

Magnification 5

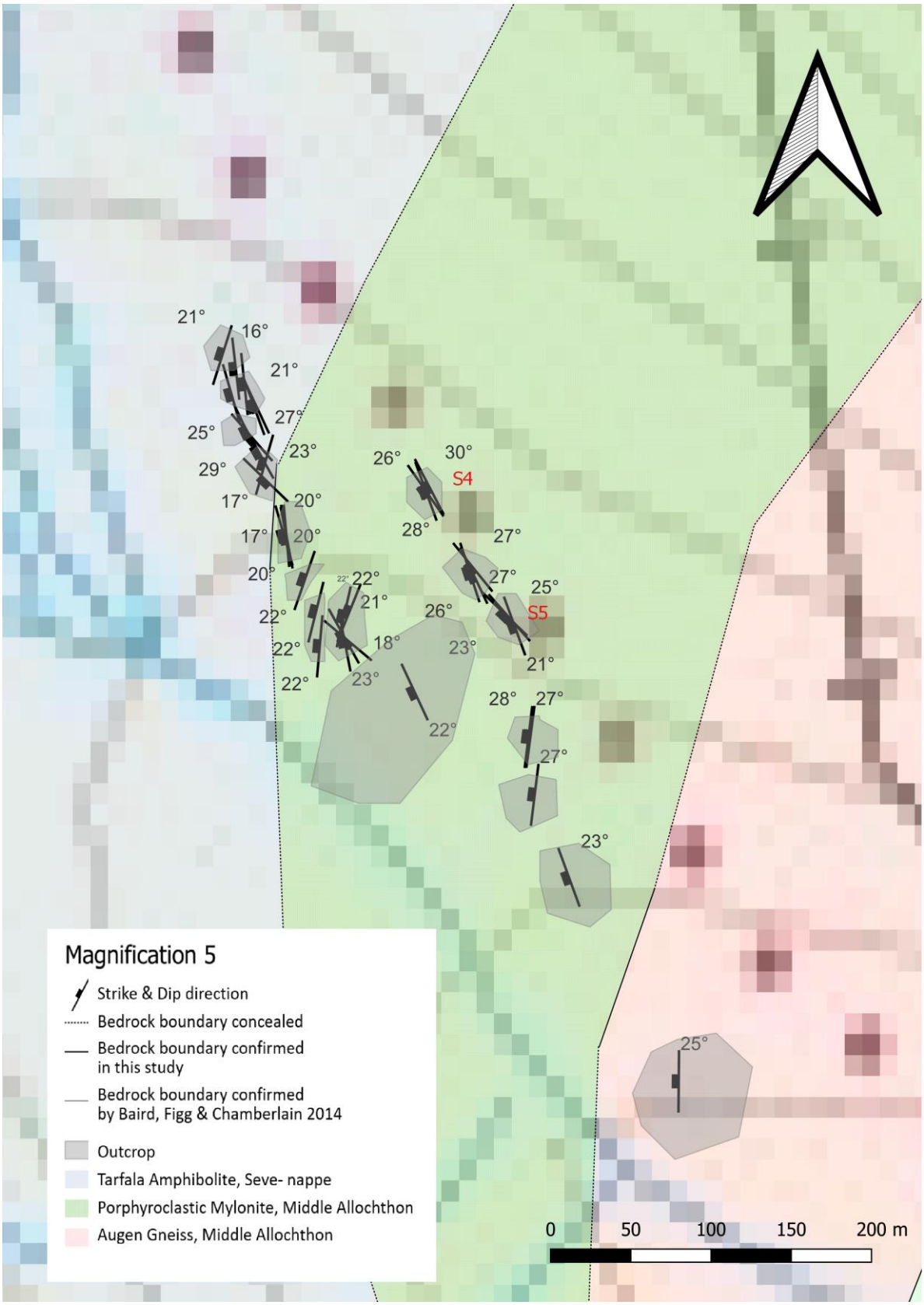

Figure 72. Magnification displaying all collected measurements of Strike and dip-direction, sample locations and approximate shape of outcrops. Note that the thrust symbols (fig. 7) are excluded in this magnification.

Magnification 6

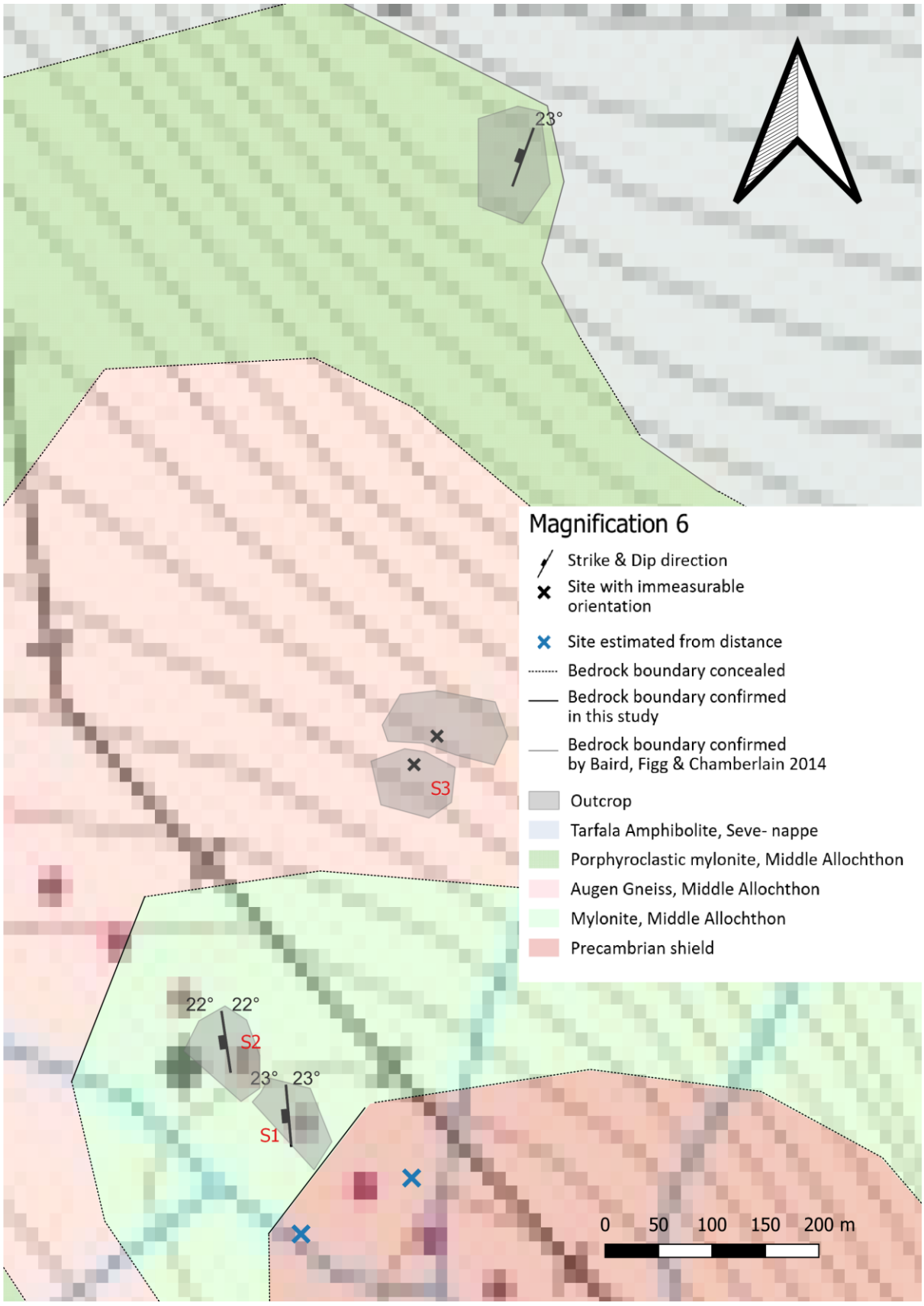

Figure 73. Magnification displaying all collected measurements of Strike and dip-direction, sample locations and approximate shape of outcrops. Note that the thrust symbols (fig. 7) are excluded in this magnification.

8.2 Appendix B, Tables

Table A1. List of collected samples with corresponding thin sections, locations and map-magnification in appendix A.

Sample number	Thin-section number	Bedrock type	Thin section name	Location coordinates	Magnification number in Appendix
1	1	Mylonite	TA-MYL-L16-01	67°53'54.15"N/ 18°37'58.99"E	6
2	2	Mylonite	TA-MYL-L19-01A	67°53'57.02"N/ 18°37'53.37"E	6
2	3	Mylonite	TA-MYL-L19-01B	67°53'57.02"N/ 18°37'53.37"E	6
3	4	Augen Gneiss	TA-GNE-L13-01	67°54'04.80"N/ 18°38'07.25"E	6
4	5	Porphyroclastic Mylonite	TA-MEN-L11-01A	67°54'10.57"N/ 18°37'21.93"E	5
4	6	Porphyroclastic Mylonite	TA-MEN-L11-01B	67°54'10.57"N/ 18°37'21.93"E	5
5	7	Porphyroclastic Mylonite	TA-GNE/MEN-L12-01A	67°54'07.87"N/ 18°37'23.80"E	5
5	8	Porphyroclastic Mylonite	TA-GNE/MEN-L12-01B	67°54'07.87"N/ 18°37'23.80"E	5
5	9	Porphyroclastic Mylonite	TA-GNE/MEN-L12-01C	67°54'07.87"N/ 18°37'23.80"E	5
6	10	Tarfala Amphibolite	TA-AMN-L4-01	67°54'32.52"N/ 18°37'30.48"E	4
7	11	Tarfala Amphibolite	TA-AMN-L4-02A	67°54'32.52"N/ 18°37'30.48"E	4
7	12	Tarfala Amphibolite	TA-AMN-L4-02B	67°54'32.52"N/ 18°37'30.48"E	4
8	13	Tarfala Amphibolite	TA-AMN-L14-01	67°54'36.66"N/ 18°37'29.59"E	4
9	14	Porphyroclastic Mylonite	TA-MEO-L2-01	67°55'00.51"N/ 18°36'16.01"E	3
10	15	Gneiss	TA-MEO-L15-01	67°55'17.96"N/ 18°38'34.70"E	3
11	16	Kebne Amphibolite	TA-AMO-L1-01A	67°54'51.84"N/ 18°35'12.15"E	2
11	17	Kebne Amphibolite	TA-AMO-L1-01B	67°54'51.84"N/ 18°35'12.15"E	2
11	18	Kebne Amphibolite	TA-AMO-L1-01C	67°54'51.84"N/ 18°35'12.15"E	2
11	19	Kebne Amphibolite	TA-AMO-L1-01D	67°54'51.84"N/ 18°35'12.15"E	2
11	20	Kebne Amphibolite	TA-AMO-L1-01E	67°54'51.84"N/ 18°35'12.15"E	2
11	21	Kebne Amphibolite	TA-AMO-L1-01F	67°54'51.84"N/ 18°35'12.15"E	2
12	22	Kebne Dyke Complex	TA-KDY-L17-01	67°56'31.21"N/ 18°34'45.33"E	1
13	23	Kebne Dyke Complex	TA-KDY-L18-01	67°56'33.92"N/ 18°35'14.57"E	1
14	24	Kebne Dyke Complex	TA-KDY-L18-02	67°56'33.92"N/ 18°35'14.57"E	1
15	25	Kebne Dyke Complex	TA-KDY-L18-03	67°56'33.92"N/ 18°35'14.57"E	1
16	26	Kebne Dyke Complex	TA-KDY-L20-01	67°56'32.97"N/ 18°34'48.43"E	1

Table A1. List of collected samples with corresponding thin sections, bedrock-type, locations and map-magnification in appendix A. Sample number 1-5 belong to the Middle Allochthon and Sample number 6-16 belong to the upper part of the Middle Allochthon; Seve nappe. Sample 8 which in this study is investigated for metamorphic P-T conditions is highlighted. For sample locations see referred magnification in appendix A.

Table A2. Oxide conversion factors

MgO	1.6582760749
Al2O3	1.8894636852
SiO2	2.1393352442
CaO	1.3991866267
MnO	1.2912264735
FeO	1.2864862929
TiO2	1.6680334029
Na2O	1.3479678135
K2O	1.2046048038
ZrO2	1.3507871081
HfO2	1.1792750294

Table A2. Table displays the oxide conversion factors which were used to convert elemental content to oxides by multiplication.

Table A3. Thin-section 13, Garnet elemental compositional chemistry table

Site	Oxygen	Magnesium	Aluminium	Silicon	Calcium	Manganese	Iron	total
1	37.17 (39.13)	1.25 (1.32)	11.21 (11.8)	15.28 (16.09)	7.94 (8.36)	1.62 (1.7)	20.51 (21.6)	94.98 (100)
2	37.68 (39.27)	1.25 (1.3)	11.19 (11.66)	15.25 (15.89)	7.95 (8.28)	1.07 (1.11)	21.57 (22.48)	95.96 (100)
4	37.52 (38.8)	1.36 (1.4)	11.62 (12.02)	15.97 (16.52)	8.16 (8.44)	1.73 (1.79)	20.35 (21.04)	96.71 (100)
9	39.14 (40.18)	1.13 (1.16)	11.38 (11.68)	15.44 (15.85)	8.29 (8.51)	0.76 (0.78)	21.27 (21.84)	97.41 (100)

Table 1. Compositional elemental data from Garnet achieved by SEM/EDS At Luleå University of technology. Normalized values are displayed within parentheses.

Table A4. Thin-section 13, Garnet elemental-oxide chemistry table

Site	MgO	Al2O3	SiO2	CaO	MnO	FeO	total
1	2.19 (2.18)	22.30 (22.17)	34.42 (34.22)	11.70 (11.63)	2.20 (2.18)	27.79 (27.63)	100.6 (100)
2	2.16 (2.15)	22.03 (22.00)	33.99 (33.95)	11.59 (11.57)	1.43 (1.43)	28.92 (28.89)	100.12 (100)
4	2.32 (2.29)	22.71 (22.36)	35.34 (34.80)	11.81 (11.63)	2.31 (2.28)	27.07 (26.65)	101.56 (100)
9	1.92 (1.94)	22.07 (22.31)	33.91 (34.28)	11.91 (12.04)	1.01 (1.02)	28.10 (28.41)	98.92 (100)

Table 2. Garnet elemental-oxide composition calculated from elemental composition times the oxide conversion factors. Normalized values are displayed within parentheses.

Table A5. Thin-section 13, Hornblende elemental compositional chemistry table

Site*	Oxygen	Sodium	Magnesium	Aluminium	Silicon	Potassium	Calcium	Titanium	Iron	Sum
1	40.35 (41.84)	1.53 (1.58)	5.28 (5.48)	7.41 (7.68)	17.48 (18.12)	0.9 (0.94)	8.83 (9.15)	0.57 (0.6)	14.08 (14.6)	96.44 (100)
2	38.83 (41.42)	1.49 (1.59)	5.05 (5.39)	7.55 (8.05)	17.33 (18.49)	0.89 (0.95)	8.84 (9.43)	0.58 (0.62)	13.18 (14.06)	93.75 (100)
3	39.29 (41.58)	1.5 (1.59)	5.41 (5.73)	7.41 (7.84)	17.33 (18.34)	0.97 (1.03)	8.62 (9.12)	0.58 (0.62)	13.38 (14.16)	94.49 (100)
4	39.74 (41.59)	1.55 (1.62)	5.5 (5.75)	7.52 (7.87)	17.61 (18.44)	0.95 (1.00)	8.58 (8.98)	0.58 (0.61)	13.51 (14.14)	95.53 (100)

*Table 5. Compositional elemental data from Hornblende achieved by SEM/EDS At Luleå University of technology. Normalized values are displayed within parentheses. *Site 1 & 2 lies in direct contact with the Metapelite part of the thin-section, site 3 & 4 lies within the Amphibolite part of the thin- section.*

Table A6. Thin-section 13, Hornblende elemental-oxide chemistry table

Site*	Na2O	MgO	Al2O3	SiO2	K2O	CaO	TiO	FeO	Sum
1	2.13 (2.17)	9.09 (9.25)	14.51 (14.78)	38.76 (39.47)	1.13 (1.15)	12.80 (13.03)	1.00 (1.02)	18.78 (19.12)	98.2 (100)
2	2.14 (2.16)	8.94 (9.00)	15.21 (15.32)	39.56 (39.83)	1.14 (1.15)	13.19 (13.29)	1.03 (1.04)	18.09 (18.21)	99.3 (100)
3	2.14 (2.17)	9.50 (9.60)	14.81 (14.97)	39.24 (39.65)	1.24 (1.25)	12.76 (12.90)	1.03 (1.05)	18.22 (18.41)	98.94 (100)
4	2.18 (2.21)	9.54 (9.63)	14.87 (15.02)	39.45 (39.84)	1.20 (1.22)	12.56 (12.69)	1.02 (1.03)	18.19 (18.37)	99.01 (100)

*Tabell 6. Hornblende elemental-oxide composition calculated from elemental composition times the oxide conversion factors. Normalized values are displayed within parentheses. *Site 1 & 2 lies in direct contact with the Metapelite part of the thin- section, site 3 & 4 lies within the Amphibolite part of the thin- section.*

Table A7. Thin-section 13, Biotite elemental compositional chemistry table

Site	Oxygen	Magnesium	Aluminium	Silicon	Potassium	Titanium	Iron	Sum
1	38.10 (42.05)	6.09 (6.72)	8.33 (9.19)	14.43 (15.92)	6.92 (7.64)	1.80 (1.98)	14.95 (16.49)	90.62 (100)
2	36.83 (40.69)	6.23 (6.88)	8.55 (9.44)	14.97 (16.53)	7.19 (7.94)	1.80 (1.99)	14.96 (16.52)	90.46 (100)
3	37.02 (40.98)	6.10 (6.75)	8.47 (9.38)	14.78 (16.35)	7.22 (7.99)	1.93 (2.14)	14.83 (16.41)	90.35 (100)
4	37.14 (41.17)	6.31 (7.00)	8.2 (9.09)	14.64 (16.23)	6.9 (7.65)	1.69 (1.87)	15.33 (17.00)	90.21 (100)

Table 7. Compositional elemental data from Biotite achieved by SEM/EDS At Luleå University of technology. Normalized values are displayed within parentheses.

Table A8. Thin-section 13, Biotite elemental-oxide chemistry table

Site	MgO	Al2O3	SiO2	K2O	TiO	FeO	Sum
1*	11.14 (11.57)	17.36 (18.03)	34.06 (35.37)	9.20 (9.56)	3.30 (3.43)	21.21 (22.03)	96.27 (100)
2	11.41 (11.55)	17.84 (18.06)	35.36 (35.81)	9.56 (9.69)	3.32 (3.36)	21.25 (21.52)	98.74 (100)
3	11.19 (11.40)	17.72 (18.05)	34.98 (35.62)	9.62 (9.80)	3.57 (3.64)	21.11 (21.50)	98.19 (100)
4	11.61 (11.88)	17.18 (17.58)	34.72 (35.54)	9.22 (9.43)	3.12 (3.19)	21.87 (22.38)	97.72 (100)

*Table 8. Biotite elemental-oxide composition calculated from elemental composition times the oxide conversion factors. Normalized values are displayed within parentheses. *Analyse-time shorter.*

Table A9. Thin-section 13, Plagioclase elemental compositional chemistry table

Site*	Oxygen	Sodium	Aluminium	Silicon	Calcium	Sum
1	42.14 (47.46)	5.98 (6.73)	11.81 (13.31)	25.7 (28.95)	3.16 (3.56)	88.79 (100)
2	40.83 (47.29)	5.62 (6.51)	11.65 (13.49)	24.81 (28.73)	3.44 (3.98)	86.35 (100)
3	40.66 (47.6)	5.82 (6.81)	11.18 (13.09)	24.83 (29.07)	2.93 (3.43)	85.42 (100)
4	39.68 (47.69)	5.47 (6.57)	10.93 (13.13)	24.04 (28.89)	3.1 (3.72)	83.22 (100)

*Table 9. Compositional elemental data from Plagioclase achieved by SEM/EDS At Luleå University of technology. Normalized values are displayed within parentheses. * *Site 1 & 2; Analyse made within Metapelite part of thin-section, site 3 & 4; Analyse made of Plagioclase within &Amphibolite part of thin- section.*

Table A10. Thin-section 13, Plagioclase elemental-oxide chemistry table

Site*	Na2O	Al2O3	SiO2	CaO	Sum
1	9.07 (8.97)	25.15 (24.87)	61.93 (61.24)	4.98 (4.93)	101.13 (100)
2	8.78 (8.66)	25.49 (25.16)	61.46 (60.68)	5.57 (5.50)	101.3 (100)
3	9.18 (9.10)	24.73 (24.51)	62.19 (61.63)	4.80 (4.76)	100.9 (100)
4	8.86 (8.80)	24.81 (24.64)	61.81 (61.39)	5.20 (5.17)	100.68 (100)

*Table 10. Plagioclase elemental-oxide composition calculated from elemental composition times the oxide conversion factors. Normalized values are displayed within parentheses. *Site 1 & 2; Analyse made within Metapelite part of thin-section, site 3 & 4; Analyse made of Plagioclase within &Amphibolite part of thin- section.*

Table A11. Thin-section 13, Titanite elemental compositional chemistry table

Site	Oxygen	Aluminium	Silicon	Calcium	Titanium	Sum
1*	40.74 (41.33)	1.02 (1.03)	12.46 (12.64)	21.94 (22.26)	22.4 (22.73)	98.56 (100)
2*	37.71 (39.98)	1.15 (1.22)	13.25 (14.05)	20.18 (21.4)	22.02 (23.35)	94.31 (100)
3	40.62 (41.95)	0.88 (0.9)	12.47 (12.88)	19.6 (20.24)	23.25 (24.02)	96.82 (100)
4	39.61 (40.7)	0.9 (0.92)	12.51 (12.85)	20.3 (20.86)	24.02 (24.67)	97.34 (100)

*Table 11. Compositional elemental data from Titanite, achieved by SEM/EDS At Luleå University of technology. Normalized values are displayed within parentheses. *Analyse time shorter.*

Table A12. Titanite elemental-oxide Chemistry table

Site	Al2O3	SiO2	CaO	TiO	Sum
1*	1.95 (1.98)	27.04 (27.58)	31.15 (31.77)	37.91 (38.67)	98.05 (100)
2*	2.31 (2.28)	30.06 (29.69)	29.94 (29.57)	38.95 (38.47)	101.26 (100)
3	1.70 (1.74)	27.55 (28.22)	28.32 (29.00)	40.07 (41.03)	97.64 (100)
4	1.74 (1.75)	27.49 (27.61)	29.19 (29.31)	41.15 (41.33)	99.57 (100)

*Table 12. Titanite elemental-oxide composition calculated from elemental composition times the oxide conversion factors. Normalized values are displayed within parentheses. * Analyse time shorter.*

Table A13. Thin-section 13, Zircon (inclusion in Garnet) elemental compositional chemistry table

Site	Oxygen	Silicon	Iron	Zirconium	Hafnium	Sum
1	29.40 (31.75)	14.03 (15.15)	1.00 (1.08)	47.26 (51.03)	0.92 (0.99)	92.61 (100)

Table 13. Compositional elemental data from Zircon inclusion within a Garnet, achieved by SEM/EDS At Luleå University of technology. Normalized values are displayed within parentheses.

Table A14. Thin-section 13, Zircon (inclusion in Garnet) elemental-oxide chemistry table

Site	SiO2	FeO	ZrO2	HfO2	Sum
1	32.41 (32.83)	1.39 (1.41)	63.84 (64.66)	1.08 (1.10)	98.72 (100)

Table 14. Zircon elemental-oxide composition calculated from elemental composition times the oxide conversion factors. Normalized values are displayed within parentheses

Table A15. Thin-section 13, Inclusion in Titanite, elemental compositional chemistry table

Oxygen	Titanium	Iron	Sum
31.45 (32.01)	31.41 (31.97)	35.39 (36.02)	98.25 (100)

Table A15. Elemental contents of inclusion within a Titanite crystal.

Table A16. Thin-section 13, Inclusion in Titanite, elemental-oxide chemistry table

TiO	FeO	Sum
53.33 (53.51)	46.34 (46.49)	99.67 (100)

Table A16. Elemental oxide contents of inclusion within Titanite.

Table A17. Thin-section 13, Titanite (inclusion in Amphibole) elemental compositional chemistry table

Oxygen	Aluminium	Silicon	Calcium	Titanium	Sum
39.77 (40.38)	0.78 (0.79)	12.24 (12.43)	21.11 (21.43)	24.57 (24.96)	98.47 (100)

Table A17. Elemental contents of Titanite inclusion within Amphibole.

Table A18. Thin-section 13, Titanite (inclusion in Amphibole) elemental-oxide chemistry table

Al2O3	SiO2	CaO	TiO	Sum
1.49 (1.50)	26.59 (26.67)	29.98 (30.07)	41.63 (41.76)	99.69 (100)

Table A18. Elemental-oxide contents of Titanite inclusion within Amphibole.

8.3 Appendix C, THERMOCALC diagnostics

Copies of the THERMOCALC diagnostics are presented below. Chosen pressure-temperature estimates with the best sigfit value are highlighted in yellow.

Metapelite diagnostics

Run 1:

an independent set of reactions has been calculated
Activities and their uncertainties

	py	gr	alm	phl	ann	east	an
a	0.00412	0.0500	0.0870	0.0360	0.0340	0.0420	0.390
sd(a)/a	0.63457	0.35902	0.28736	0.39392	0.41133	0.37927	0.11163

	ab	q	H2O	mu	pa
a	0.770	1.00	1.00	1.00	1.00
sd(a)/a	0.05000	0	0	0	

Independent set of reactions
1) py + phl + 2mu = 3east + 6q
2) py + 2gr + 3east + 6q = 3phl + 6an
3) gr + alm + mu = ann + 3an
4) 2py + 3gr + 3mu + 4pa = 3east + 9an + 4ab + 4H2O

Calculations for the independent set of reactions
(for x(H2O) = 1.0)

	P(T)	sd(P)	a	sd(a)	b	c	ln_K	sd(ln_K)
1	8.0	2.57	-13.50	1.23	-0.01256	3.443	-0.694	1.361
2	12.4	1.21	-0.99	1.59	-0.21539	10.764	5.371	2.014
3	9.0	0.63	37.72	1.15	-0.12791	7.389	-0.769	0.702
4	8.8	0.55	267.31	2.37	-0.65716	26.613	0.941	2.262

Average PT (for x(H2O) = 1.0)

Single end-member diagnostic information

avP, avT, sd's, cor, fit are result of doubling the uncertainty on ln a :
a ln a suspect if any are v different from lsq values.
e* are ln a residuals normalised to ln a uncertainties :
large absolute values, say >2.5, point to suspect info.
hat are the diagonal elements of the hat matrix :
large values, say >0.33, point to influential data.
For 95% confidence, fit (= sd(fit)) < 1.73
however a larger value may be OK - look at the diagnostics!

	avP	sd	avT	sd	cor	fit
lsq	11.6	1.7	613	44	0.880	1.72

	P	sd(P)	T	sd(T)	cor	fit	e*	hat
py	10.95	1.84	595	49	0.914	1.57	0.87	0.35
gr	11.36	2.02	612	44	0.787	1.70	0.19	0.48
alm	12.07	1.72	628	46	0.903	1.55	-0.73	0.14
phl	11.05	1.31	595	35	0.890	1.25	-1.37	0.12
ann	12.35	1.69	636	45	0.913	1.44	1.05	0.29
east	11.70	1.52	614	39	0.879	1.51	1.19	0.02
an	11.39	1.99	612	44	0.796	1.70	-0.18	0.42
ab	11.58	1.74	614	47	0.869	1.72	-0.07	0.08
q	11.57	1.73	613	44	0.880	1.72	0	0

H2O	11.57	1.73	613	44	0.880	1.72	0	0
mu	11.57	1.73	613	44	0.880	1.72	0	0
pa	11.57	1.73	613	44	0.880	1.72	0	0

T = 613¡C, sd = 44,
P = 11.6 kbars, sd = 1.7, cor = 0.880, sigfit = 1.72
==========

Run 2:
an independent set of reactions has been calculated
Activities and their uncertainties

	py	gr	alm	phl	ann	east	an
a	0.00399	0.0500	0.0950	0.0380	0.0350	0.0450	0.430
sd(a)/a	0.63715	0.35902	0.30526	0.38888	0.40751	0.37244	0.09747

	ab	q	H2O	mu	pa
a	0.750	1.00	1.00	1.00	1.00
sd(a)/a	0.05000	0	0	0	

Independent set of reactions
1) py + phl + 2mu = 3east + 6q
2) py + 2gr + 3east + 6q = 3phl + 6an
3) gr + alm + mu = ann + 3an
4) 2py + 3gr + 3mu + 4pa = 3east + 9an + 4ab + 4H2O

Calculations for the independent set of reactions
(for x(H2O) = 1.0)

	P(T)	sd(P)	a	sd(a)	b	c	ln_K	sd(ln_K)
1	7.7	2.53	-13.50	1.23	-0.01256	3.443	-0.509	1.344
2	12.0	1.18	-0.99	1.59	-0.21539	10.764	5.944	1.968
3	8.7	0.62	37.72	1.15	-0.12791	7.389	-0.535	0.688
4	8.6	0.54	267.31	2.37	-0.65716	26.613	1.985	2.200

Average PT (for x(H2O) = 1.0)

Single end-member diagnostic information

avP, avT, sd's, cor, fit are result of doubling the uncertainty on ln a :
a ln a suspect if any are v different from lsq values.
e* are ln a residuals normalised to ln a uncertainties :
large absolute values, say >2.5, point to suspect info.
hat are the diagonal elements of the hat matrix :
large values, say >0.33, point to influential data.
For 95% confidence, fit (= sd(fit)) < 1.73
however a larger value may be OK - look at the diagnostics!

	avP	sd	avT	sd	cor	fit
lsq	11.2	1.6	610	43	0.889	1.64

	P	sd(P)	T	sd(T)	cor	fit	e*	hat
py	10.70	1.76	594	48	0.921	1.52	0.76	0.36
gr	11.03	1.90	609	42	0.793	1.63	0.20	0.54
alm	11.73	1.62	624	44	0.912	1.48	-0.71	0.16
phl	10.74	1.22	592	33	0.899	1.19	-1.31	0.12
ann	11.93	1.61	630	44	0.919	1.41	0.95	0.28
east	11.36	1.39	611	37	0.888	1.41	1.22	0.02
an	11.10	1.82	609	42	0.818	1.63	-0.16	0.36

ab	11.25	1.63	610	45	0.877	1.64	-0.06	0.09
q	11.24	1.62	610	43	0.889	1.64	0	0
H2O	11.24	1.62	610	43	0.889	1.64	0	0
mu	11.24	1.62	610	43	0.889	1.64	0	0
pa	11.24	1.62	610	43	0.889	1.64	0	0

T = 610¡C, sd = 43,
P = 11.2 kbars, sd = 1.6, cor = 0.889, sigfit = 1.64
==========

Run 3:
an independent set of reactions has been calculated
Activities and their uncertainties

	py	gr	alm	phl	ann	east	an
a	0.00594	0.0760	0.0650	0.0370	0.0390	0.0430	0.390
sd(a)/a	0.60353	0.29903	0.32177	0.39138	0.39308	0.37696	0.11163

	ab	q	H2O	mu	pa
a	0.770	1.00	1.00	1.00	1.00
sd(a)/a	0.05000	0	0	0	

Independent set of reactions
1) py + phl + 2mu = 3east + 6q
2) py + gr + mu = phl + 3an
3) gr + alm + mu = ann + 3an
4) 2py + 3gr + 3mu + 4pa = 3east + 9an + 4ab + 4H2O

Calculations for the independent set of reactions
(for x(H2O) = 1.0)

	P(T)	sd(P)	a	sd(a)	b	c	ln_K	sd(ln_K)
1	8.6	2.53	-13.50	1.23	-0.01256	3.443	-1.017	1.340
2	12.0	0.77	-7.24	0.70	-0.11398	7.104	1.581	0.848
3	8.9	0.61	37.72	1.15	-0.12791	7.389	-0.759	0.678
4	9.3	0.53	267.31	2.37	-0.65716	26.613	-0.976	2.142

Average PT (for x(H2O) = 1.0)

Single end-member diagnostic information

avP, avT, sd's, cor, fit are result of doubling the uncertainty on ln a :
a ln a suspect if any are v different from lsq values.
e* are ln a residuals normalised to ln a uncertainties :
large absolute values, say >2.5, point to suspect info.
hat are the diagonal elements of the hat matrix :
large values, say >0.33, point to influential data.
For 95% confidence, fit (= sd(fit)) < 1.73
however a larger value may be OK - look at the diagnostics!

	avP	sd	avT	sd	cor	fit
lsq	11.9	2.2	611	58	0.893	2.29

	P	sd(P)	T	sd(T)	cor	fit	e*	hat
py	10.90	2.30	582	61	0.925	1.98	1.39	0.36
gr	11.77	2.54	610	58	0.816	2.28	0.17	0.40
alm	12.76	2.13	635	57	0.915	1.95	-1.24	0.17
phl	11.22	1.80	588	48	0.903	1.74	-1.73	0.13
ann	12.98	2.08	642	55	0.920	1.85	1.51	0.25

east	12.04	2.11	613	54	0.892	2.14	1.19	0.02
an	11.73	2.61	610	58	0.801	2.28	-0.19	0.50
ab	11.94	2.26	613	62	0.881	2.29	-0.11	0.09
q	11.92	2.24	611	58	0.893	2.29	0	0
H2O	11.92	2.24	611	58	0.893	2.29	0	0
mu	11.92	2.24	611	58	0.893	2.29	0	0
pa	11.92	2.24	611	58	0.893	2.29	0	0

T = 611¡C, sd = 58,
P = 11.9 kbars, sd = 2.2, cor = 0.893, sigfit = 2.29
==========

Run 4:
an independent set of reactions has been calculated
Activities and their uncertainties

	py	gr	alm	phl	ann	east	an
a	0.00449	0.0510	0.0910	0.0390	0.0370	0.0370	0.430
sd(a)/a	0.62754	0.35625	0.27245	0.38642	0.40013	0.39138	0.09747

	ab	q	H2O	mu	pa
a	0.750	1.00	1.00	1.00	1.00
sd(a)/a	0.05000	0	0	0	

Independent set of reactions
1) py + phl + 2mu = 3east + 6q
2) py + 2gr + 3east + 6q = 3phl + 6an
3) gr + alm + mu = ann + 3an
4) 2py + 3gr + 3mu + 4pa = 3east + 9an + 4ab + 4H2O

Calculations for the independent set of reactions
(for x(H2O) = 1.0)

	P(T)	sd(P)	a	sd(a)	b	c	ln_K	sd(ln_K)
1	9.1	2.61	-13.50	1.23	-0.01256	3.443	-1.240	1.386
2	11.7	1.20	-0.99	1.59	-0.21539	10.764	6.452	1.991
3	8.7	0.60	37.72	1.15	-0.12791	7.389	-0.456	0.668
4	8.8	0.54	267.31	2.37	-0.65716	26.613	1.103	2.215

Average PT (for x(H2O) = 1.0)

Single end-member diagnostic information

avP, avT, sd's, cor, fit are result of doubling the uncertainty on ln a :
a ln a suspect if any are v different from lsq values.
e* are ln a residuals normalised to ln a uncertainties :
large absolute values, say >2.5, point to suspect info.
hat are the diagonal elements of the hat matrix :
large values, say >0.33, point to influential data.
For 95% confidence, fit (= sd(fit)) < 1.73
however a larger value may be OK - look at the diagnostics!

	avP	sd	avT	sd	cor	fit
lsq	11.2	1.5	608	40	0.884	1.61

	P	sd(P)	T	sd(T)	cor	fit	e*	hat
py	10.52	1.51	587	41	0.916	1.35	1.09	0.34
gr	11.10	1.84	607	40	0.786	1.61	0.12	0.53
alm	11.75	1.50	623	40	0.907	1.41	-0.77	0.14

```
   phl  10.80   1.25    593    34  0.894   1.24  -1.18  0.12
   ann  12.06   1.42    632    38  0.917   1.26   1.13  0.30
  east  11.31   1.47    608    38  0.883   1.53   0.77  0.02
    an  11.15   1.76    607    40  0.811   1.61  -0.10  0.36
    ab  11.26   1.56    609    43  0.872   1.61  -0.08  0.09
     q  11.24   1.55    608    40  0.884   1.61      0     0
   H2O  11.24   1.55    608    40  0.884   1.61      0     0
    mu  11.24   1.55    608    40  0.884   1.61      0     0
    pa  11.24   1.55    608    40  0.884   1.61      0     0


T = 608¡C, sd = 40,
P = 11.2 kbars, sd = 1.5, cor = 0.884, sigfit = 1.61
================================================
```

Run 9:

```
an independent set of reactions has been calculated
Activities and their uncertainties
            py      gr      alm      phl      ann     east       an
a         0.00301   0.0550    0.100   0.0390   0.0370   0.0370    0.430
sd(a)/a    0.65887  0.34563  0.26000  0.38642  0.40013  0.39138  0.09747

            ab       q      H2O       mu       pa
a          0.750     1.00     1.00     1.00     1.00
sd(a)/a    0.05000        0              0        0

Independent set of reactions
1)  py + phl + 2mu = 3east + 6q
2)  py + 2gr + 3east + 6q = 3phl + 6an
3)  gr + alm + mu = ann + 3an
4)  2py + 3gr + 3mu + 4pa = 3east + 9an + 4ab + 4H2O

Calculations for the independent set of reactions
(for x(H2O) = 1.0)
      P(T)   sd(P)      a   sd(a)        b        c     ln_K sd(ln_K)
1      8.3    2.64  -13.50    1.23  -0.01256    3.443   -0.841    1.401
2     11.6    1.20   -0.99    1.59  -0.21539   10.764    6.701    1.994
3      8.8    0.59   37.72    1.15  -0.12791    7.389   -0.626    0.658
4      8.7    0.55  267.31    2.37  -0.65716   26.613    1.676    2.236

Average PT (for x(H2O) = 1.0)

Single end-member diagnostic information

avP, avT, sd's, cor, fit are result of doubling the uncertainty on ln a :
a ln a suspect if any are v different from lsq values.
e* are ln a residuals normalised to ln a uncertainties :
large absolute values, say >2.5, point to suspect info.
hat are the diagonal elements of the hat matrix :
large values, say >0.33, point to influential data.
For 95% confidence, fit (= sd(fit)) < 1.73
however a larger value may be OK - look at the diagnostics!

        avP    sd    avT    sd   cor   fit
   lsq   11.1   1.3    600    34 0.888  1.34

         P  sd(P)     T  sd(T)    cor    fit    e*   hat
    py  10.59   1.33    587    36  0.918   1.21   0.74  0.33
```

gr	10.91	1.51	600	33	0.794	1.33	0.14	0.52
alm	11.42	1.29	611	35	0.911	1.22	-0.54	0.14
phl	10.69	0.99	588	27	0.897	0.98	-1.05	0.11
ann	11.69	1.27	619	35	0.922	1.13	0.83	0.32
east	11.13	1.13	601	30	0.887	1.18	0.93	0.02
an	10.95	1.45	600	33	0.814	1.34	-0.12	0.37
ab	11.07	1.29	601	36	0.876	1.34	-0.06	0.09
q	11.06	1.28	600	34	0.888	1.34	0	0
H2O	11.06	1.28	600	34	0.888	1.34	0	0
mu	11.06	1.28	600	34	0.888	1.34	0	0
pa	11.06	1.28	600	34	0.888	1.34	0	0

T = 600¡C, sd = 34,
P = 11.1 kbars, sd = 1.3, cor = 0.888, sigfit = 1.34
==========

Amphibolite diagnostics

Run 1:
an independent set of reactions has been calculated
Activities and their uncertainties

	py	gr	alm	phl	ann	east	an
a	0.00412	0.0500	0.0870	0.0360	0.0340	0.0420	0.370
sd(a)/a	0.63457	0.35902	0.28736	0.39392	0.41133	0.37927	0.11907

	ab	q	H2O	mu	pa
a	0.780	1.00	1.00	1.00	1.00
sd(a)/a	0.05000	0	0	0	

Independent set of reactions
1) py + phl + 2mu = 3east + 6q
2) py + 2gr + 3east + 6q = 3phl + 6an
3) gr + alm + mu = ann + 3an
4) 2py + 3gr + 3mu + 4pa = 3east + 9an + 4ab + 4H2O

Calculations for the independent set of reactions
(for x(H2O) = 1.0)

	P(T)	sd(P)	a	sd(a)	b	c	ln_K	sd(ln_K)
1	8.0	2.57	-13.50	1.23	-0.01256	3.443	-0.694	1.361
2	12.6	1.22	-0.99	1.59	-0.21539	10.764	5.055	2.030
3	9.1	0.64	37.72	1.15	-0.12791	7.389	-0.927	0.713
4	8.9	0.56	267.31	2.37	-0.65716	26.613	0.519	2.292

Average PT (for x(H2O) = 1.0)

Single end-member diagnostic information

avP, avT, sd's, cor, fit are result of doubling the uncertainty on ln a :
a ln a suspect if any are v different from lsq values.
e* are ln a residuals normalised to ln a uncertainties :
large absolute values, say >2.5, point to suspect info.
hat are the diagonal elements of the hat matrix :
large values, say >0.33, point to influential data.
For 95% confidence, fit (= sd(fit)) < 1.73
however a larger value may be OK - look at the diagnostics!

	avP	sd	avT	sd	cor	fit
lsq	11.7	1.8	615	45	0.876	1.74

	P	sd(P)	T	sd(T)	cor	fit	e*	hat
py	11.14	1.90	597	50	0.911	1.59	0.85	0.35
gr	11.53	2.07	614	45	0.786	1.72	0.20	0.45
alm	12.25	1.77	630	46	0.900	1.57	-0.73	0.14
phl	11.22	1.34	597	35	0.885	1.25	-1.39	0.12
ann	12.53	1.74	638	46	0.909	1.47	1.04	0.29
east	11.89	1.55	616	39	0.874	1.51	1.24	0.03
an	11.53	2.07	614	45	0.786	1.72	-0.20	0.45
ab	11.76	1.79	616	48	0.865	1.74	-0.07	0.08
q	11.74	1.77	615	45	0.876	1.74	0	0
H2O	11.74	1.77	615	45	0.876	1.74	0	0
mu	11.74	1.77	615	45	0.876	1.74	0	0
pa	11.74	1.77	615	45	0.876	1.74	0	0

T = 615¡C, sd = 45,
P = 11.7 kbars, sd = 1.8, cor = 0.876, sigfit = 1.74
==========

Run 2:

an independent set of reactions has been calculated
Activities and their uncertainties

	py	gr	alm	phl	ann	east	an
a	0.00399	0.0500	0.0950	0.0380	0.0350	0.0450	0.410
sd(a)/a	0.63715	0.35902	0.30526	0.38888	0.40751	0.37244	0.10443

	ab	q	H2O	mu	pa
a	0.760	1.00	1.00	1.00	1.00
sd(a)/a	0.05000	0	0	0	

Independent set of reactions
1) py + phl + 2mu = 3east + 6q
2) py + 2gr + 3east + 6q = 3phl + 6an
3) gr + alm + mu = ann + 3an
4) 2py + 3gr + 3mu + 4pa = 3east + 9an + 4ab + 4H2O

Calculations for the independent set of reactions
(for x(H2O) = 1.0)

	P(T)	sd(P)	a	sd(a)	b	c	ln_K	sd(ln_K)
1	7.7	2.53	-13.50	1.23	-0.01256	3.443	-0.509	1.344
2	12.2	1.19	-0.99	1.59	-0.21539	10.764	5.659	1.981
3	8.9	0.63	37.72	1.15	-0.12791	7.389	-0.678	0.697
4	8.7	0.54	267.31	2.37	-0.65716	26.613	1.610	2.226

Average PT (for x(H2O) = 1.0)

Single end-member diagnostic information

avP, avT, sd's, cor, fit are result of doubling the uncertainty on ln a :
a ln a suspect if any are v different from lsq values.
e* are ln a residuals normalised to ln a uncertainties :
large absolute values, say >2.5, point to suspect info.
hat are the diagonal elements of the hat matrix :
large values, say >0.33, point to influential data.
For 95% confidence, fit (= sd(fit)) < 1.73
however a larger value may be OK - look at the diagnostics!

	avP	sd	avT	sd	cor	fit
lsq	11.4	1.7	611	43	0.885	1.66

	P	sd(P)	T	sd(T)	cor	fit	e*	hat
py	10.87	1.82	596	49	0.919	1.55	0.75	0.36
gr	11.18	1.94	611	43	0.791	1.64	0.21	0.51
alm	11.89	1.67	626	45	0.909	1.50	-0.71	0.16
phl	10.90	1.25	594	34	0.895	1.20	-1.33	0.12
ann	12.10	1.65	632	45	0.916	1.43	0.95	0.28
east	11.53	1.42	613	37	0.884	1.41	1.26	0.02
an	11.23	1.88	611	43	0.808	1.65	-0.18	0.39
ab	11.42	1.67	612	46	0.874	1.66	-0.06	0.09
q	11.40	1.66	611	43	0.885	1.66	0	0
H2O	11.40	1.66	611	43	0.885	1.66	0	0
mu	11.40	1.66	611	43	0.885	1.66	0	0
pa	11.40	1.66	611	43	0.885	1.66	0	0

T = 611¡C, sd = 43,
P = 11.4 kbars, sd = 1.7, cor = 0.885, sigfit = 1.66
==========

Run 3:
an independent set of reactions has been calculated
Activities and their uncertainties

	py	gr	alm	phl	ann	east	an
a	0.00412	0.0500	0.0870	0.0360	0.0340	0.0420	0.370
sd(a)/a	0.63457	0.35902	0.28736	0.39392	0.41133	0.37927	0.11907

	ab	q	H2O	mu	pa
a	0.780	1.00	1.00	1.00	1.00
sd(a)/a	0.05000	0	0	0	

Independent set of reactions
1) py + phl + 2mu = 3east + 6q
2) py + 2gr + 3east + 6q = 3phl + 6an
3) gr + alm + mu = ann + 3an
4) 2py + 3gr + 3mu + 4pa = 3east + 9an + 4ab + 4H2O

Calculations for the independent set of reactions
(for x(H2O) = 1.0)

	P(T)	sd(P)	a	sd(a)	b	c	ln_K	sd(ln_K)
1	8.0	2.57	-13.50	1.23	-0.01256	3.443	-0.694	1.361
2	12.6	1.22	-0.99	1.59	-0.21539	10.764	5.055	2.030
3	9.1	0.64	37.72	1.15	-0.12791	7.389	-0.927	0.713
4	8.9	0.56	267.31	2.37	-0.65716	26.613	0.519	2.292

Average PT (for x(H2O) = 1.0)

Single end-member diagnostic information

avP, avT, sd's, cor, fit are result of doubling the uncertainty on ln a :
a ln a suspect if any are v different from lsq values.
e* are ln a residuals normalised to ln a uncertainties :
large absolute values, say >2.5, point to suspect info.
hat are the diagonal elements of the hat matrix :
large values, say >0.33, point to influential data.
For 95% confidence, fit (= sd(fit)) < 1.73
however a larger value may be OK - look at the diagnostics!

avP	sd	avT	sd	cor	fit

```
   lsq   11.7   1.8    615    45 0.876  1.74

         P  sd(P)     T  sd(T)    cor    fit    e*   hat
    py  11.14   1.90    597     50  0.911   1.59   0.85  0.35
    gr  11.53   2.07    614     45  0.786   1.72   0.20  0.45
   alm  12.25   1.77    630     46  0.900   1.57  -0.73  0.14
   phl  11.22   1.34    597     35  0.885   1.25  -1.39  0.12
   ann  12.53   1.74    638     46  0.909   1.47   1.04  0.29
  east  11.89   1.55    616     39  0.874   1.51   1.24  0.03
    an  11.53   2.07    614     45  0.786   1.72  -0.20  0.45
    ab  11.76   1.79    616     48  0.865   1.74  -0.07  0.08
     q  11.74   1.77    615     45  0.876   1.74      0     0
   H2O  11.74   1.77    615     45  0.876   1.74      0     0
    mu  11.74   1.77    615     45  0.876   1.74      0     0
    pa  11.74   1.77    615     45  0.876   1.74      0     0


T = 615¡C, sd = 45,
P = 11.7 kbars, sd = 1.8, cor = 0.876, sigfit = 1.74
===============================================
```

Run 4:

```
an independent set of reactions has been calculated
Activities and their uncertainties
             py      gr     alm     phl     ann    east      an
a         0.00399  0.0500  0.0950  0.0380  0.0350  0.0450   0.410
sd(a)/a   0.63715  0.35902  0.30526  0.38888  0.40751  0.37244  0.10443

             ab       q     H2O      mu      pa
a          0.760    1.00    1.00    1.00    1.00
sd(a)/a    0.05000       0             0       0

Independent set of reactions
1)  py + phl + 2mu = 3east + 6q
2)  py + 2gr + 3east + 6q = 3phl + 6an
3)  gr + alm + mu = ann + 3an
4)  2py + 3gr + 3mu + 4pa = 3east + 9an + 4ab + 4H2O

Calculations for the independent set of reactions
(for x(H2O) = 1.0)
      P(T)   sd(P)      a   sd(a)        b       c     ln_K sd(ln_K)
1      7.7    2.53  -13.50    1.23  -0.01256    3.443   -0.509    1.344
2     12.2    1.19   -0.99    1.59  -0.21539   10.764    5.659    1.981
3      8.9    0.63   37.72    1.15  -0.12791    7.389   -0.678    0.697
4      8.7    0.54  267.31    2.37  -0.65716   26.613    1.610    2.226

Average PT (for x(H2O) = 1.0)

Single end-member diagnostic information

avP, avT, sd's, cor, fit are result of doubling the uncertainty on ln a :
a ln a suspect if any are v different from lsq values.
e* are ln a residuals normalised to ln a uncertainties :
large absolute values, say >2.5, point to suspect info.
hat are the diagonal elements of the hat matrix :
large values, say >0.33, point to influential data.
For 95% confidence, fit (= sd(fit)) < 1.73
however a larger value may be OK - look at the diagnostics!
```

	avP	sd	avT	sd	cor	fit
lsq	11.4	1.7	611	43	0.885	1.66

	P	sd(P)	T	sd(T)	cor	fit	e*	hat
py	10.87	1.82	596	49	0.919	1.55	0.75	0.36
gr	11.18	1.94	611	43	0.791	1.64	0.21	0.51
alm	11.89	1.67	626	45	0.909	1.50	-0.71	0.16
phl	10.90	1.25	594	34	0.895	1.20	-1.33	0.12
ann	12.10	1.65	632	45	0.916	1.43	0.95	0.28
east	11.53	1.42	613	37	0.884	1.41	1.26	0.02
an	11.23	1.88	611	43	0.808	1.65	-0.18	0.39
ab	11.42	1.67	612	46	0.874	1.66	-0.06	0.09
q	11.40	1.66	611	43	0.885	1.66	0	0
H2O	11.40	1.66	611	43	0.885	1.66	0	0
mu	11.40	1.66	611	43	0.885	1.66	0	0
pa	11.40	1.66	611	43	0.885	1.66	0	0

T = 611¡C, sd = 43,
P = 11.4 kbars, sd = 1.7, cor = 0.885, sigfit = 1.66
==========

Run 6:
an independent set of reactions has been calculated
Activities and their uncertainties

	py	gr	alm	phl	ann	east	an
a	0.00449	0.0510	0.0910	0.0390	0.0370	0.0370	0.370
sd(a)/a	0.62754	0.35625	0.27245	0.38642	0.40013	0.39138	0.11907

	ab	q	H2O	mu	pa
a	0.780	1.00	1.00	1.00	1.00
sd(a)/a	0.05000	0	0	0	0

Independent set of reactions
1) py + phl + 2mu = 3east + 6q
2) py + 2gr + 3east + 6q = 3phl + 6an
3) gr + alm + mu = ann + 3an
4) 2py + 3gr + 3mu + 4pa = 3east + 9an + 4ab + 4H2O

Calculations for the independent set of reactions
(for x(H2O) = 1.0)

	P(T)	sd(P)	a	sd(a)	b	c	ln_K	sd(ln_K)
1	9.1	2.61	-13.50	1.23	-0.01256	3.443	-1.240	1.386
2	12.3	1.22	-0.99	1.59	-0.21539	10.764	5.550	2.033
3	9.1	0.63	37.72	1.15	-0.12791	7.389	-0.907	0.699
4	9.1	0.56	267.31	2.37	-0.65716	26.613	-0.093	2.299

Average PT (for x(H2O) = 1.0)

Single end-member diagnostic information

avP, avT, sd's, cor, fit are result of doubling the uncertainty on ln a :
a ln a suspect if any are v different from lsq values.
e* are ln a residuals normalised to ln a uncertainties :
large absolute values, say >2.5, point to suspect info.
hat are the diagonal elements of the hat matrix :
large values, say >0.33, point to influential data.
For 95% confidence, fit (= sd(fit)) < 1.73
however a larger value may be OK - look at the diagnostics!

	avP	sd	avT	sd	cor	fit
lsq	11.8	1.6	613	42	0.872	1.65

	P	sd(P)	T	sd(T)	cor	fit	e*	hat
py	11.05	1.65	593	43	0.907	1.42	1.04	0.34
gr	11.60	1.94	613	42	0.781	1.64	0.14	0.45
alm	12.27	1.61	628	42	0.896	1.45	-0.76	0.14
phl	11.30	1.30	598	34	0.882	1.24	-1.23	0.12
ann	12.59	1.54	638	41	0.907	1.32	1.11	0.30
east	11.86	1.54	614	39	0.871	1.52	0.90	0.02
an	11.60	1.94	613	42	0.781	1.64	-0.14	0.45
ab	11.78	1.66	615	44	0.861	1.64	-0.08	0.08
q	11.76	1.65	613	42	0.872	1.65	0	0
H2O	11.76	1.65	613	42	0.872	1.65	0	0
mu	11.76	1.65	613	42	0.872	1.65	0	0
pa	11.76	1.65	613	42	0.872	1.65	0	0

T = 613¡C, sd = 42,
P = 11.8 kbars, sd = 1.6, cor = 0.872, sigfit = 1.65

==========

Whole rock diagnostics:

Run 1:

an independent set of reactions has been calculated
Activities and their uncertainties

	py	gr	alm	phl	ann	east	an
a	0.00412	0.0500	0.0870	0.0360	0.0340	0.0420	0.390
sd(a)/a	0.63457	0.35902	0.28736	0.39392	0.41133	0.37927	0.11163

	ab	q	H2O	mu	pa
a	0.770	1.00	1.00	1.00	1.00
sd(a)/a	0.05000	0	0	0	

Independent set of reactions

1) py + phl + 2mu = 3east + 6q
2) py + 2gr + 3east + 6q = 3phl + 6an
3) gr + alm + mu = ann + 3an
4) 2py + 3gr + 3mu + 4pa = 3east + 9an + 4ab + 4H2O

Calculations for the independent set of reactions
(for x(H2O) = 1.0)

	P(T)	sd(P)	a	sd(a)	b	c	ln_K	sd(ln_K)
1	8.0	2.57	-13.50	1.23	-0.01256	3.443	-0.694	1.361
2	12.4	1.21	-0.99	1.59	-0.21539	10.764	5.371	2.014
3	9.0	0.63	37.72	1.15	-0.12791	7.389	-0.769	0.702
4	8.8	0.55	267.31	2.37	-0.65716	26.613	0.941	2.262

Average PT (for x(H2O) = 1.0)

Single end-member diagnostic information

avP, avT, sd's, cor, fit are result of doubling the uncertainty on ln a :
a ln a suspect if any are v different from lsq values.
e* are ln a residuals normalised to ln a uncertainties :
large absolute values, say >2.5, point to suspect info.
hat are the diagonal elements of the hat matrix :
large values, say >0.33, point to influential data.

For 95% confidence, fit (= sd(fit)) < 1.73
however a larger value may be OK - look at the diagnostics!

	avP	sd	avT	sd	cor	fit
lsq	11.6	1.7	613	44	0.880	1.72

	P	sd(P)	T	sd(T)	cor	fit	e*	hat
py	10.95	1.84	595	49	0.914	1.57	0.87	0.35
gr	11.36	2.02	612	44	0.787	1.70	0.19	0.48
alm	12.07	1.72	628	46	0.903	1.55	-0.73	0.14
phl	11.05	1.31	595	35	0.890	1.25	-1.37	0.12
ann	12.35	1.69	636	45	0.913	1.44	1.05	0.29
east	11.70	1.52	614	39	0.879	1.51	1.19	0.02
an	11.39	1.99	612	44	0.796	1.70	-0.18	0.42
ab	11.58	1.74	614	47	0.869	1.72	-0.07	0.08
q	11.57	1.73	613	44	0.880	1.72	0	0
H2O	11.57	1.73	613	44	0.880	1.72	0	0
mu	11.57	1.73	613	44	0.880	1.72	0	0
pa	11.57	1.73	613	44	0.880	1.72	0	0

T = 613¡C, sd = 44,
P = 11.6 kbars, sd = 1.7, cor = 0.880, sigfit = 1.72
==========

Run 2:
an independent set of reactions has been calculated
Activities and their uncertainties

	py	gr	alm	phl	ann	east	an
a	0.00399	0.0500	0.0950	0.0380	0.0350	0.0450	0.430
sd(a)/a	0.63715	0.35902	0.30526	0.38888	0.40751	0.37244	0.09747

	ab	q	H2O	mu	pa
a	0.750	1.00	1.00	1.00	1.00
sd(a)/a	0.05000	0	0	0	

Independent set of reactions
1) py + phl + 2mu = 3east + 6q
2) py + 2gr + 3east + 6q = 3phl + 6an
3) gr + alm + mu = ann + 3an
4) 2py + 3gr + 3mu + 4pa = 3east + 9an + 4ab + 4H2O

Calculations for the independent set of reactions
(for x(H2O) = 1.0)

	P(T)	sd(P)	a	sd(a)	b	c	ln_K	sd(ln_K)
1	7.7	2.53	-13.50	1.23	-0.01256	3.443	-0.509	1.344
2	12.0	1.18	-0.99	1.59	-0.21539	10.764	5.944	1.968
3	8.7	0.62	37.72	1.15	-0.12791	7.389	-0.535	0.688
4	8.6	0.54	267.31	2.37	-0.65716	26.613	1.985	2.200

Average PT (for x(H2O) = 1.0)

Single end-member diagnostic information

avP, avT, sd's, cor, fit are result of doubling the uncertainty on ln a :
a ln a suspect if any are v different from lsq values.
e* are ln a residuals normalised to ln a uncertainties :
large absolute values, say >2.5, point to suspect info.
hat are the diagonal elements of the hat matrix :

large values, say >0.33, point to influential data.
For 95% confidence, fit (= sd(fit)) < 1.73
however a larger value may be OK - look at the diagnostics!

	avP	sd	avT	sd	cor	fit
lsq	11.2	1.6	610	43	0.889	1.64

	P	sd(P)	T	sd(T)	cor	fit	e*	hat
py	10.70	1.76	594	48	0.921	1.52	0.76	0.36
gr	11.03	1.90	609	42	0.793	1.63	0.20	0.54
alm	11.73	1.62	624	44	0.912	1.48	-0.71	0.16
phl	10.74	1.22	592	33	0.899	1.19	-1.31	0.12
ann	11.93	1.61	630	44	0.919	1.41	0.95	0.28
east	11.36	1.39	611	37	0.888	1.41	1.22	0.02
an	11.10	1.82	609	42	0.818	1.63	-0.16	0.36
ab	11.25	1.63	610	45	0.877	1.64	-0.06	0.09
q	11.24	1.62	610	43	0.889	1.64	0	0
H2O	11.24	1.62	610	43	0.889	1.64	0	0
mu	11.24	1.62	610	43	0.889	1.64	0	0
pa	11.24	1.62	610	43	0.889	1.64	0	0

T = 610¡C, sd = 43,
P = 11.2 kbars, sd = 1.6, cor = 0.889, sigfit = 1.64
==========

Run 4:
an independent set of reactions has been calculated
Activities and their uncertainties

	py	gr	alm	phl	ann	east	an
a	0.00449	0.0510	0.0910	0.0390	0.0370	0.0370	0.410
sd(a)/a	0.62754	0.35625	0.27245	0.38642	0.40013	0.39138	0.10443

	ab	q	H2O	mu	pa
a	0.760	1.00	1.00	1.00	1.00
sd(a)/a	0.05000	0	0	0	

Independent set of reactions
1) py + phl + 2mu = 3east + 6q
2) py + 2gr + 3east + 6q = 3phl + 6an
3) gr + alm + mu = ann + 3an
4) 2py + 3gr + 3mu + 4pa = 3east + 9an + 4ab + 4H2O

Calculations for the independent set of reactions
(for x(H2O) = 1.0)

	P(T)	sd(P)	a	sd(a)	b	c	ln_K	sd(ln_K)
1	9.1	2.61	-13.50	1.23	-0.01256	3.443	-1.240	1.386
2	11.9	1.21	-0.99	1.59	-0.21539	10.764	6.166	2.004
3	8.8	0.61	37.72	1.15	-0.12791	7.389	-0.599	0.678
4	8.9	0.55	267.31	2.37	-0.65716	26.613	0.727	2.240

Average PT (for x(H2O) = 1.0)

Single end-member diagnostic information

avP, avT, sd's, cor, fit are result of doubling the uncertainty on ln a :
a ln a suspect if any are v different from lsq values.
e* are ln a residuals normalised to ln a uncertainties :
large absolute values, say >2.5, point to suspect info.

hat are the diagonal elements of the hat matrix :
large values, say >0.33, point to influential data.
For 95% confidence, fit (= sd(fit)) < 1.73
however a larger value may be OK - look at the diagnostics!

	avP	sd	avT	sd	cor	fit
lsq	11.4	1.6	609	41	0.880	1.62

	P	sd(P)	T	sd(T)	cor	fit	e*	hat
py	10.69	1.55	589	42	0.913	1.37	1.07	0.34
gr	11.26	1.87	609	41	0.785	1.61	0.13	0.51
alm	11.92	1.53	625	41	0.904	1.42	-0.77	0.14
phl	10.96	1.27	594	34	0.891	1.24	-1.19	0.12
ann	12.23	1.45	634	39	0.914	1.28	1.13	0.30
east	11.48	1.49	610	38	0.879	1.52	0.81	0.02
an	11.29	1.81	609	41	0.801	1.62	-0.11	0.39
ab	11.42	1.59	611	43	0.869	1.62	-0.08	0.09
q	11.40	1.58	609	41	0.880	1.62	0	0
H2O	11.40	1.58	609	41	0.880	1.62	0	0
mu	11.40	1.58	609	41	0.880	1.62	0	0
pa	11.40	1.58	609	41	0.880	1.62	0	0

T = 609¡C, sd = 41,
P = 11.4 kbars, sd = 1.6, cor = 0.880, sigfit = 1.62
==========

Run 9:
an independent set of reactions has been calculated
Activities and their uncertainties

	py	gr	alm	phl	ann	east	an
a	0.00301	0.0550	0.100	0.0390	0.0370	0.0370	0.390
sd(a)/a	0.65887	0.34563	0.26000	0.38642	0.40013	0.39138	0.11163

	ab	q	H2O	mu	pa
a	0.770	1.00	1.00	1.00	1.00
sd(a)/a	0.05000	0	0	0	

Independent set of reactions
1) py + phl + 2mu = 3east + 6q
2) py + 2gr + 3east + 6q = 3phl + 6an
3) gr + alm + mu = ann + 3an
4) 2py + 3gr + 3mu + 4pa = 3east + 9an + 4ab + 4H2O

Calculations for the independent set of reactions
(for x(H2O) = 1.0)

	P(T)	sd(P)	a	sd(a)	b	c	ln_K	sd(ln_K)
1	8.3	2.64	-13.50	1.23	-0.01256	3.443	-0.841	1.401
2	11.9	1.22	-0.99	1.59	-0.21539	10.764	6.115	2.021
3	9.1	0.61	37.72	1.15	-0.12791	7.389	-0.919	0.678
4	8.8	0.56	267.31	2.37	-0.65716	26.613	0.902	2.289

Average PT (for x(H2O) = 1.0)

Single end-member diagnostic information

avP, avT, sd's, cor, fit are result of doubling the uncertainty on ln a :
a ln a suspect if any are v different from lsq values.
e* are ln a residuals normalised to ln a uncertainties :

large absolute values, say >2.5, point to suspect info.
hat are the diagonal elements of the hat matrix :
large values, say >0.33, point to influential data.
For 95% confidence, fit (= sd(fit)) < 1.73
however a larger value may be OK - look at the diagnostics!

	avP	sd	avT	sd	cor	fit
lsq	11.4	1.3	604	35	0.880	1.38

	P	sd(P)	T	sd(T)	cor	fit	e*	hat
py	10.94	1.42	591	38	0.911	1.26	0.71	0.33
gr	11.23	1.58	604	34	0.790	1.37	0.15	0.46
alm	11.76	1.37	615	36	0.904	1.26	-0.53	0.14
phl	11.01	1.02	591	27	0.889	1.00	-1.09	0.11
ann	12.03	1.36	623	36	0.916	1.17	0.81	0.32
east	11.49	1.17	605	30	0.879	1.19	1.02	0.02
an	11.24	1.56	604	34	0.794	1.37	-0.15	0.44
ab	11.41	1.36	605	37	0.869	1.38	-0.05	0.09
q	11.39	1.35	604	35	0.880	1.38	0	0
H2O	11.39	1.35	604	35	0.880	1.38	0	0
mu	11.39	1.35	604	35	0.880	1.38	0	0
pa	11.39	1.35	604	35	0.880	1.38	0	0

T = 604¡C, sd = 35,
P = 11.4 kbars, sd = 1.3, cor = 0.880, sigfit = 1.38
==========

Run 11

an independent set of reactions has been calculated
Activities and their uncertainties

	py	gr	alm	phl	ann	east	an
a	0.00412	0.0500	0.0870	0.0360	0.0340	0.0420	0.390
sd(a)/a	0.63457	0.35902	0.28736	0.39392	0.41133	0.37927	0.11163

	ab	an	ab	q	H2O	mu	pa
a	0.770	0.370	0.780	1.00	1.00	1.00	1.00
sd(a)/a	0.05000	0.11907	0.05000	0	0	0	0

Independent set of reactions
1) py + phl + 2mu = 3east + 6q
2) py + 2gr + 3east + 6q = 3phl + 6an
3) py + 2gr + 3east + 6q = 3phl + 6an
4) gr + alm + mu = ann + 3an
5) 2py + 3gr + 3mu + 4pa = 3east + 9an + 4ab + 4H2O
6) 2py + 3gr + 3mu + 4pa = 3east + 9an + 4ab + 4H2O

Calculations for the independent set of reactions
(for x(H2O) = 1.0)

	P(T)	sd(P)	a	sd(a)	b	c	ln_K	sd(ln_K)
1	8.0	2.57	-13.50	1.23	-0.01256	3.443	-0.694	1.361
2	12.4	1.21	-0.99	1.59	-0.21539	10.764	5.371	2.014
3	12.6	1.22	-0.99	1.59	-0.21539	10.764	5.055	2.030
4	9.0	0.63	37.72	1.15	-0.12791	7.389	-0.769	0.702
5	8.8	0.55	267.31	2.37	-0.65716	26.613	0.941	2.262
6	8.8	0.55	267.31	2.37	-0.65716	26.613	0.992	2.262

Average PT (for x(H2O) = 1.0)

Single end-member diagnostic information

avP, avT, sd's, cor, fit are result of doubling the uncertainty on ln a :
a ln a suspect if any are v different from lsq values.
e* are ln a residuals normalised to ln a uncertainties :
large absolute values, say >2.5, point to suspect info.
hat are the diagonal elements of the hat matrix :
large values, say >0.43, point to influential data.
For 95% confidence, fit (= sd(fit)) < 1.54
however a larger value may be OK - look at the diagnostics!

	avP	sd	avT	sd	cor	fit
lsq	11.7	1.2	614	32	0.901	1.24

	P	sd(P)	T	sd(T)	cor	fit	e*	hat
py	11.08	1.31	596	35	0.930	1.13	0.86	0.35
gr	11.47	1.43	613	32	0.799	1.23	0.20	0.62
alm	12.19	1.22	629	33	0.922	1.12	-0.73	0.15
phl	11.14	1.03	596	28	0.911	0.90	-1.38	0.12
ann	12.47	1.20	637	33	0.929	1.05	1.05	0.30
east	11.80	1.06	615	28	0.901	1.08	1.22	0.02
an	11.71	1.24	614	32	0.887	1.23	0.12	0.15
ab	11.69	1.21	614	32	0.900	1.23	-0.16	0.02
an	11.62	1.22	613	31	0.890	1.22	-0.33	0.13
ab	11.68	1.21	613	32	0.900	1.24	0.10	0.02
q	11.68	1.21	614	32	0.901	1.24	0	0
H2O	11.68	1.21	614	32	0.901	1.24	0	0
mu	11.68	1.21	614	32	0.901	1.24	0	0
pa	11.68	1.21	614	32	0.901	1.24	0	0

T = 614¡C, sd = 32,
P = 11.7 kbars, sd = 1.2, cor = 0.901, sigfit = 1.24
==========

Run 13
an independent set of reactions has been calculated
Activities and their uncertainties

	py	gr	alm	phl	ann	east	an
a	0.00301	0.0550	0.100	0.0360	0.0340	0.0420	0.390
sd(a)/a	0.65887	0.34563	0.26000	0.39392	0.41133	0.37927	0.11163

	ab	an	ab	q	H2O	mu	pa
a	0.770	0.370	0.780	1.00	1.00	1.00	1.00
sd(a)/a	0.05000	0.11907	0.05000	0	0	0	

Independent set of reactions
1) py + phl + 2mu = 3east + 6q
2) py + 2gr + 3east + 6q = 3phl + 6an
3) py + 2gr + 3east + 6q = 3phl + 6an
4) gr + alm + mu = ann + 3an
5) 2py + 3gr + 3mu + 4pa = 3east + 9an + 4ab + 4H2O
6) 2py + 3gr + 3mu + 4pa = 3east + 9an + 4ab + 4H2O

Calculations for the independent set of reactions
(for x(H2O) = 1.0)

	P(T)	sd(P)	a	sd(a)	b	c	ln_K	sd(ln_K)
1	7.5	2.60	-13.54	1.23	-0.01230	3.421	-0.380	1.373
2	12.3	1.21	-0.39	1.59	-0.21598	10.746	5.495	2.013

3 12.5 1.22 -0.39 1.59 -0.21598 10.746 5.179 2.028
4 9.2 0.62 37.97 1.15 -0.12804 7.368 -1.003 0.684
5 8.7 0.56 267.13 2.37 -0.65443 26.355 1.283 2.271
6 8.7 0.56 267.13 2.37 -0.65443 26.355 1.334 2.271

Average PT (for x(H2O) = 1.0)

Single end-member diagnostic information

avP, avT, sd's, cor, fit are result of doubling the uncertainty on ln a :
a ln a suspect if any are v different from lsq values.
e* are ln a residuals normalised to ln a uncertainties :
large absolute values, say >2.5, point to suspect info.
hat are the diagonal elements of the hat matrix :
large values, say >0.43, point to influential data.
For 95% confidence, fit (= sd(fit)) < 1.54
however a larger value may be OK - look at the diagnostics!

	avP	sd	avT	sd	cor	fit
lsq	11.6	1.1	610	28	0.905	1.11

	P	sd(P)	T	sd(T)	cor	fit	e*	hat
py	11.28	1.21	599	32	0.931	1.07	0.55	0.34
gr	11.42	1.26	609	28	0.806	1.10	0.21	0.60
alm	11.98	1.13	620	30	0.924	1.05	-0.49	0.14
phl	11.16	1.01	594	27	0.913	0.80	-1.28	0.11
ann	12.25	1.15	628	31	0.934	1.00	0.78	0.34
east	11.75	0.97	611	25	0.904	0.89	1.37	0.02
an	11.66	1.10	610	28	0.890	1.11	0.11	0.16
ab	11.64	1.08	610	28	0.903	1.11	-0.15	0.03
an	11.57	1.08	609	28	0.893	1.10	-0.34	0.14
ab	11.63	1.08	609	28	0.903	1.11	0.11	0.03
q	11.64	1.08	610	28	0.905	1.11	0	0
H2O	11.64	1.08	610	28	0.905	1.11	0	0
mu	11.64	1.08	610	28	0.905	1.11	0	0
pa	11.64	1.08	610	28	0.905	1.11	0	0

T = 610¡C, sd = 28,
P = 11.6 kbars, sd = 1.1, cor = 0.905, sigfit = 1.11
==========

Run 14
an independent set of reactions has been calculated
Activities and their uncertainties

	py	gr	alm	phl	ann	east	an
a	0.00301	0.0550	0.100	0.0360	0.0340	0.0420	0.430
sd(a)/a	0.65887	0.34563	0.26000	0.39392	0.41133	0.37927	0.09747

	ab	an	ab	q	H2O	mu	pa
a	0.750	0.410	0.760	1.00	1.00	1.00	1.00
sd(a)/a	0.05000	0.10443	0.05000	0	0	0	

Independent set of reactions
1) py + phl + 2mu = 3east + 6q
2) py + 2gr + 3east + 6q = 3phl + 6an
3) py + 2gr + 3east + 6q = 3phl + 6an
4) gr + alm + mu = ann + 3an

5) 2py + 3gr + 3mu + 4pa = 3east + 9an + 4ab + 4H2O
6) 2py + 3gr + 3mu + 4pa = 3east + 9an + 4ab + 4H2O

Calculations for the independent set of reactions
(for x(H2O) = 1.0)

	P(T)	sd(P)	a	sd(a)	b	c	ln_K	sd(ln_K)
1	7.5	2.60	-13.54	1.23	-0.01230	3.421	-0.380	1.373
2	12.0	1.20	-0.39	1.59	-0.21598	10.746	6.080	1.986
3	12.1	1.20	-0.39	1.59	-0.21598	10.746	5.795	1.999
4	8.9	0.60	37.97	1.15	-0.12804	7.368	-0.710	0.665
5	8.6	0.55	267.13	2.37	-0.65443	26.355	2.056	2.217
6	8.5	0.55	267.13	2.37	-0.65443	26.355	2.109	2.217

Average PT (for x(H2O) = 1.0)

Single end-member diagnostic information

avP, avT, sd's, cor, fit are result of doubling the uncertainty on ln a :
a ln a suspect if any are v different from lsq values.
e* are ln a residuals normalised to ln a uncertainties :
large absolute values, say >2.5, point to suspect info.
hat are the diagonal elements of the hat matrix :
large values, say >0.43, point to influential data.
For 95% confidence, fit (= sd(fit)) < 1.54
however a larger value may be OK - look at the diagnostics!

	avP	sd	avT	sd	cor	fit
lsq	11.3	1.0	606	27	0.909	1.08

	P	sd(P)	T	sd(T)	cor	fit	e*	hat
py	10.91	1.14	595	31	0.934	1.03	0.59	0.34
gr	11.08	1.20	605	27	0.807	1.07	0.20	0.65
alm	11.63	1.07	616	29	0.927	1.01	-0.50	0.13
phl	10.83	0.99	591	27	0.917	0.78	-1.23	0.11
ann	11.90	1.13	624	31	0.937	0.96	0.79	0.34
east	11.38	0.95	607	25	0.908	0.88	1.27	0.02
an	11.31	1.04	606	27	0.897	1.08	0.14	0.13
ab	11.29	1.02	606	27	0.907	1.08	-0.16	0.03
an	11.23	1.02	606	27	0.899	1.07	-0.33	0.12
ab	11.28	1.02	605	27	0.907	1.08	0.11	0.03
q	11.28	1.02	606	27	0.909	1.08	0	0
H2O	11.28	1.02	606	27	0.909	1.08	0	0
mu	11.28	1.02	606	27	0.909	1.08	0	0
pa	11.28	1.02	606	27	0.909	1.08	0	0

T = 606¡C, sd = 27,
P = 11.3 kbars, sd = 1.0, cor = 0.909, sigfit = 1.08
==========

Run 15
an independent set of reactions has been calculated
Activities and their uncertainties

	py	gr	alm	phl	ann	east	an
a	0.00301	0.0550	0.100	0.0380	0.0350	0.0450	0.390
sd(a)/a	0.65887	0.34563	0.26000	0.38888	0.40751	0.37244	0.11163

	ab	an	ab	q	H2O	mu	pa
a	0.770	0.410	0.760	1.00	1.00	1.00	1.00

sd(a)/a 0.05000 0.10443 0.05000 0 0 0

Independent set of reactions
1) py + phl + 2mu = 3east + 6q
2) py + 2gr + 3east + 6q = 3phl + 6an
3) py + 2gr + 3east + 6q = 3phl + 6an
4) gr + alm + mu = ann + 3an
5) 2py + 3gr + 3mu + 4pa = 3east + 9an + 4ab + 4H2O
6) 2py + 3gr + 3mu + 4pa = 3east + 9an + 4ab + 4H2O

Calculations for the independent set of reactions
(for x(H2O) = 1.0)

	P(T)	sd(P)	a	sd(a)	b	c	ln_K	sd(ln_K)
1	7.2	2.57	-13.54	1.23	-0.01230	3.421	-0.227	1.354
2	12.3	1.20	-0.39	1.59	-0.21598	10.746	5.450	1.992
3	12.1	1.19	-0.39	1.59	-0.21598	10.746	5.750	1.978
4	9.1	0.62	37.97	1.15	-0.12804	7.368	-0.974	0.682
5	8.7	0.56	267.13	2.37	-0.65443	26.355	1.490	2.260
6	8.7	0.56	267.13	2.37	-0.65443	26.355	1.437	2.260

Average PT (for x(H2O) = 1.0)

Single end-member diagnostic information

avP, avT, sd's, cor, fit are result of doubling the uncertainty on ln a :
a ln a suspect if any are v different from lsq values.
e* are ln a residuals normalised to ln a uncertainties :
large absolute values, say >2.5, point to suspect info.
hat are the diagonal elements of the hat matrix :
large values, say >0.43, point to influential data.
For 95% confidence, fit (= sd(fit)) < 1.54
however a larger value may be OK - look at the diagnostics!

	avP	sd	avT	sd	cor	fit
lsq	11.4	1.1	605	29	0.906	1.14

	P	sd(P)	T	sd(T)	cor	fit	e*	hat
py	11.02	1.21	596	33	0.932	1.10	0.54	0.34
gr	11.14	1.27	605	28	0.806	1.12	0.22	0.63
alm	11.71	1.14	616	31	0.925	1.08	-0.50	0.14
phl	10.90	0.99	590	27	0.914	0.81	-1.31	0.11
ann	11.97	1.16	623	32	0.935	1.03	0.78	0.34
east	11.48	0.95	607	25	0.905	0.90	1.42	0.02
an	11.30	1.08	605	28	0.895	1.12	-0.34	0.13
ab	11.36	1.08	605	29	0.904	1.14	0.11	0.03
an	11.39	1.10	606	29	0.893	1.14	0.12	0.15
ab	11.38	1.08	606	29	0.904	1.14	-0.15	0.03
q	11.37	1.08	605	29	0.906	1.14	0	0
H2O	11.37	1.08	605	29	0.906	1.14	0	0
mu	11.37	1.08	605	29	0.906	1.14	0	0
pa	11.37	1.08	605	29	0.906	1.14	0	0

T = 605¡C, sd = 29,
P = 11.4 kbars, sd = 1.1, cor = 0.906, sigfit = 1.14
==========

8.4 Appendix D, Thin-section 25 (Kebne Dyke Complex) SEM/EDS analyse.

Some additional geochemical results beyond the scope of this study were retrieved from the Kebne Dyke Complex unit with the electron microscope. These results point to alteration processes of the Kebne Dyke Complex involving (igneous) Pyroxene to Pyroxene alteration along with (metamorphic) Pyroxene to Amphibole alteration. The Pyroxene- Pyroxene alteration is manifested as Bronzite crystals with surrounding corona structures of inverted Pigeonite. Pyroxene to Amphibole alteration is displayed by Orthopyroxene and minor amounts of Clinopyroxene surrounded by alteration rims of Hornblende.

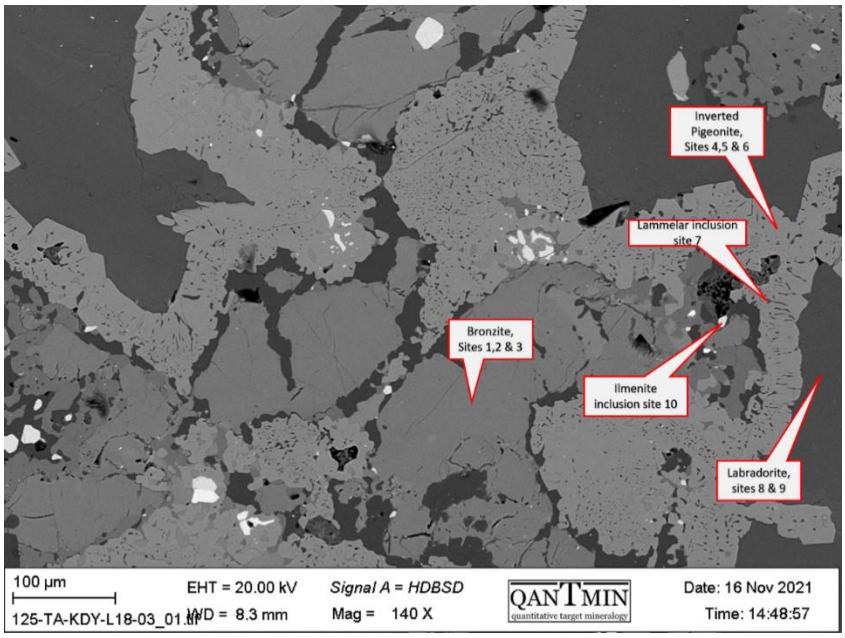

Figure 74. Corona structure seen in back scattered view of thin section 25 displaying Bronzite with a corona of inverted Pigeonite and Labradorite crystals. Ilmenite are found as white spots.

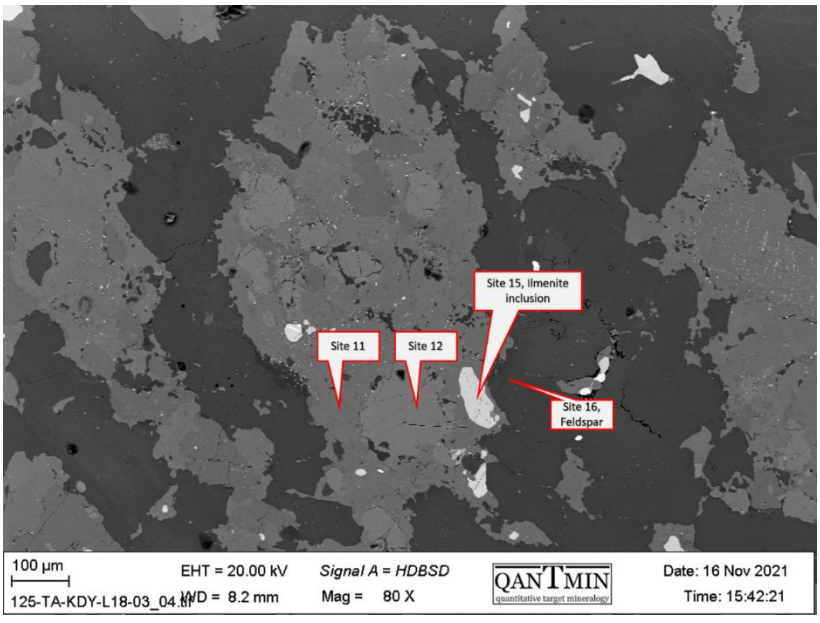

Figure 75. Backscattered view of thin section 25. Suspected Uratilization process involving site 13 & 14.

Table A19. Additional geochemical analyse result, thin section 25

Site	Na2O3	MgO	TiO2	Al2O3	MnO	SiO2	K2O	CaO	FeO	Sum
Bronzite										
1		21.765539193		1.2932499374		49.8930304975		2.380111782	24.6680685901	72.9518196279
2		22.682293165		1.3622300955		50.2558101923			25.6996665471	74.3003334529
3		22.4738216582		1.4643297203		50.0369730406			26.0248755809	73.9751244191
Inverted Pigeonite										
4		4.8864406269		22.7004441473		35.3488120338		11.1514210647	25.9128821273	62.9356968079
5		4.8682527697		22.5664616853		35.0679847986		10.7247146306	26.7725861159	62.5026992535
6		4.8724687754		22.8113182194	0.6968528504	35.1713993368		10.8233450887	25.6246157293	63.552039182
7*		2.3408574203		11.1164699591		69.0782743176		5.2347620482	12.2296362548	82.5356016977
Ilmenite										
10		1.0114495399	47.6798909599			14.4420020345			36.8666574657	48.6913404998
15			51.9568339766			1.5401177253			46.5030482981	51.9568339766
Feldspar										
8	6.2878077069			29.8104852459		52.8922622607		11.0094447865		29.8104852459
9	5.8960434206			30.0512236337		53.2970849749		10.7556479708		30.0512236337
16	4.3152861829			34.0433558346		48.1336065264		13.507751456		34.0433558346
Uratlitization process										
11		17.8796707685		1.3734171802		47.1912756584		1.2289276853	32.3267087076	67.6732912924
12	1.1787422967	13.0019671623		7.5187026757		44.9402915329	1.0888843518	1.5809670715	30.6904449091	68.1308127942

*Table A19. Additional geochemical analyse table of selected sites from thin section 25. *Lamellar inclusion in Inverted Pigeonite.*